A Physical-Space Version of the Stretched-Vortex Subgrid-Stress Model for Large-Eddy Simulation of Incompressible Flow

Thesis by

Tobias Voelkl

In Partial Fulfillment of the Requirements

for the Degree of

Doctor of Philosophy

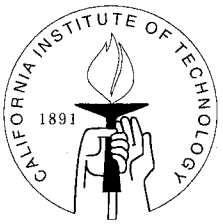

California Institute of Technology

Pasadena, California

2000

(Submitted April 21, 2000)

Acknowledgements

First and foremost I would like to express my deep gratitude to my adviser, Prof. Dale I. Pullin, for making this thesis possible. His patience and generosity in supporting his students at all times were a continual source of motivation during the work on this project.

I also gratefully acknowledge the help from Ashish Misra, my predecessor in the work on the stretched-vortex model, and from Ron Henderson, who answered my many questions about numerical methods. My fellow students and friends here at the Graduate Aeronautical Laboratories (GALCIT), among them Mark Brady, Luis González Liñero, Giorgio Isella, Stefan Schlamp, and Claude Seywert, helped me in many ways, and I thank all of them. Thanks are also due to the many other members of GALCIT, who taught me, were available for discussions, and were supportive of my work.

My family always supported me in my endeavors, which is particularly important to me, and I am most grateful for that.

I would also like to acknowledge the material support, without which this work would not have been possible either, in particular, financial support for this project by the National Science Foundation under Grant CTS-9634222. The computational resources, which have most generously been provided by the ASCI center at Caltech under the Academic Strategic Alliances Program of the Accelerated Strategic Computing Initiative (ASCI/ASAP) under subcontract no. B341492 of DOE contract W-7405-ENG-48, were of vital importance for this project and are gratefully acknowledged, too. My thanks also go to the institutions where the computations under the ASCI program were carried out, namely Pittsburgh Supercomputing Center (PSC), Los Alamos National Laboratory (LANL), and the Caltech Center for Advanced Computing Research (CACR).

Abstract

In large-eddy simulations of turbulence, the large scales of the flow are resolved by a numerical solution of the equations of motion for these scales, but the contribution of the fine-scale turbulence must be modeled. The stretched-vortex model estimates the influence of these unresolved subgrid-scale turbulence fluctuations on the resolved-scale velocities by using kinematic results for homogeneous, anisotropic turbulence consisting of locally straight, unidirectional vortex structures [D. I. Pullin and P. G. Saffman, Phys. Fluids **6** (5), 1994]. A new method is presented to dynamically determine the value of model constants related to the subgrid kinetic energy. For this purpose, a relation between the resolved-scale velocity structure function of second order and the energy spectrum is derived based on the kinematics of the model vortex structures, and therefore without the assumption of isotropy. Implementation of this relation using a local, circular average allows application of the model to wall-bounded turbulent flows without special modifications. The resulting algebraic model is completely localized, i.e., no global flow quantities like the resolved-scale spectrum are required. This facilitates the application of the model in physical-space numerical methods using, for example, finite differences or Lagrangian-interpolation polynomials. The model includes an estimate of the subgrid kinetic energy, which is used to compute subgrid contributions to low-order turbulence statistics of the full flowfield. Results will be shown for the decay of kinetic energy and energy spectra of decaying, isotropic turbulence, for mean velocities, root-mean-square velocity fluctuations and turbulence-kinetic-energy budgets of channel flow up to a Reynolds number of approximately 23 000 (based on channel halfwidth and centerline velocity), and for mean velocities and turbulence kinetic energy of channel flow under spanwise rotation. The results are compared to unfiltered data from direct numerical simulations and experiment.

Contents

Nomenclature

Roman letters

$\mathrm{a}(\,.\,,\,.\,)$	Weak form of Helmholtz operator
$c = c_R + ic_I$	(Complex) wavespeed in Orr-Sommerfeld equation, Sec. 3.3.5
$\mathbf{D}$	Derivative matrix, defined for GLL discretization in (3.32)
$\mathbf{D} \cdot (\,.\,)$	Discrete divergence operator
E_{ij}	Rotation matrix
$\tilde{\mathbf{e}}_1$, $\tilde{\mathbf{e}}_2$, $\tilde{\mathbf{e}}_3$	Eigenvectors of resolved rate-of-strain tensor $\tilde{S}_{ij}$
$E'(t)$	Perturbation energy of small disturbances in channel flow, see Sec. 3.3.5
$E(k)$	Three-dimensional, shell-summed energy spectrum
$\mathbf{e}_v$, e_i^v	Unit vector describing orientation of subgrid-vortex axis
F_2	Second-order structure function of the velocity vector
$\tilde{F}_2$	Structure function of the resolved-scale velocity vector
$\tilde{F}_2^{\odot}$	Circular average of resolved-scale structure function
$g_{\mathcal{N}}$	Neumann boundary condition
$\mathbf{G}$	Discrete gradient operator
h	Channel halfwidth
h_i	Lagrange polynomial through GLL points ξ_k, basis function for polynomial expansion

$(\hat{\boldsymbol{\imath}}_1, \hat{\boldsymbol{\imath}}_2, \hat{\boldsymbol{\imath}}_3)$	Unit vectors spanning a cartesian coordinate system
I_1,I_2,I_3	Tensor invariants of $\tilde{S}_{ij}$, see Sec. 3.3.6
J	Cutoff parameter in model energy spectrum
J_e, J_i	Order of the explicit (J_e) and implicit (J_i) time integration for time discretization of Sec. 3.3.4
J_0	Zeroth order Bessel function of the first kind
K	Subgrid kinetic energy
k	Wavenumber
$\mathcal{K}_0$	Kolmogorov prefactor
k_c	Cutoff wavenumber
ℓ	Integral or outer scale of turbulence
$\mathbf{L}$	Linear diffusion operator
L_i	Legendre polynomial of order i
$\hat{\mathbf{n}}$	Unit normal vector of the plane in which circular averaging is performed
N_α	Number of modes in coordinate direction α, resolution
$\mathbf{N}$	Nonlinear advection operator in the Navier-Stokes equations
P	Pressure
$P(\alpha, \beta, \gamma)$	Probability density function (pdf) of the vortex orientation
$\hat{P}(\alpha, \beta)$	Probability density function of the vortex orientation, independent of spin angle
$\mathbf{r}$	Separation vector between two points for structure function

r	Length of the separation vector $\mathbf{r}$
R_{ij}	Velocity correlation tensor
Re	Reynolds number (general)
Re_c	Reynolds number based on centerline velocity and channel halfwidth
Re_τ	Reynolds number based on wall-shear velocity u_τ and channel halfwidth h
Ro_τ	Rotation number, $Ro_\tau = 2\Omega h/u_\tau$
$\tilde{S}_{ij}$	Resolved-scale rate-of-strain tensor, $\tilde{S}_{ij} = \frac{1}{2}(\partial\tilde{U}_i/\partial x_j + \partial\tilde{U}_j/\partial x_i)$
$\mathbf{U}$, U_i	Instantaneous, total velocity vector in vector and component notation (with $i = 1, 2, 3$)
$\tilde{U}_i$	Resolved-scale velocity vector
u_i	Subgrid-scale velocity
u_i'	Fluctuation around mean velocity (in Reynolds-averaged equations)
U_m	Bulk velocity
u_τ	Wall-shear velocity (also called friction velocity)
$u_{\tau s}$	Local wall-shear velocity at suction side of rotating channel
$u_{\tau p}$	Local wall-shear velocity at pressure side of rotating channel
u_{ijk}^δ	Discrete expansion coefficients of a discrete function u^δ
$u^{\mathcal{D}}$	Component of u^δ which satisfies Dirichlet boundary condition
$u^{\mathcal{N}}$	Homogeneous component of u^δ, vanishes on Dirichlet boundary
$\breve{\mathbf{u}}$	Vector of Fourier coefficients of a function u
$\hat{\mathbf{U}}$, $\hat{\hat{\mathbf{U}}}$, $\mathbf{U}^*$	Intermediate velocities in splitting methods for time integration

$\overline{\overline{U_i'U_j'}}$	Reynolds stress tensor
$\mathbf{W}$	Weight matrix, defined for GLL discretization in (3.31)
w_i	GLL weights, see (3.16)
X	Non-dimensional cutoff wavenumber, $X = k_c\eta$
Z_{ij}	Diagonal tensor $(\frac{1}{2}, \frac{1}{2}, 0)$

Greek letters

α	Longitudinal wavenumber in Orr-Sommerfeld equation, Sec. 3.3.5
α, β, γ	Euler angles (colatitude, longitude, spin) describing orientation of vortex-fixed coordinate frame
γ_i	GLL normalization factors, see (3.17)
γ_x	Implicit correction for second-order finite-difference operator, e.g., in x-direction, see (3.10)
Δt	Timestep for numerical integration
Δ	Length scale corresponding to the cutoff wavenumber, $\Delta = \pi/k_c$
δ	Dirac delta function
δ_{xx}^2	Second-order, centered finite-difference operator for second derivative, e.g., in x-direction
ϵ	Dissipation rate per unit mass
ϵ_{ijk}	Alternating matrix (Levi-Civita symbol)
ε_{sgs}	Energy transfer from resolved scales to subgrid scale, $\varepsilon_{\text{sgs}} \equiv -\tilde{S}_{ij}\tau_{ij}$
ζ	Auxiliary variable in the solution of the Orr-Sommerfeld equation, $\zeta \equiv \partial\phi/\partial z$

η	Kolmogorov length scale
θ	Colatitude of subgrid vortex in local alignment model
Θ_{ij}	One-dimensional energy spectrum tensor
λ_1, λ_2, λ_3	Eigenvalues of resolved rate-of-strain tensor $\tilde{S}_{ij}$, $\lambda_1 < \lambda_2 < \lambda_3$
ν	Kinematic viscosity
ξ_i	Gauss-Lobatto-Legendre (GLL) points, see (3.14)
Π_k	Non-dimensional coefficients in the local-balance equation (2.44)
ρ	Density
τ_W	Shear stress at channel wall
τ_{ij}	Model subgrid-stress (SGS) tensor
ϕ	Longitude of subgrid vortex in local alignment model
$\phi(z)$	Eigenfunction of the Orr-Sommerfeld equation, Sec. 3.3.5
ψ	Angle between $\mathbf{e}^v$ and $\hat{\mathbf{n}}$
ψ'	Streamfunction of the perturbation in the Orr-Sommerfeld equation, Sec. 3.3.5
$\delta\Omega$	Boundary of domain Ω
$\delta\Omega_{\mathcal{D}}$	Domain boundary with Dirichlet conditions
$\delta\Omega_{\mathcal{N}}$	Domain boundary with Neumann conditions
Ω	Domain
ω	Vorticity
$\mathbf{\Omega}$, Ω_i	Constant angular velocity of rotating channel

Other symbols

$\langle\langle \quad \rangle\rangle$	Expectation of a function averaged over the orientation of the vortex structures
$\langle \quad \rangle$	Expectation of a function averaged over vortex orientation independent of spin angle
$^+$	Denotes quantity scaled by wall variables, see Sec. 4.2.1

List of Figures

List of Tables

Chapter 1 Introduction

Large-eddy simulation (LES) was introduced as an approach for the prediction of turbulent flows which are inaccessible to direct numerical simulation (DNS). The resolution requirements for DNS, where all length scales of the flow have to be adequately resolved, increase rapidly with increasing Reynolds number, Re, the non-dimensional parameter which is characteristic for the equations of motion of an incompressible flow (the Reynolds number can be understood as the ratio of the magnitude of the inertial force to the magnitude of the viscous force). An estimate for the rapid increase can be obtained using well-known results from dimensional analysis and basic assumptions from Kolmogorov's universal equilibrium theory (cf. Ref. 82): The length scale of the smallest structures in turbulence is given by the *Kolmogorov* scale, which is defined as $\eta \equiv (\nu^3/\epsilon)^{1/4}$, where ν is the viscosity and ϵ the dissipation. The ratio of the size ℓ of the largest eddies to the size of the smallest can then be estimated by

$$\frac{\ell}{\eta} \propto \left(\frac{u\ell}{\nu}\right)^{3/4} = Re^{3/4}, \tag{1.1}$$

where the assumption[81] has been made that the rate of dissipation taking place at the smallest scales is equal to the rate at which energy is supplied from the largest scales, so that one obtains the scaling: $\epsilon \propto u^3/\ell$. Since the width of one grid cell in a direct numerical simulation has to be of the order of the Kolmogorov scale, and the largest dimensions (the domain size) will determine ℓ, the number of gridpoints in one dimension is of the order of the ratio $\ell/\eta \propto Re^{3/4}$. For a full, three-dimensional simulation the number of gridpoints required is therefore proportional to $Re^{9/4}$. If the total computational cost is to be estimated, one also has to take into account that the timestep used for the simulation is limited and depends on the meshwidth. Therefore, the number of timesteps needed to integrate the equations of motions over a given time interval also increases approximately proportional to $Re^{3/4}$. In conclusion, one

can estimate that the computational cost of DNS is proportional to the cube of the Reynolds number.

These brief considerations may serve as an explanation why DNS of turbulent flows has been limited to low or moderate Reynolds numbers, mostly in simple geometries like a periodic box (where quite high Reynolds numbers can be reached because of special, very efficient numerical methods available for this particular case), channel flow, etc. (see Ref. 60 for a review on direct numerical simulation).

Large-eddy simulation tries to go beyond these limitations imposed by the resolution requirements for turbulent flows by directly computing only the larger scales, i.e., scales at wavenumbers smaller than some cutoff, say $k = k_c$ (k is the wavenumber), whilst the unresolved or subgrid scales and their principal physical effect on these large or resolved scales, that of providing an energy sink via energy cascade to the dissipation-range scales, are modeled.

There are many different approaches to this task — see Refs. 52, 47 and 68 for reviews. The eddy-viscosity ansatz is the earliest and remains the most widely used basis for subgrid-stress (SGS) modeling. Smagorinsky's model for the eddy viscosity, originally developed for atmospheric turbulence, has been applied extensively to engineering applications. The formulation with a fixed model constant has well-known shortcomings for wall-bounded flow and this has been largely superseded by dynamic procedures to determine the Smagorinsky constant based on double filtering.[19,49] Some mathematical inconsistencies which arise in the dynamical formulation can be resolved by casting the problem in variational form, resulting in the dynamic localization model.[20] In applications, simplified solutions to the difficulties arising in the dynamic procedure are widely used, for example plane averaging in homogeneous directions,[19] or approximate localization.[69]

A related class of SGS models are the spectral eddy-viscosity models.[43,54] This approach was extended to operate in physical space through the first use of velocity structure functions[54] as a substitute for the spectral information required to estimate the eddy viscosity. For use in large-eddy simulations,[11,18] this model has been combined with additional filtering or a switch, which selectively turns the eddy viscosity

on and off.[47]

As an alternative to eddy-viscosity models, the scale-similarity model[3] was proposed. In tests comparing the modeled subgrid stresses with those computed from DNS data (*a priori* testing), the scale-similarity model achieved much higher correlation coefficients than the Smagorinsky model. But in actual LES, it has been found that the scale-similarity model does not provide sufficient dissipation.[3,52] Nevertheless, it has been used in combination with other SGS models (e.g., the Smagorinsky model) which then provide the necessary dissipative effect.

A different approach was proposed by Leonard,[45,46] based on retaining the first terms of a formal series which expresses the result of filtering a product of two quantities solely in terms of products of the gradients of filtered quantities, thereby theoretically providing an exact closure for the (Gaussian) filtered LES equations. This is often termed the 'gradient model'. As described in Ref. 46, special regularization techniques (e.g., using particle methods) may have to be used in the numerical methods implementing this model. Alternatively the gradient model could be included in mixed models, for example with an eddy-viscosity term, as in the nonlinear model of Kosović.[36] A related idea, namely to invert the filtering operation, augmented by a procedure to generate a range of subgrid scales on a finer mesh, leads to the subgrid-scale estimation model,[15] which was originally developed in spectral space, but can also be applied in physical space.[13,14] The present paper describes continuing work on a different class of models, the so-called *stretched-vortex* SGS models.

We will consider incompressible, constant-density flow. The usual starting point for LES are the resolved-scale Navier-Stokes equations*

$$\frac{\partial \tilde{U}_i}{\partial x_i} = 0 \tag{1.2}$$

$$\frac{\partial \tilde{U}_i}{\partial t} + \frac{\partial}{\partial x_j}(\tilde{U}_i \tilde{U}_j) = -\frac{1}{\rho}\frac{\partial \tilde{P}}{\partial x_i} - \frac{\partial \tau_{ij}}{\partial x_j} + \nu \frac{\partial^2 \tilde{U}_i}{\partial x_j \partial x_j}, \tag{1.3}$$

*Note that while here we use index notation (U_1, U_2, U_3) for the velocity components, we will use (U, V, W) interchangeably if it simplifies notation. The same applies to (x, y, z) and (x_1, x_2, x_3) for coordinates in space.

where $\tilde{U}_i$ is a resolved-scale velocity field and τ_{ij} is the subgrid-stress (SGS) tensor, which represents the effect of subgrid turbulence on the resolved flow.[†] The equations (1.2) and (1.3) can be derived formally by applying a filtering operator to the full Navier-Stokes equations.[45] This filtering operation to obtain the resolved-scale velocity field cannot be performed explicitly in actual LES. Instead, the resolved field is the result of the numerical integration of (1.2) and (1.3) using a given numerical method on a grid with a given resolution whose smallest scale is much larger than the smallest turbulence scale. This requires an SGS model, which expresses τ_{ij} as a functional of the resolved-scale velocity field $\tilde{U}_i$.

One approach to the construction of SGS models is to apply certain formal properties of the filtering operation[19,21] to all physical quantities appearing in (1.3). Presently we follow a different path by considering a model which is motivated by vortex/structure-based descriptions of the fine scales of turbulence. Our aim is to construct a local model which approximates the effect of the subgrid motion on the resolved scales in a physical way. We will not attempt to either interpret or to analyse this model using elements of the filtering operation. Further, our goal is to obtain estimates for the low-order statistics of a full turbulent field which can be compared directly to results of unfiltered DNS or experimental measurement. This will usually involve an estimate of subgrid contributions to turbulence transport properties. There will be exceptions to this, which will be noted in the sequel. In summary, we seek to calculate the turbulence itself, for which the component filtered to the resolution of the numerical method may be dominant but is not complete. In this sense our approach might be described as Highly Under Resolved Turbulence Simulation (HURTS). We will attempt to follow the same approach in analyzing the turbulence transport budget.

Our model development is based on kinematics of homogeneous anisotropic turbulence generated by simple vortex structures, as originally described by Pullin and Saffmann[71] (henceforth denoted by PS). A SGS model of this type has been developed

[†]We follow here the sign convention of Ref. 71 for τ_{ij}, which is frequently used in the context of LES, although it is different from the convention used for the Reynolds-averaged equations.

and tested in LES of isotropic turbulence by Misra and Pullin,[57] henceforth refered to as MP. This original version used the energy spectrum of the resolved scales to dynamically determine model coefficients for the SGS model. In the present work, a new version of the stretched-vortex SGS model has been developed and tested, which does not require the computation of global quantities like the energy spectrum of the resolved scales. In the new version presented here, model coefficients are estimated dynamically using only localized information of the resolved field. This allows the model to be implemented more easily than earlier versions, in particular in physical-space numerical methods like finite differences where energy spectra or similar global quantities are not directly available.

The organization of the present work is as follows: In Chap. 2, the fundamental concepts of the stretched-vortex model are reviewed, and the new physical-space version is described. The numerical methods used for the simulations in this work are reviewed in Chap. 3. While a complete description of these well-known methods need not be given here, features important in the context of the present work are described in some detail. The test cases, for which large-eddy simulations with the new model have been performed, are defined, and the results for these tests are presented in Chap. 4. A discussion of the results, in particular in comparison with other SGS models, is given in Chap. 5.

Chapter 2 The stretched-vortex model

2.1 Vortex models for the fine scales of turbulence

Vortex dynamics can be used to develop models for the prediction of turbulence quantities, based on the hypothesis that one can describe certain ranges of the broad spectrum of turbulence scales as being composed of ensembles of more or less coherent laminar vortex structures.[72] Such a description is suggested by experimental evidence, both from laboratory and computational experiments, for example, Refs. 26, 42, and 85, that the fine-scale structure consists of tubes and/or sheets of vorticity, possibly sheet-like structures, which roll up to form vortex tubes.[85] (It is, however, not known presently how significant the role of these structures is in the mechanisms of turbulence, i.e., what proportion of total vorticity can be linked to the tube-like structures.) A review of vortex models for turbulence can be found in Ref. 72. The model of interest for the present work is the Lundgren stretched-spiral vortex,[50] which is of the single-vortex type, i.e., no dynamical interaction is present between individual structures. Its dynamics are a consequence of the internal structure and evolution of the model vortices. In Lundgren's model, the latter take the form of unsteady, two-dimensional spiral vortices subject to axial straining by the surrounding flowfield. This offers a richer internal structure than earlier single-vortex models by Synge and Lin,[80] based on Hill's spherical vortex, and by Townsend,[83] who used Burgers' vortices.

In polar coordinates (r, θ) in the vortex cross section, Lundgren's asymptotic solution of the vorticity equation can be written as:[72]

$$\omega(r, \theta, t) = e^{at}\hat{\omega}(\rho, \theta, \tau), \tag{2.1}$$

$$\hat{\omega}(\rho, \theta, t) = \sum_{-\infty}^{\infty} \hat{\omega}_n(\rho, \tau) \exp(in\theta), \tag{2.2}$$

with the coefficients given by:

$$\hat{\omega}_n(\rho,\tau) = f_n(\rho)\exp[-in\Omega(\rho)\tau - \nu n^2\Lambda^2(\rho)\tau^3/3], \qquad n \neq 0, \tag{2.3}$$

$$\hat{\omega}_0(\rho,\tau) = g(\rho,\tau) + f_0(\rho,\tau), \tag{2.4}$$

$$\rho(r,t) = re^{at/2}, \qquad \tau(t) = (e^{at}-1)/a, \tag{2.5}$$

where

$$\frac{1}{\rho}\frac{d}{d\rho}[\rho^2\Omega(\rho)] = f_0(\rho) + g(\rho), \qquad \text{and} \tag{2.6}$$

$$\Lambda = \frac{d\Omega}{d\rho}. \tag{2.7}$$

In (2.1)–(2.7), (ρ,τ) are stretched space and time variables, respectively, corresponding to a strictly two-dimensional evolution (i.e., no vortex stretching), $\exp(at)f_0(\rho)$ is the θ-averaged vorticity for the spiral, and $\exp(at)g(\rho)$ specifies some axisymmetric background vorticity field. The quantity a is the strain rate of the surrounding flow-field (a is taken to be constant). For $\nu \to 0$, Lundgren's solution (2.1)–(2.7) becomes a vortex sheet evolving dynamically according to the equation $\theta = \Omega(\rho)\tau$, which is of spiral form if the angular velocity $\Omega(\rho)$ is monotonically decreasing.

Lundgren further calculates the shell-summed energy spectrum for vortex structures with a vorticity distribution $\omega(r,\theta,t)$ within individual vortices. The result can be written in the form:

$$E(\kappa) = \frac{2\pi^2}{L^3}\sum_m l_m \int_0^{2\pi} \frac{1}{\kappa}|\hat{\omega}^{(m)}(\kappa\cos\theta_k, \kappa\sin\theta_k, t)|^2\, d\theta_k, \tag{2.8}$$

where L is the sidelength of a cube containing the turbulence, and the vortex structures are assumed to be composed of segments of length l_m, along which the internal vorticity distribution is independent of the coordinate along the vortex axis. In (2.8), the vorticity distribution has been written in terms of its sectional Fourier transform $\hat{\omega}^{(m)}$, see Refs. 70 and 76. As noted in Ref. 76, the energy spectrum (2.8) has the important property, that it does not depend on the orientation of the structures

(since the vorticity distribution in the structures is assumed to be independent of their orientation).

While for the present work we will only make use of (2.8), we mention here also the important result of Lundgren, who evaluated (2.8) for the stretched-spiral vortex, and, using asymptotic approximations in the evaluation of the integrals, obtained the following result for the energy spectrum of an ensemble of stretched-spiral vortices:

$$E(k) = E_0(k) + \frac{4\pi}{3}\frac{N_c l_0}{L^3} a^{1/3} k^{-5/3} \exp\left[-\frac{2\nu k^2}{3a}\right] \sum_{n=1}^{\infty} n^{-4/3} \int_0^{\infty} \frac{|f_n(\rho)|^2 \rho \, d\rho}{|\Lambda(\rho)|^{4/3}}, \qquad (2.9)$$

where N_c is the rate per unit time at which structures are created by a process outside the model, and l_0 is their initial length. The term $E_0(k)$ is the contribution to the spectrum of the $n = 0$ term in the solution for the vorticity. If the second term dominates E_0 at small wavenumbers, then (2.9) has a $k^{-5/3}$ inertial range when $k(\nu/a)^{1/2} \ll 1$. The spiral form of the vorticity solution and the vortex stretching are essential for obtaining this form of the spectrum.[72] This result is based on vortex kinematics and dynamics, and appears to be the only known result making a definite analytical connection between a $k^{-5/3}$-type spectrum and an approximate solution of the Navier-Stokes equations. As noted in connection with (2.8), the energy spectrum is independent of the vortex orientation. Therefore, in the Lundgren model, the $k^{-5/3}$ form of the spectrum does not depend on the isotropy of the small scales.

The development of vortex models, which, although resting on strong assumptions, contain local dynamics and can be analyzed kinematically, has suggested the use of vortex dynamics in the development of subgrid-stress models for LES, as will be described in the following sections.

2.2 Review of the fundamental model equations

2.2.1 Vortex structure

The concept of locally straight and nearly axisymmetric vortex structures has been generalized for the purpose of SGS modeling by PS. These subgrid elements are vortices in the sense that they provide subgrid motion only in a plane normal to the vortex axis. Finite-length effects of these "vortices" are ignored, as is any possible axial motion in the vortex cores. The proposed subgrid structure is extremely simple. Combined with the stretching strain provided by the local resolved flow, it may nevertheless be sufficient to provide a viable model of the cascade physics which are responsible for the transfer from resolved to subgrid scales.

In a vortex-fixed (Cartesian) coordinate system spanned by unit vectors $(\hat{\boldsymbol{\imath}}'_1, \hat{\boldsymbol{\imath}}'_2, \hat{\boldsymbol{\imath}}'_3)$, a vortex structure can be described in the form:

$$\boldsymbol{\omega} = \omega(x'_1, x'_2, t)\hat{\boldsymbol{\imath}}'_3, \tag{2.10}$$

where the coordinate system was chosen such that $\hat{\boldsymbol{\imath}}'_3$ is parallel to the vortex axis, and (x'_1, x'_2, x'_3) are coordinates in the vortex-fixed system. A schematic illustration of a single vortex structure in a gridcell, which is part of a much larger computational domain, is shown in Fig. 2.1.

The coordinate transformation between a coordinate system $(\hat{\boldsymbol{\imath}}_1, \hat{\boldsymbol{\imath}}_2, \hat{\boldsymbol{\imath}}_3)$, which is fixed in space ("laboratory frame"), and the vortex-fixed system $(\hat{\boldsymbol{\imath}}'_1, \hat{\boldsymbol{\imath}}'_2, \hat{\boldsymbol{\imath}}'_3)$ is described by the rotation matrix E_{ij}, which can be expressed in terms of the Euler angles α, β, and γ, where α is the angle between the x_3 and x'_3 axes (colatitude), β is longitude, and γ is spin about the x'_3 axis.

The orientation of the vortex structures will be described by the probability density function of the Euler angles $P(\alpha, \beta, \gamma)$.[71] Then the expectation of any function $f(\mathsf{E}_{ij})$ averaged over the orientations of the structures is given by:

$$\langle\langle f(\mathsf{E}_{ij})\rangle\rangle \equiv \frac{1}{8\pi^2}\int_0^{\pi}\int_0^{2\pi}\int_0^{2\pi} f(\mathsf{E}_{ij})P(\alpha,\beta,\gamma)\sin\alpha\, d\alpha\, d\beta\, d\gamma. \tag{2.11}$$

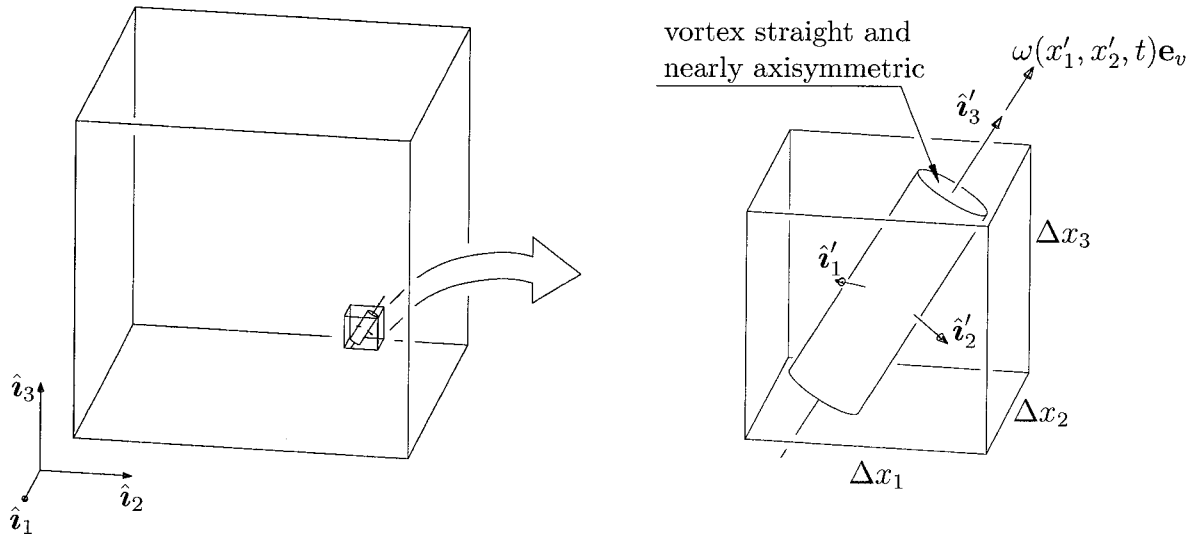

Figure 2.1: Schematic illustration of a single vortex structure in a gridcell (shown enlarged on the right) within a large computational domain.

In the special case that P is independent of the spin angle γ, it is denoted by $\hat{P}(\alpha, \beta)$, and the orientation average is written as:

$$\langle f(\mathsf{E}_{ij}) \rangle \equiv \frac{1}{4\pi} \int_0^{\pi} \int_0^{2\pi} f(\mathsf{E}_{ij}) \hat{P}(\alpha, \beta) \sin\alpha \, d\alpha \, d\beta. \tag{2.12}$$

2.2.2 Reynolds stresses and subgrid-scale stresses

The model subgrid structures established in the preceding section can now be used to obtain a kinematic result for the Reynolds stress tensor $\overline{\overline{u_i' u_j'}}$. (Here the Reynolds decomposition for the velocity U_i in a fixed reference frame is written as $U_i = \overline{\overline{U}}_i + u_i'$. The double overbar denotes an ensemble average or a volume average over a sufficiently large volume containing the turbulence.)

The vortex structures, which are assumed to generate the small-scale turbulence and thereby the Reynolds stresses, each have a vorticity distribution of the form (2.10) or, expressed in the laboratory frame, vortex m has a vorticity distribution: $\omega_i^{(m)}(\mathbf{x}, t) = \mathsf{E}_{3i} \omega^{(m)}(x_1', x_2', t)$. The vorticity correlation tensor can then be obtained by taking the sum of the contributions of all the vortex structures in a box

of volume L^3 containing the turbulence:

$$\begin{aligned}\overline{\overline{\omega_i(\mathbf{x})\omega_j(\mathbf{x}+\boldsymbol{\xi})}} =& \frac{1}{L^3}\sum_m l_m \int_{-\infty}^{\infty}\int_{-\infty}^{\infty}\int_0^{\pi}\int_0^{2\pi}\int_0^{2\pi} \\ & \times \omega^{(m)}(x_1', x_2', t)\omega^{(m)}(x_1'+\xi_1', x_2'+\xi_2', t)\mathsf{E}_{3i}\mathsf{E}_{3j} \\ & \times P(\alpha,\beta,\gamma)dx_1'\,dx_2'\,\sin\alpha\,d\alpha\,d\beta\,d\gamma.\end{aligned} \tag{2.13}$$

Here, l_m is the instantaneous length of a structure.

With the help of the relation between the vorticity spectrum tensor and the velocity spectrum tensor for homogeneous turbulence, cf. Ref. 5, the last equation can be used to obtain an expression for the one-dimensional spectrum tensor Θ_{ij}. After considerable algebra (see PS), the following expression is obtained, e.g., for the component Θ_{33}:

$$\begin{aligned}\Theta_{33}(k_3) =& \frac{1}{L^3}\sum_m l_m \int_0^{2\pi}\int_0^{\pi}\int_0^{2\pi}\int_{|k_3/\sin\alpha}^{\infty}\frac{1}{\kappa^3} \\ & \times |\hat{\omega}^{(m)}(\kappa\cos\theta_k, \kappa\sin\theta_k, t)|^2\left(\kappa^2 - \frac{k_3^2}{\sin^2\alpha}\right)^{1/2} \\ & \times \hat{P}\sin^2\alpha\,d\theta_k\,d\alpha\,d\beta\,d\kappa.\end{aligned} \tag{2.14}$$

We note that in this formula, wavenumbers for the Fourier transform in a vortex-fixed frame are expressed in polar form $(\kappa\cos\theta_k, \kappa\sin\theta_k)$ (for details see PS).

The last equation holds under the assumption that P is independent of the spin angle γ. This assumption will always be used in the following. (It does not imply that the internal and unknown vorticity distribution has to be axisymmetric. As PS note, it is reasonable to assume that all values of spin are equally likely since the vorticity within a structure will lead to rotation around the vortex axis, thereby leading to an averaging effect in azimuthal direction.)

The shell-summed energy spectrum can now be introduced in the last equation, making use of (2.8).

As discussed in the previous section, the relation (2.8) for the energy spectrum does not introduce an assumption of isotropy. This is therefore a crucial step in

the derivation: The integral effect of the unknown internal vorticity distribution in the model equation can be expressed using only the energy spectrum, which is independent of the vortex orientation, and therefore easier to model.

Now, the results for the components of Θ_{ij} can be written down. Here, we give only the results for the diagonal terms, which we will need in Sec. 2.3.1:

$$\Theta_{11}(k_3) = \frac{1}{2\pi^2}\int_0^{\pi}\int_0^{2\pi}\int_{|k_3/\sin\alpha|}^{\infty}\frac{E(\kappa)}{\kappa^2}\left[\cos^2\alpha\cos^2\beta\left(\kappa^2-\frac{k_3^2}{\sin^2\alpha}\right)^{1/2} + \sin^2\beta\frac{k_3^2}{\sin^2\alpha}\left(\kappa^2-\frac{k_3^2}{\sin^2\alpha}\right)^{-1/2}\right]\hat{P}\,d\alpha\,d\beta\,d\kappa, \tag{2.15}$$

$$\Theta_{22}(k_3) = \frac{1}{2\pi^2}\int_0^{\pi}\int_0^{2\pi}\int_{|k_3/\sin\alpha|}^{\infty}\frac{E(\kappa)}{\kappa^2}\left[\cos^2\alpha\sin^2\beta\left(\kappa^2-\frac{k_3^2}{\sin^2\alpha}\right)^{1/2} + \cos^2\beta\frac{k_3^2}{\sin^2\alpha}\left(\kappa^2-\frac{k_3^2}{\sin^2\alpha}\right)^{-1/2}\right]\hat{P}\,d\alpha\,d\beta\,d\kappa, \tag{2.16}$$

$$\Theta_{33}(k_3) = \frac{1}{2\pi^2}\int_0^{\pi}\int_0^{2\pi}\int_{|k_3/\sin\alpha|}^{\infty}\frac{E(\kappa)}{\kappa^2}\left(\kappa^2-\frac{k_3^2}{\sin^2\alpha}\right)^{1/2}\hat{P}\sin^2\alpha\,d\alpha\,d\beta\,d\kappa. \tag{2.17}$$

The Reynolds stresses are obtained from the one-dimensional spectrum tensor by carrying out the one-dimensional inverse Fourier transform $\overline{\overline{u_iu_j}} = \int\Theta_{ij}(k_3)\,dk_3$, which leads to:

$$\overline{\overline{u_iu_j}} = 2\int_0^{\infty}E(k)\,dk\,\langle \mathsf{E}_{pi}\mathsf{Z}_{pq}\mathsf{E}_{qj}\rangle, \tag{2.18}$$

where Z_{ij} is a diagonal tensor with diagonal elements $(\frac{1}{2},\frac{1}{2},0)$. We emphasize that this simple form of Z_{ij} is not an assumption made for the derivation, but is obtained as a result, if the algebra of the derivation outlined above is carried out. We also note that if the subgrid turbulence was isotropic, we would have $P\equiv 1$, and accordingly the off-diagonal components of the subgrid Reynolds-stress tensor would vanish, resulting in vanishing subgrid dissipation. This shows that SGS modeling clearly requires an anisotropic subgrid structure, i.e., $P\neq 1$ at a typical time instant.

In addition to the formal derivation, however, an intuitive explanation can also be given for this result: The velocity field generated by the vortex structure must lie in

the plane normal to the vortex axis (x_1'-x_2'-plane). Moreover, since independence of the spin angle was assumed, there is no preferred direction in that plane. Therefore, in the Reynolds stress tensor, the off-diagonal components will vanish on average, and the energy of the motion $\overline{u_k' u_k'}$ is equipartitioned between the two in-plane directions in the $x_1' x_2'$ plane. In the vortex-fixed coordinate system, the Reynolds stress tensor can accordingly be expected to take the form:

$$\overline{u_i' u_j'} = \overline{u_k' u_k'} \mathsf{Z}_{ij}. \tag{2.19}$$

(In this reference frame, the average only needs to be carried out over the cross-sectional plane of the structure. This average is denoted by a single overbar.) The last equation can now be transformed into the fixed (x_1, x_2, x_3) frame, noting that the result of the transformation is a function of E_{ij}, and therefore the average has to be taken over the statistically distributed orientations as defined in (2.12):

$$\overline{\overline{u_i u_j}} = \overline{\overline{u_k u_k}} \langle \mathsf{E}_{pi} \mathsf{Z}_{pq} \mathsf{E}_{qj} \rangle. \tag{2.20}$$

This intuitive result agrees with (2.18), which was obtained from the kinematic derivation (with $\overline{\overline{u_k u_k}} = 2 \int_0^\infty E(k)\, dk$.)

The subgrid-stress tensor is then obtained by assuming that the action of the unresolved subgrid scales on the resolved scales in LES is analogous to the action of the Reynolds stresses on the mean flow in the Reynolds-averaged Navier-Stokes equations. That is, we use an expression of the form (2.18), but include only contributions from the unresolved scales, i.e., scales with wavenumbers above a cutoff wavenumber k_c:

$$\tau_{ij} = 2 \int_{k_c}^{\infty} E(k)\, dk\, \langle \mathsf{E}_{pi} \mathsf{Z}_{pq} \mathsf{E}_{qj} \rangle. \tag{2.21}$$

This equation is the starting point for the stretched-vortex SGS model.

2.2.3 Model pdf and model energy spectrum

For the application of (2.21) in LES, the form of the pdf $\hat{P}$, which enters in the orientation average, and the form of the energy spectrum $E(k)$ need to be specified. Different choices are conceivable, but to investigate those was not the focus of the present work. Therefore, the same form of the pdf as used by MP will be applied here, and the energy spectrum will also be the same, except for a different choice of a cutoff parameter (see below).

For the vortex alignment, MP used a pdf given by the product of delta functions or a linear combination of such products of delta functions of the type

$$\hat{P}(\alpha,\beta) = \frac{4\pi}{\sin\alpha}\delta(\alpha-\theta)\delta(\beta-\phi), \tag{2.22}$$

where $\theta(\mathbf{x},t)$, $\phi(\mathbf{x},t)$ are particular Euler angles. Defining the unit vector $\mathbf{e}_v$ of the vortex axis with components

$$e_1^v = \sin\theta\cos\phi, \quad e_2^v = \sin\theta\sin\phi, \quad e_3^v = \cos\theta, \tag{2.23}$$

one can then write (2.21) in the form

$$\tau_{ij} = (\delta_{ij} - e_i^v e_j^v)\int_{k_c}^{\infty} E(k)\,dk. \tag{2.24}$$

Misra and Pullin[57,58] tested several particular models for $P(\alpha,\beta)$ including alignment with eigenvectors of the resolved rate-of-strain tensor $\tilde{S}_{ij} = \frac{1}{2}(\partial\tilde{U}_i/\partial x_j + \partial\tilde{U}_j/\partial x_i)$, alignment with the resolved vorticity vector, and a model in which the vortex alignment responded kinematically to the time-varying velocity-gradient tensor of the resolved field. Of these, the simplest model assumes that a single subgrid vortex aligns, with weighted probability, with the eigenvectors corresponding to the maximum extensional and intermediate eigenvalues of the resolved rate-of-strain tensor (see Sec. 2.3.4).

To estimate the subgrid kinetic energy $K \equiv \int_{k_c}^{\infty} E(k)\,dk$, MP assume a Kol-

mogorov form of $E(k)$ with a sharp viscous cutoff:

$$E(k) = \begin{cases} \mathcal{K}_0 \epsilon^{2/3} k^{-5/3}, & k < J/\eta \\ 0, & k > J/\eta \end{cases} \tag{2.25}$$

where $\mathcal{K}_0$ is the Kolmogorov prefactor, $\eta = (\nu^3/\epsilon)^{1/4}$ is the "local" Kolmogorov length, and J is a cutoff parameter. The concept of a local Kolmogorov length and accordingly a local dissipation ϵ has to be understood in the LES context: A gridcell in a large-eddy simulation will typically be large compared to the smallest scales in turbulence, and therefore the turbulent motions in one gridcell can be viewed as their own realization or statistical sample of turbulence, which can be described (approximately) by its own statistical quantities.

The form of the spectrum (2.25) is very simple, as is desired for the development of a tractable SGS model. Of course, the actual spectrum, for example, in the turbulent wall region of a boundary layer or channel flow has a more complicated form (see, e.g., Ref. 66 for a discussion of one-dimensional spectra in the wall region). But the test results obtained with the stretched-vortex model using (2.25) indicate, that this simplified spectrum is sufficient for the present purposes of evaluating the integral to obtain the subgrid kinetic energy K.

We also emphasize again that for stretched-vortex models of the fine scales there is no assumption of local isotropy and therefore no inconsistency in combining a Kolmogorov spectrum with local anisotropy. This is a consequence of the result derived for the one-dimensional spectrum tensor Θ_{ij}, the diagonal elements of which are given in (2.15), (2.16), and (2.17). As can be seen in these equations, the terms containing the influence of the anisotropy (i.e., terms with dependence on the vortex orientation) can be separated from the term containing the energy spectrum. The energy spectrum in turn depends only on the internal vorticity distribution, and not on the pdf $\hat{P}$, see (2.8). This can also be understood physically using the well-known relation for homogeneous anisotropic turbulence, $E(k) = E_\omega(k)/(2\,k^2)$, where E_ω is the vorticity spectrum. It is clear that for a field with straight, parallel vortex lines

(present rectilinear vortex model), the trace of the two-point vorticity correlation tensor must be independent of the orientation of these lines. It then follows that $E_\omega(k)$, and hence $E(k)$ must be independent of the vortex orientation. Thus there is no assumption of local isotropy and therefore no inconsistency in combining a Kolmogorov spectrum with local anisotropy.

Alternatives to the sharp dissipation cutoff of (2.25) would be to assume that each subgrid vortex is of the (nearly axisymmetric) stretched-spiral form, and to replace (2.25) with the Lundgren[50] spectrum (2.9), or to use an exponential cutoff near $k\eta = 1$, as suggested by DNS[31] and experiment.[75] The sharp cutoff is chosen for simplicity. The quantity J is a model parameter. A cutoff at the Kolmogorov scale $k\eta = 1$ ($J = 1$) is preferred on physical grounds but there is some analytical simplification if one lets $J \rightarrow \infty$.

Equation (2.25) contains as unknowns ϵ and $\mathcal{K}_0$. MP estimated these by first using the assumption of a local balance between the total dissipation ϵ on one side and the sum of the resolved-scale dissipation and the subgrid "dissipation" $\varepsilon_{\rm sgs}$ on the other side:

$$\epsilon = 2\nu\tilde{S}_{ij}\tilde{S}_{ij} + \varepsilon_{\rm sgs}, \quad \varepsilon_{\rm sgs} \equiv -\tilde{S}_{ij}\tau_{ij} = -K\tilde{S}_{ij}(\delta_{ij} - e_i^v e_j^v). \tag{2.26}$$

More precisely, $\varepsilon_{\rm sgs}$ represents the production of subgrid kinetic energy by the interaction between the resolved rate-of-strain tensor and the subgrid stresses, and represents therefore transfer of energy from resolved to subgrid scales. In using (2.26), it is implicitly assumed that this energy is dissipated within the local subgrid motion, and is not transferred elsewhere. This is consistent with an algebraic, zero-equation SGS model. In their dynamic version of the stretched-vortex model, MP used (2.26) and a continuity condition between resolved and subgrid spectra to obtain a (global) system of equations which could be solved for ϵ at each gridpoint and a global $\mathcal{K}_0$, thus allowing the SGS tensor to be computed from the resolved-scale quantities. For channel flow this matching was done, with appropriate kinematics, in planes defined by the two directions of flow homogeneity. This required the solution of coupled systems of

equations for the ϵ field.

One of the main objectives of the present work was to develop a localized version of the stretched-vortex model, which would allow its application to more complicated geometries using numerical methods other than global spectral methods. This requires a new method of estimating the factor $\mathcal{K}_0\epsilon^{2/3}$, which will be described in the following section, but no other changes are necessary; in particular, the use of delta function pdfs for the vortex alignment will remain unchanged.

2.3 Localized estimation of the subgrid kinetic energy in physical space

2.3.1 Structure-function relation for the stretched-vortex model with delta-function pdf

The present version makes use of the relation between the energy spectrum in Fourier space and the second-order structure functions in physical space (see, e.g., Batchelor[5]). We use the second-order structure function of the form:

$$F_2(\mathbf{r}) \equiv \overline{\overline{|\mathbf{U}(\mathbf{x}+\mathbf{r}) - \mathbf{U}(\mathbf{x})|^2}}. \tag{2.27}$$

(Note that the norm of the difference of the velocity *vectors* is used here.) The use of second-order structure functions for the estimation of SGS parameters in LES was first reported by Métais and Lesieur,[54] who used the well-known structure function relation for isotropic turbulence.

The present model does not assume isotropy of the small scales. As in the derivation of the model SGS tensor itself, a kinematic result valid for the anisotropic (model) turbulence can be derived based on the assumptions about properties of the underlying vorticity structure which have been introduced in the previous section.

The derivation uses (2.15), (2.16), and (2.17) to compute the trace of the one-

dimensional spectrum tensor:

$$\Theta_{11}+\Theta_{22}+\Theta_{33}=\frac{1}{2\pi^2}\int_0^{\pi}\int_0^{2\pi}\int_{|k_3/\sin\alpha|}^{\infty}E(\kappa)\left(\kappa^2-\frac{k_3^2}{\sin^2\alpha}\right)^{-1/2}\hat{P}\,d\alpha\,d\beta\,d\kappa. \tag{2.28}$$

As mentioned before, the delta function pdf will be used to describe the vortex alignment. After substituting the pdf from (2.22), the integration over the Euler angles can be carried out:

$$\Theta_{11}+\Theta_{22}+\Theta_{33}=\frac{2}{\pi}\int_{|k_3/\sin\theta|}^{\infty}E(\kappa)\left(\kappa^2-\frac{k_3^2}{\sin^2\theta}\right)^{-1/2}\frac{d\kappa}{\sin\theta}. \tag{2.29}$$

We recall that θ as defined in (2.23) is the angle between the three-axis (laboratory frame) and the local orientation of the subgrid-vortex structure. Performing an inverse Fourier transform in one dimension, an expression for the trace of the velocity correlation tensor for a separation $(0,0,r)$ is obtained:

$$(R_{11}+R_{22}+R_{33})(0,0,r)=\frac{2}{\pi}\int_{k_3=\infty}^{\infty}\int_{\kappa=|k_3/\sin\alpha|}^{\infty}E(\kappa)\left(\kappa^2-\frac{k_3^2}{\sin^2\theta}\right)^{-1/2}\frac{d\kappa}{\sin\theta}e^{ik_3r}dk_3. \tag{2.30}$$

In order to simplify this expression further, the order of integration has to be interchanged. The limits of integration have to be modified so that the original domain of integration is preserved. We obtain:

$$R_{11}+R_{22}+R_{33}=\frac{2}{\pi}\int_{\kappa=0}^{\infty}\frac{E(\kappa)}{\sin\theta}\int_{k_3=-\kappa\sin\theta}^{\kappa\sin\theta}\left(\kappa^2-\frac{k_3^2}{\sin^2\theta}\right)^{-1/2}e^{ik_3r}\,dk_3\,d\kappa. \tag{2.31}$$

Using the substitution $s\equiv k_3/(\kappa\sin\theta)$, the expression can be simplified:

$$R_{11}+R_{22}+R_{33}=\frac{2}{\pi}\int_{\kappa=0}^{\infty}E(\kappa)\int_{s=-1}^{1}(1-s^2)^{-1/2}e^{i\kappa sr\sin\theta}ds\,d\kappa. \tag{2.32}$$

The inner integration (over s) can be carried out analytically,[23] and one obtains:

$$R_{11} + R_{22} + R_{33} = 2 \int_0^\infty E(\kappa) \mathrm{J}_0(r\kappa \sin\theta)\, d\kappa, \tag{2.33}$$

where J_0 denotes the zeroth order Bessel function of the first kind. This result can be related to the structure function by using the relation:

$$\begin{aligned} R_{11} + R_{22} + R_{33} &= \overline{\overline{U_1^2}} + \overline{\overline{U_2^2}} + \overline{\overline{U_3^2}} - \frac{1}{2}\left[\overline{\overline{(\hat{U}_1 - U_1)^2}} + \overline{\overline{(\hat{U}_2 - U_2)^2}} + \overline{\overline{(\hat{U}_3 - U_3)^2}}\right] \\ &= 2\int_0^\infty E(k)\, dk - \frac{1}{2}\overline{\overline{|\hat{\mathbf{U}} - \mathbf{U}|^2}}.. \end{aligned} \tag{2.34}$$

Here $\hat{\mathbf{U}}$ is the velocity vector at the location $\hat{\mathbf{x}} \equiv \mathbf{x} + r\hat{\boldsymbol{\imath}}_3$. The separation vector is in the three-direction of the coordinate system because this relation will now be used in (2.33), which was derived for a separation vector aligned with this direction. This, however, is not a restriction in the application of these relations, since, for a separation $\mathbf{r}$ of arbitrary direction, we can always choose a coordinate system such that the three-axis is aligned with $\mathbf{r}$. (The trace is invariant under rotations.) The angle θ, which appears in (2.33) and in the equations that follow, is to be understood as the angle between the vortex orientation $\mathbf{e}_v$ and the separation $\mathbf{r}$. Substituting (2.34) into (2.33), we now obtain:

$$F_2(\mathbf{r};\mathbf{x}) = 4\int_0^\infty E(k)\left[1 - \mathrm{J}_0\left(rk\sin\theta\right)\right] dk. \tag{2.35}$$

We remark that for homogeneous anisotropic turbulence, F_2 is a function of the separation $\mathbf{r}$ only. In the present SGS modeling application, we will use (2.35) in a local approximation at different points on the resolved-flow grid, and retain the parametric dependence on $\mathbf{x}$.

To apply (2.35) to LES, we split the structure function of the full velocity field, $F_2(\mathbf{r};\mathbf{x})$, into a resolved-scale contribution, $\tilde{F}_2(\mathbf{r};\mathbf{x}) = \overline{\overline{|\hat{\tilde{\mathbf{U}}} - \tilde{\mathbf{U}}|^2}}$, and a subgrid con-

tribution, $F_{2,\mathrm{sgs}}(\mathbf{r};\mathbf{x})$, where

$$F_2(\mathbf{r};\mathbf{x}) = \tilde{F}_2(\mathbf{r};\mathbf{x}) + F_{2,\mathrm{sgs}}(\mathbf{r};\mathbf{x}). \tag{2.36}$$

The structure-function relation can be used to express $F_{2,\mathrm{sgs}}(\mathbf{r};\mathbf{x})$ in terms of the energy spectrum:

$$F_2(\mathbf{r};\mathbf{x}) = \tilde{F}_2(\mathbf{r};\mathbf{x}) + 4\int_{k_c}^{\infty} E(k)\left[1 - \mathrm{J}_0\left(rk\sin\theta\right)\right] dk. \tag{2.37}$$

Substituting this in (2.35) and collecting the two integrals into one, we obtain

$$\tilde{F}_2(\mathbf{r};\mathbf{x}) = 4\int_{0}^{k_c} E(k)\left[1 - \mathrm{J}_0\left(rk\sin\theta\right)\right] dk. \tag{2.38}$$

2.3.2 Model equation for $\mathcal{K}_0\epsilon^{2/3}$ using a circular average

Equation (2.38) serves as basis for the estimation of SGS parameters by use of a local average over suitable directions of $\mathbf{r}$ at each gridpoint $\mathbf{x}$. This is done presently by averaging $\tilde{F}_2(\mathbf{r};\mathbf{x})$ over a circle of radius $r = |\mathbf{r}|$ (which will depend on the local meshwidth of the computational grid) lying in a plane with normal $\hat{\mathbf{n}}$, such that $\mathbf{r}$ joins the circle center to a point on its perimeter. A sketch of the geometry is provided in Fig. 2.2. This is subsequently referred to as a *circular average*. It was chosen

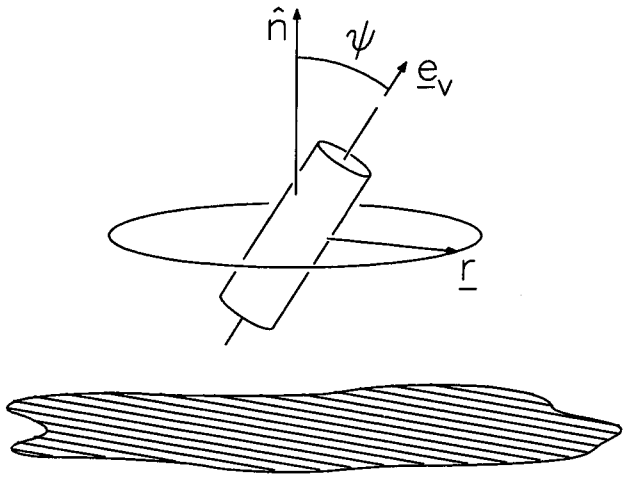

Figure 2.2: Sketch of the geometry used in the circular average of the structure function relation for the stretched-vortex model.

because it is applicable equally well to both free and wall-bounded flows, and is used for all LES reported presently. We remark that a spherical average could be used for free turbulent flows but is not suitable for near-wall flows, owing to the large shear combined with the suppression of turbulence in the sublayer. The spherical average of (2.38) is given in Appendix A, where it is demonstrated that the well-known structure-function relation for isotropic turbulence is recovered.

Applying the circular average, denoted by superscript $^{\odot}$, in (2.38) we obtain:

$$\tilde{F}_2^{\odot}(r;\mathbf{x}) = \frac{2}{\pi}\int_{\phi=0}^{2\pi}\int_{k=0}^{k_c} E(k)\left[1-\mathrm{J}_0\left(kr\sqrt{1-\sin^2\psi\cos^2\phi}\right)\right]\,dk\,d\phi. \tag{2.39}$$

The factor $\sin\theta$ in (2.38) has been expressed in terms of known quantities. We recall that θ is the angle between $\mathbf{e}_v$ and $\mathbf{r}$. From the geometrical configuration illustrated in Fig. 2.2, it follows that $\cos\theta = \sin\psi\cos\phi$, where $\cos\psi = \mathbf{e}^v\cdot\hat{\mathbf{n}}$, i.e., ψ is the angle between $\mathbf{e}^v$ and $\hat{\mathbf{n}}$. The angle ϕ is the polar angle, over which the average is taken.

2.3.3 Closure of the model

In order to make use of the last equation, we need to assume a functional form for $E(k)$. We use the same Kolmogorov spectrum with a sharp viscous cutoff as in (2.25). We note that in this case the spectrum is applied over the range $0 \le k \le k_c$. But only the integral over the spectrum enters into the model, and therefore a more detailed description of the energy spectrum is not expected to be necessary for the purposes of this model. We also note that convergence of the integral at the lower limit, i.e., $k \to 0$, is guaranteed since $1-\mathrm{J}_0(x) = O(x^2)$ as $x \to 0$. Substituting (2.25) into (2.39) and changing the integration variable to $s = k\Delta$, where Δ is the length scale at the cutoff, i.e., $k_c = \pi/\Delta$, we can solve for the unknown factor $\mathcal{K}_0\epsilon^{2/3}$:

$$\mathcal{K}_0\epsilon^{2/3} = \frac{\pi\tilde{F}_2^{\odot}(r;\mathbf{x})}{2\Delta^{2/3}\int_{\phi=0}^{2\pi}\int_{s=0}^{\pi} s^{-5/3}\left[1-\mathrm{J}_0\left(s\frac{r}{\Delta}\sqrt{1-\sin^2\psi\cos^2\phi}\right)\right]\,ds\,d\phi}. \tag{2.40}$$

In (2.40), r and Δ are related to the local mesh size of the (possibly non-uniform) computational grid (see Sec. 2.3.4). All other quantities on the right-hand side can

be estimated from the resolved-scale velocity field. The integral in the denominator is a function of r/Δ and ψ. Methods for an effective implementation of (2.40) in large-eddy simulations are discussed in Sec. 2.3.4.

The limits of integration in (2.40) apply only for $k_c < J\eta^{-1}$ owing to the viscous cutoff in the model energy spectrum (2.25). (We recall that η is understood as a "local," gridcell Kolmogorov scale in LES.) In the model implementation, the cases $k_c < J\eta^{-1}$ and $k_c > J\eta^{-1}$ have to be distinguished unless a simplified form of the spectrum with a $k^{-5/3}$ range extending to infinity is used, $J \to \infty$. This latter choice simplifies the model significantly.

Formulation for $J \to \infty$

The group $\mathcal{K}_0\epsilon^{2/3}$ is obtained from (2.40), which is valid at all locations for this case. The (estimated) subgrid kinetic energy then follows from (2.25):

$$K = \frac{3}{2}\mathcal{K}_0\epsilon^{2/3}k_c^{-2/3}. \tag{2.41}$$

An estimate for η is not required. All quantities in (2.24) are known, and the SGS tensor τ_{ij} can now be computed.

Formulation for finite J

The model equations can also be closed for finite J, but the complexity of the resulting model version is somewhat increased compared to the $J \to \infty$ version. The local-balance equation (2.26) is used. The subgrid kinetic energy is now

$$\begin{aligned} K &= \frac{3\mathcal{K}_0\epsilon^{2/3}}{2k_c^{2/3}}\left[1-\left(\frac{k_c\eta}{J}\right)^{2/3}\right], \quad k_c < J\eta^{-1} \\ &= 0, \qquad\qquad\qquad\qquad\quad k_c > J\eta^{-1}. \end{aligned} \tag{2.42}$$

Since the subgrid kinetic energy vanishes for $k_c > J\eta^{-1}$, the SGS tensor will vanish accordingly. If $K = 0$ for a grid cell, this means that locally all the energy is contained in the resolved scales, i.e., all relevant turbulence scales are resolved at that location,

and no model contribution is needed.

Since η is not known *a priori* in a cell, we first calculate the product $k_c\eta$ and then test for $k_c\eta \lesseqgtr J$. For $k_c\eta < J$, substituting K from (2.42) into (2.26) yields

$$\epsilon = 2\nu\tilde{S}_{ij}\tilde{S}_{ij} - \frac{3\mathcal{K}_0\epsilon^{2/3}}{2k_c^{2/3}}\left[1-\left(\frac{k_c\eta}{J}\right)^{2/3}\right]\tilde{S}_{ij}(\delta_{ij}-e_i^v e_j^v), \qquad k_c\eta < J. \tag{2.43}$$

This can be written as

$$1 - \Pi_1 X^4 + 3\Pi_2\,\Pi_3 X^4\left[1-\left(\frac{X}{J}\right)^{2/3}\right] = 0, \qquad X < J, \tag{2.44}$$

where

$$\begin{aligned} X &\equiv k_c\eta = k_c\left(\frac{\nu^3}{\epsilon}\right)^{1/4}, \qquad \Pi_1 \equiv \frac{2\tilde{S}_{ij}\tilde{S}_{ij}}{(k_c^4\nu^2)}, \\ \Pi_2 &\equiv \frac{\mathcal{K}_0\epsilon^{2/3}}{k_c^{8/3}\nu^2}, \qquad \Pi_3 \equiv \frac{\tilde{S}_{ij}(\delta_{ij}-e_i^v e_j^v)}{(2k_c^2\nu)}. \end{aligned} \tag{2.45}$$

Note that the group $\mathcal{K}_0\epsilon^{2/3}$ is preserved in Π_2. The parameter Π_1 is essentially twice the square of the grid-scale Reynolds number. It follows from (2.26) and (2.45) that $\Pi_3 < 0$ corresponds to transfer from resolved to subgrid scales (cascade) while $\Pi_3 > 0$ corresponds to transfer to resolved scales (backscatter). Given $\mathcal{K}_0\epsilon^{2/3}$ from (2.40), then (2.44) can be solved for X by Newton's method at each gridpoint, and it is not necessary to solve a coupled system for either the whole domain, or along homogeneous flow directions. The subgrid kinetic energy and therefore the SGS tensor can then be computed for $X < J$. When $X > J$, the flow is estimated to be locally resolved ($k_c > J\eta^{-1}$) and the SGS tensor is set to zero. We remark that this is a smooth transition at $X = J$ with no discontinuity in τ_{ij}. A brief analysis of (2.44) is given in Appendix C.

2.3.4 Notes on model implementation

The model implementation is similar for all numerical methods used, both for decaying isotropic turbulence and channel flow. As input, the model needs the local $\tilde{U}_i$ and $\partial\tilde{U}_i/\partial x_j$. The first step is to compute $\tilde{F}_2^{\odot}$ at each grid point. This is done by approximating the circular average by an average over the four neighboring grid points in the plane. To account for non-uniform grids, we invoke Kolmogorov's inertial-range form[35] $F_2 \sim (\epsilon r)^{2/3}$, which also follows from (2.25) and (2.35) without additional assumptions. This method was also used by Lesieur and Métais.[47] For all present LES, the circular average is performed in a plane normal to the three-direction (wall-normal for channel flow), and we obtain

$$\tilde{F}_2^{\odot} = \frac{1}{4}\sum_{k=1,2}\Bigg[\left\|\tilde{\mathbf{U}}(\mathbf{x}) - \tilde{\mathbf{U}}(\mathbf{x}+\Delta x_k^+\hat{\boldsymbol{\imath}}_k)\right\|^2 \left(\frac{r}{\Delta x_k^+}\right)^{2/3} + \left\|\tilde{\mathbf{U}}(\mathbf{x}) - \tilde{\mathbf{U}}(\mathbf{x}-\Delta x_k^-\hat{\boldsymbol{\imath}}_k)\right\|^2 \left(\frac{r}{\Delta x_k^-}\right)^{2/3}\Bigg], \tag{2.46}$$

where Δx_k^+ and Δx_k^- are the grid spacing in positive and negative k-direction, respectively (for the numerical methods used in the present work, $\Delta x_k^+ = \Delta x_k^-$ for $k = 1, 2$). The separation length for the structure function is set to $r = \sqrt{\Delta x_1 \Delta x_2}$, i.e., the geometric mean of the grid spacings in the (x_1, x_2)-plane where the structure function is computed.

Next, the orientation of the subgrid-vortex structures is determined. We assume alignment with eigenvectors of the resolved rate-of-strain tensor $\tilde{S}_{ij} = (\partial\tilde{U}_i/\partial x_j + \partial\tilde{U}_j/\partial x_i)/2$. Given the eigenvectors $\tilde{\mathbf{e}}_1$, $\tilde{\mathbf{e}}_2$, and $\tilde{\mathbf{e}}_3$ of $\tilde{S}_{ij}$, with corresponding eigenvalues $\lambda_1 < \lambda_2 < \lambda_3$, we will use versions of the model, where the subgrid structures are assumed to be aligned with $\tilde{\mathbf{e}}_3$ only ($\tilde{\mathbf{e}}_3$ model), or where a fraction $\lambda \equiv \lambda_3/(|\lambda_2| + \lambda_3)$ of the structures is aligned with $\tilde{\mathbf{e}}_3$, and the remainder $(1-\lambda)$ with $\tilde{\mathbf{e}}_2$ ($\tilde{\mathbf{e}}_2 + \tilde{\mathbf{e}}_3$ model). These versions, which use alignment with eigenvectors of $\tilde{S}_{ij}$ only, do not model backscatter. In Ref. 57, other versions which include backscatter, e.g., using partial alignment with the resolved-scale vorticity vector, have been tested. But no

significant improvements in the results of the simulations presented in the following would be expected by using different alignments.

Equation (2.40) can now be evaluated using (2.46). The integral in the denominator of (2.40) depends on ψ and r/Δ. Presently, an analytical approximation to the integral is used (see Appendix B). An alternative would be to use a two-dimensional table lookup. The angle ψ is known from the subgrid-vortex orientation. The ratio r/Δ is the ratio of the separation length r used for the structure function and the cutoff length scale Δ ($k_c = \pi/\Delta$). In the present work, $\Delta = (\Delta z^+ + \Delta z^-)/2$ is used, i.e., the average of the distances to the two neighboring points in positive and negative z-direction.

When $J \to \infty$, the subgrid kinetic energy can be obtained immediately from (2.41). A step-by-step overview for the $J \to \infty$ version of the model is given in Table 2.1.

Table 2.1: List of steps for estimating the SGS tensor τ_{ij} with the $J \to \infty$ version of the model (assumes that plane of circular average is normal to three-direction).

Input: Resolved-scale velocity field $\tilde{U}$,
resolved-scale rate-of-strain tensor $\tilde{S}_{ij} = \frac{1}{2}(\partial\tilde{U}_i/\partial x_j + \partial\tilde{U}_j/\partial x_i)$

For each gridpoint:

compute resolved-scale structure function $\tilde{F}_2^{\odot}$ from (2.46)

solve eigenvalue-problem for $\tilde{S}_{ij}$: eigenvalues $\lambda_1 < \lambda_2 < \lambda_3$ and corresponding eigenvectors $\tilde{e}_1$, $\tilde{e}_2$, $\tilde{e}_3$.

set alignment fraction:
$\lambda \equiv 1$ for $\tilde{\mathbf{e}}_3$ model,
$\lambda \equiv \lambda_3/(|\lambda_2| + \lambda_3)$ for $\tilde{\mathbf{e}}_2 + \tilde{\mathbf{e}}_3$ model.

compute $\mathcal{K}_0\epsilon^{2/3}$ from (2.40): determine alignment factor $\sin^2\psi$ using
$\cos^2\psi = \sqrt{\lambda\tilde{e}_{3z}^2 + (1-\lambda)\tilde{e}_{2z}^2}$,
determine r/Δ with
$r \equiv \sqrt{\Delta x \Delta y}$ and
$\Delta \equiv (\Delta z^+ + \Delta z^-)/2$,
evaluate (B.8) to approximate integral,
and then evaluate (2.40).

compute subgrid kinetic energy K from (2.41), using $k_c = \pi/\Delta$.

compute SGS tensor: $\tau_{ij} = K\left[\lambda\left(\delta_{ij} - \tilde{e}_{3i}\tilde{e}_{3j}\right) + (1-\lambda)\left(\delta_{ij} - \tilde{e}_{2i}\tilde{e}_{2j}\right)\right]$.

Output: Subgrid-stress tensor τ_{ij}

For finite J, (2.44) has to be solved. This can be done efficiently with a Newton solver, for which an initial value is obtained by an analytical approximation; see Appendix C for details. When X is known, K can be obtained from (2.42) and other quantities including $\mathcal{K}_0$ can be determined. The SGS stress tensor τ_{ij} then follows from (2.24). The steps to compute the SGS tensor using a model version with finite J are summarized in Table 2.2.

Table 2.2: List of steps for model version with finite J (assumes that plane of circular average is normal to three-direction).

Input: Resolved-scale velocity field $\tilde{U}$,
resolved-scale rate-of-strain tensor $\tilde{S}_{ij} = \frac{1}{2}(\partial\tilde{U}_i/\partial x_j + \partial\tilde{U}_j/\partial x_i)$

For each gridpoint:
compute resolved-scale structure function $\tilde{F}_2^{\odot}$ from (2.46)
solve eigenvalue problem for $\tilde{S}_{ij}$: eigenvalues $\lambda_1 < \lambda_2 < \lambda_3$ and corresponding eigenvectors $\tilde{e}_1$, $\tilde{e}_2$, $\tilde{e}_3$.
set alignment fraction: $\lambda \equiv 1$ for $\tilde{\mathbf{e}}_3$ model,
$\lambda \equiv \lambda_3/(|\lambda_2| + \lambda_3)$ for $\tilde{\mathbf{e}}_2 + \tilde{\mathbf{e}}_3$ model.
Assume $k_c\eta < J$
compute $\mathcal{K}_0\epsilon^{2/3}$ from (2.40): as in $J \to \infty$ version, Table 2.1.
Compute Π_1, Π_2, Π_3, cf. (2.45).
If (2.44) has no real solution for these values of Π_1, Π_2, Π_3:
set $\tau_{ij} = 0$, continue with next gridpoint.
(clipping, in praxis rarely necessary, cf. Appendix C)
Obtain initial value for Newton solver, cf. Appendix C.
Solve (2.44) using Newton's method.
If $X > J$, flow is locally resolved: $\tau_{ij} = 0$,
continue with next gridpoint
Compute subgrid kinetic energy from (2.42).
Compute SGS tensor from (2.24) as in $J \to \infty$ version, Table 2.1.

Output: Subgrid-stress tensor τ_{ij}

Chapter 3 Numerical methods

3.1 Pseudospectral method for homogeneous turbulence

The numerical method for testing the SGS model in decaying isotropic turbulence is based on a standard finite-dimensional Fourier expansion of the velocity field. It is based on the method used by Rogallo[73] and the earlier work by Orszag and Patterson.[65] The implementation used for the present work is the same as in Ref. 56, where a brief description of the method can also be found.

We only note the characteristic properties of this method which make it computationally very efficient: The divergence-free condition reduces in Fourier space to the condition $\mathbf{k} \cdot \mathbf{U_k} = 0$, where $\mathbf{U_k}$ are the expansion coefficients of the velocity field as defined in a three-dimensional, discrete Fourier transformation. This allows to implement the divergence-free condition by using the projection operator into the subspace orthogonal to the wavenumber vector $\mathbf{k}$. The nonlinear term is computed in physical space (hence the method is refered to as pseudospectral).

This can lead to *aliasing errors*, which arise when the highest, energy-rich modes created by a nonlinear product cannot be resolved by the finite number of modes used in the discretization, and are folded back into the range of resolved modes. The problem can easily be investigated in one dimension:[8] If $u(x)$ and $v(x)$ are two functions which are given by their discrete Fourier coefficients $\check{u}_k$ and $\check{v}_k$, and the product $w(x) = u(x)v(x)$ is to be computed in physical space, the result, described by its Fourier coefficients, will be:

$$\check{w}_k = \frac{1}{N} \sum_{j=0}^{N-1} u_j v_j e^{-ikx_j}, \quad k = -\frac{N}{2}, \ldots, \frac{N}{2} - 1 \tag{3.1}$$

with $u_j = \sum_{k=-N/2}^{N/2-1} \check{u}_k e^{ikx_j}$ for $j = 0, 1, \ldots, N-1$, and v_j defined analogously. Substituting the expressions for u_j and v_j into the product and using the orthogonality relation:

$$\frac{1}{N}\sum_{j=0}^{N-1} e^{ipx_j} = \begin{cases} 1 & \text{if } p = Nm,\ m = 0, \pm 1, \pm 2, \ldots \\ 0 & \text{otherwise,} \end{cases} \tag{3.2}$$

the product can be written as:

$$\check{w}_k = \sum_{m+n=k} \check{u}_m \check{v}_n + \sum_{m+n=k\pm N} \check{u}_m \check{v}_n \tag{3.3}$$

where the first term on the right-hand side is the representation of the product in a finite-dimensional Fourier expansion, and the second term is the aliasing error. As can be inferred from this expression, and confirmed in actual computations, the aliasing error is dominated by the influence of the highest resolved modes. If the energy contents in these modes is high, aliasing errors can have a significant, adverse influence on the quality of the results of a numerical simulation. This applies, in particular, to large-eddy simulations, where the smallest resolved scales are typically far larger than the dissipation-range scales, and therefore contain significant amounts of energy. Fully-resolved direct numerical simulations should be less affected by the problem of aliasing errors.

For the present LES of isotropic turbulence, we follow the "3/2-rule"[8] to remove aliasing errors. This technique adds additional modes, which are set to zero initially, to the Fourier representation of the two functions $u(x)$ and $v(x)$ before they are transformed to physical space for the evaluation of the product. The transform uses now M rather than N points, with $M \geq 3N/2$. Denoting padded quantities with a superscript *, we have:

$$\check{w}_k^* = \frac{1}{M}\sum_{j=0}^{M-1} u_j^* v_j^* e^{-ikx_j}, \quad k = -\frac{M}{2}, \ldots, \frac{M}{2} - 1 \tag{3.4}$$

with $u_j^* = \sum_{k=-M/2}^{M/2-1} \check{u}_k^* e^{ikx_j}$ for $j = 0, 1, \ldots, M-1$, where

$$\check{u}_k^* = \begin{cases} \check{u}_k & \text{for } k = -\frac{N}{2}, \ldots, \frac{N}{2} - 1 \\ 0 & \text{otherwise,} \end{cases} \tag{3.5}$$

and v_j^* defined analogously. Similarly as in (3.3), we can write for the padded product:

$$\check{w}_k^* = \sum_{m+n=k} \check{u}_m^* \check{v}_n^* + \sum_{m+n=k\pm M} \check{u}_m^* \check{v}_n^*, \tag{3.6}$$

but note that the condition for the contributions to the aliasing term is different here. Now, we recall that the range of resolved modes is $k = -N/2, \ldots, N/2 - 1$. But it is easy to see from (3.6) that aliasing errors can only effect modes outside the range of resolved scales. We take, e.g., the worst case of the highest resolved mode $k = -N/2$: The second term in (3.6) could only add an aliasing error to this mode if $m + n = -N/2 + M = N$ (setting $M = 3N/2$). This can only be true if at least one of the two factors is a mode outside the range of resolved scales: $m \geq N/2$ and/or $n \geq N/2$. Then, from (3.5), it is clear that at least one of the factors in the aliasing term in (3.6) is zero. Therefore, even for the highest resolved mode, no aliasing error is added. The aliasing errors can only affect modes outside the range of resolved scales, and these modes are discarded after evaluating the product, since they are not part of the discrete representation of the physical quantity, but have only been added as part of the de-aliasing procedure. The de-aliasing, therefore, has an important effect on the correct representation of the nonlinear transfer across the cutoff between resolved and subgrid scales, but no valid contributions of the nonlinear term to the resolved scales are removed, and in that sense the de-aliasing does not introduce any artificial dissipation.

In three dimensions, the padding at the beginning of the nonlinear step and the removal of the additional modes at the end is performed for all three directions. In the numerical method for isotropic turbulence, the Fourier coefficients are also subjected to spherical truncation (cf. Ref. 8).

The temporal integration of the equation uses an integrating factor technique for the diffusion operator and a Runge-Kutta scheme for the nonlinear term.

3.2 Compact finite-difference method for homogeneous turbulence

Finite-difference methods, which can be generalized if the discrete differentiation operators are allowed to be implicit, have been reviewed and analyzed in Ref. 44. In this reference, the term "compact finite differences" is used for derivative operators, which have improved resolution characteristics for high wavenumber modes, and which represent the discrete derivatives in implicit form, but with relatively small stencil sizes (hence the name "compact"). The implicit representation contributes to a tighter coupling between the nodes of the stencil, which is responsible for the improved resolution characteristics. But it also means that a linear system has to be solved to obtain the values of the discrete derivatives to be computed.

A code has been developed to simulate incompressible flow in a periodic box using a compact finite-difference discretization. This code was not intended to be an alternative to the pseudospectral method described in the previous section. Of course, the efficiency of the pseudospectral Fourier method for this particular geometry is unsurpassed. The purpose of this code was twofold: First, to test a particular pressure-correction scheme for use with compact finite differences (which have the theoretical potential of being applied to more general geometries), and, second, to test the SGS model developed in this work in a numerical method operating entirely in physical space.

3.2.1 Discretization schemes

The numerical method in the present work uses compact finite differences in all three spatial directions. The finite-difference scheme itself is the same as described in Ref. 77, but in this reference it was only applied in one spatial dimension.

The first derivative on a staggered mesh, as used here in all three dimensions, is given by:

$$\frac{h}{24}(22f'_k + f'_{k+1} + f'_{k-1}) = f_{k+1/2} - f_{k-1/2}. \tag{3.7}$$

The leading term in the truncation error for this scheme is of fourth order, but due to the implicit form of the scheme, the dispersion error for this scheme at higher wavenumbers will be smaller than for standard, centered finite differences of fourth order (c.f. Ref. 44).

For the second derivatives in the viscous term, a special treatment is used, again following Ref. 77, to simplify the operators for the viscous term, which will be advanced by an implicit timestepping method. This fourth-order accurate expression for the second derivative is given by:

$$f'' = \delta^2(f) + \gamma(f), \tag{3.8}$$

where δ^2 denotes the standard second-order, centered finite difference operator, and γ is an implicit correction using values of the first derivative:

$$\delta^2(f_k) = \frac{f_{k+1} + f_{k-1} - 2f_k}{h^2}, \tag{3.9}$$

$$\gamma(f_k) = \frac{f_{k+1} + f_{k-1} - 2f_k}{h^2} - \frac{f'_{k+1} - f'_{k-1}}{2h}. \tag{3.10}$$

Applied to the viscous term, only the explicit part of the Laplacian, $\delta^2_{xx} + \delta^2_{yy} + \delta^2_{zz}$ (where, e.g., δ^2_{xx} means that the operator δ^2 is applied in x-direction), is advanced by the Crank-Nicholson scheme, while the correction terms γ are treated together with the nonlinear term using the Adams-Bashforth scheme (see below).

3.2.2 Time integration using a splitting method with the internal iterations technique

Splitting methods, which are widely used for the numerical integration of the Navier-Stokes equations for incompressible flow, perform the time integration of the nonlinear, pressure, and viscous terms in separate steps. Typically the nonlinear term in the Navier-Stokes equation is integrated in the first step. The resulting intermediate velocity $\hat{\mathbf{U}}$, however, is not divergence-free. Therefore, a pressure correction with a scalar field Φ is applied in the form (in general):

$$\frac{\hat{\hat{\mathbf{U}}}^{n+1} - \hat{\mathbf{U}}^{n+1}}{\Delta t} = -\mathbf{G}\Phi^{n+1}, \tag{3.11}$$

where $\mathbf{G}$ denotes the discrete gradient operator consistent with the chosen approximation scheme for the derivatives. Φ is determined by requiring that the corrected velocity field be divergence-free, $\mathbf{D} \cdot \hat{\hat{\mathbf{U}}}^{n+1} = 0$ ($\mathbf{D}$ is the discrete divergence operator). Applying the operator $\mathbf{D}$ to (3.11), one obtains an equation for Φ:

$$\mathbf{D} \cdot \mathbf{G}\Phi^{n+1} = \frac{1}{\Delta t}\mathbf{D} \cdot \hat{\mathbf{U}}^{n+1}. \tag{3.12}$$

The operator $\mathbf{D} \cdot \mathbf{G}$ has to be consistent with the first derivative operator used in (3.11). But the use of compact finite-difference schemes has the effect that the discrete operator $\mathbf{D} \cdot \mathbf{G}$ will be a rather densely populated matrix which makes it computationally expensive to invert.

One possible way to perform the pressure correction step at a reasonable computational cost is the internal iterations technique by Schiestel and Viazzo.[77] Instead of solving the full equation (3.12), the left-hand side is replaced by a discrete Laplace operator, which uses the explicit, centered, second-order finite-difference scheme. The resulting matrix is sparse and can be inverted using available solvers for such systems. However, since this equation is not consistent with the discretization scheme used for the first derivatives, the corrected velocity will still not be divergence-free. Therefore,

within each timestep, an iteration has to be performed until the incompressibility condition is satisfied (within a specified tolerance level.) The viscous term is also included in this internal iteration. To summarize, the algorithm to perform internal iteration $m-1 \rightarrow m$ for timestep $n \rightarrow n+1$ is given in the following:

$$\begin{aligned}\frac{\hat{\mathbf{U}}^{n+1,m}-\mathbf{U}^{n}}{\Delta t} = & \underbrace{\frac{1}{2}(3\mathbf{N}^{n}-\mathbf{N}^{n-1})+\frac{1}{2}(\gamma_x+\gamma_y+\gamma_z)(3\mathbf{U}^{n}-\mathbf{U}^{n-1})}_{\text{Adams-Bashforth}} \\ & -\mathbf{G}P^{n+1,m-1} \\ & +\underbrace{\frac{1}{2Re}(\delta_{xx}^2+\delta_{yy}^2+\delta_{zz}^2)(\mathbf{U}^{n+1,m-1}+\mathbf{U}^{n})}_{\text{Crank-Nicholson}}\end{aligned}$$

$$\begin{aligned}(\delta_{xx}^2+\delta_{yy}^2+\delta_{zz}^2)\Phi^{n+1,m} &= \frac{1}{\Delta t}\mathbf{D}\cdot\hat{\mathbf{U}}^{n+1,m} \\ \frac{1}{\Delta t}(\mathbf{U}^{n+1,m}-\hat{\mathbf{U}}^{n+1,m}) &= -\mathbf{G}\Phi^{n+1,m} \\ P^{n+1,m} &= \Phi^{n+1,m}+P^{n+1,m-1}.\end{aligned}$$

Here, $\mathbf{N}$ denotes the nonlinear term of the momentum equation (1.3) (the divergence form is used in the present work).

3.2.3 Implementation

The numerical method described in the preceding sections has been implemented on a fully staggered grid. The pressure correction is computed at the center of each grid cell, while each velocity component is computed on the cell face, which is normal to the corresponding coordinate direction.

For the interpolations made necessary by the use of the staggered grid, an implicit scheme as given in[44] is used:

$$f_i+\frac{3}{10}(f_{i+1}+f_{i-1}) = \frac{1}{20}(f_{i+3/2}+f_{i-3/2})+\frac{3}{4}(f_{i+1/2}+f_{i-1/2}). \tag{3.13}$$

Both, this interpolation scheme and the implicit first derivative operators require

the inversion of a tridiagonal matrix. In the present code, which uses only periodic boundary conditions, this inversion is performed using a fast-transform solver.

The (simplified) Poisson operator is inverted using a conjugate gradient solver with incomplete Cholesky factorization (see Ref. 22 for a description of these methods). For the present implementation, routines from the `DLAP` package[78] have been used.

The compact finite-difference code has been tested by simulating the early-time behaviour of the Taylor-Green vortex flow and comparing the results with those of Ref. 7.

3.3 Nodal(GLL)/Fourier method for channel flow

Incompressible flow in an open channel is a widely used testcase for the behaviour of a SGS model in wall-bounded turbulence. Tests for the present work have been performed with versions of the code of Ref. 9.

For the two homogeneous directions, which exist in this case, Fourier expansions can be used. Various discretization schemes have been used for the third, wall-normal direction, e.g., Chebychev polynomials,[34] and B-splines.[40] For the present work, Lagrange polynomials through the Gauss-Lobatto-Legendre (GLL) points are used.[8,30] The $(N+1)$ GLL points for expansion polynomials of order N are given by

$$\xi_0 = -1, \quad \xi_N = 1, \quad L'_N(\xi_j) = 0 \text{ for } j = 1, \ldots, N-1, \tag{3.14}$$

where L_k denotes the Legendre polynomial of order k. The basis functions of the expansion are then given by:

$$h_j(\xi) = \frac{(\xi-1)(\xi+1)L'_N(\xi)}{N(N+1)L_N(\xi_j)(\xi-\xi_j)}, \qquad j = 0, \ldots, N, \tag{3.15}$$

where ξ_j are the GLL points defined in (3.14). These interpolation points are defined in the context of the quadrature rule[8,30] of the same name, and are associated with

corresponding weights:

$$w_i \equiv \frac{2}{N_z(N_z+1)[L_{N_z}(\xi_i)]^2}, \quad i = 0, \ldots, N_z - 1 \tag{3.16}$$

and normalization factors:

$$\gamma_k = (k + \frac{1}{2})^{-1} \qquad \text{for } k < N \tag{3.17}$$
$$\gamma_N = 2/N$$

which will be needed in the following sections.

The basis (3.15) is called a *nodal* basis. Nodal bases are invariably made up of Lagrange polynomials, which are in general form given by

$$\Phi_p(x) = \frac{\prod_{q=0, q\neq p}^{N}(x - x_q)}{\prod_{q=0, q\neq p}^{N}(x_p - x_q)}, \qquad p = 0, \ldots, N. \tag{3.18}$$

They have the property that $\Phi_p(x_q) = \delta_{pq}$, where δ_{ij} is the Kronecker delta. In particular, $h_p(\xi_q) = \delta_{pq}$, cf. (3.15). This means that no transforms have to be performed to obtain the physical values at the nodes if a function is discretized using a Lagrange polynomial basis. The nodal GLL basis functions play an important role in the context of spectral element methods. The main advantage of this particular basis is that because of the connection with the Gauss-type quadrature, integrals (as arise in the method of weighted residuals) can be efficiently evaluated numerically with sufficiently high accuracy.

In particular, the inner product $(h_p, h_q) = \int_\Omega h_p(\xi) h_q(\xi)\, d\xi$, which is known as *mass* matrix and plays an important role in the method of weighted residuals, is advantageously evaluated using the Gauss-Lobatto-Legendre quadrature rule for $(N+1)$ points. The resulting (approximate) mass matrix is diagonal, which is very helpful for computational efficiency. This result is not exact, but rather corresponds to the practice of lumping the mass matrix, which is used in finite element methods, i.e., summing the rows and using the sum as the entry of a diagonal matrix.[30] The error

incurred by this effective lumping due to the use of the reduced-order quadrature is consistent with the approximation error of the expansion.

3.3.1 Spatial discretization

In the following, we describe the formulation for the advection and diffusion terms of the Navier-Stokes equations for a hybrid Fourier/GLL-basis representation of the solution fields. The nonlinear advection operator and the linear diffusion operator will be denoted by **N** and **L**:

$$\mathbf{N}(\mathbf{U}) \equiv -\frac{1}{2}\left[\mathbf{U}\cdot\nabla\mathbf{U} + \nabla\cdot(\mathbf{U}\mathbf{U})\right], \tag{3.19}$$

$$\mathbf{L}(\mathbf{U}) \equiv \frac{1}{Re}\nabla^2\mathbf{U}. \tag{3.20}$$

(The so-called skewsymmetric form of the nonlinear term is used, cf. Ref. 38.)

For the channel flow simulations, the polynomial expansion using basis vectors of the form (3.15) is used in one dimension (wall-normal direction), and Fourier expansions are used in the two homogeneous directions (streamwise and spanwise). The numerical representation u^δ of any flow variable u is therefore discretized in the form:

$$u^\delta(x,y,z) = \sum_{q=0}^{N_z}\sum_{p=-N_y/2}^{N_y/2-1}\sum_{m=-N_x/2}^{N_x/2-1} u^\delta_{mpq} e^{2\pi i(mx/L_x+py/L_y)} h_q(\chi^{-1}(z)), \tag{3.21}$$

where (N_x, N_y, N_z) are the number of GLL/Fourier-"modes" used in the respective coordinate directions, u^δ_{ijk} is the discrete expansion coefficient at node (i,j,k), and the domain has dimensions L_x and L_y in streamwise and spanwise direction, respectively. Furthermore, we have used the mapping function χ which maps the standard element $[-1,1]$ (in one dimension) into the physical domain: $z = \chi(\xi)$ where $\xi \in [-1,1]$. (In general, it is advantageous to define the function χ using isoparametric mapping.[28,30] This will not be described here, since for the simple geometry of the channel flow, the upper and lower wall are typically located at $z = -1$ and $z = 1$, which is identical to

the standard domain $-1 \leq \xi \leq 1$. The mapping is therefore an identity: $z \equiv \xi$, and will not be considered any further in the following.)

Nonlinear term

The nonlinearity in the advection term requires an explicit time-integration of this term in physical space for reasons of computational efficiency. Inverse Fourier transforms have to be performed in the homogeneous directions to obtain the polynomial expansion coefficients in physical space, which are equivalent to the nodal values of $\mathbf{U}^\delta$ (because of the use of Lagrange interpolants). The values of the nonlinear products can then be computed at the nodes, i.e., the nonlinear term is evaluated by a *collocation*-type method.

The treatment of the nonlinear term is therefore quite straightforward, except that aliasing errors can be introduced because the nonlinear product is evaluated in physical space and then transformed back to a spectral representation.

For the present LES of channel flow, a version of the code has been developed that uses the "2/3-rule"[8] for aliasing removal in the Fourier expansions in the two homogeneous directions. This technique is essentially the same as the "3/2"-rule which was discussed in Sec. 3.1. The number of modes is not expanded for the evaluation of the nonlinear term, however; instead, the upper one-third of the total number of modes is used only for de-aliasing purposes, but is retained throughout the computation. Only the lower two-thirds of the total number of modes constitute the resolved scales. In other words, the nonlinear term is evaluated for the full $N_x \times N_y$ modes, and then all those modes (p, q) are set to zero, for which:

$$\left(\frac{p}{\frac{2}{3}\frac{N_x}{2}} \right)^2 + \left(\frac{q}{\frac{2}{3}\frac{N_y}{2}} \right)^2 \geq 1. \tag{3.22}$$

The de-aliasing based on the "2/3"-rule can be easily implemented, especially for a parallel code, because it does not require major changes compared to the version without de-aliasing. This is the reason why the "2/3"-rule was used here for the channel flow code, even though it incurs some extra computational cost for carrying

along in the other steps the modes used for de-aliasing.

The influence and possible treatment of aliasing errors in the nodal, polynomial expansion on the GLL points, which is used in wall-normal direction for the channel flow LES, has not been investigated so far to our knowledge. The subject is less clear than in the case of Fourier expansions, because the basis functions (3.15) of the expansion are only approximately orthogonal. Numerical experiments with the viscous Burgers equations seem to indicate, however, that aliasing-like errors can indeed play a significant role in GLL-polynomial expansions, as would be expected because of their spectral-like properties. We propose, therefore, in analogy to the methods for Fourier expansions, a truncation method for aliasing removal in an expansion with basis functions of the form (3.15). It is based on a transformation to a modal expansion. The product is first computed in physical space by multiplying the expansion coefficients/nodal values (of the Lagrange interpolant) at the GLL points: $F_j = U_j V_j$ (no sum), then the final result F^{da} is computed by:

$$F_j^{da} = \sum_{k=0}^{M_z} \left(\frac{1}{\gamma_k} \sum_{n=0}^{N_z} F_n L_k(\xi_n) w_n \right) L_k(\xi_j). \tag{3.23}$$

In tests with the one-dimensional Burgers equation, this method resulted in significant improvements of the results.

The fully de-aliased version of the code (using de-aliasing for both the Fourier- and GLL-expansion) has been applied to the channel flow LES, and results computed with and without de-aliasing will be compared, see Sec. 4.2. The improvements were only small, which may indicate that the use of the skewsymmetric form of the nonlinear term, at least in this particular case, significantly reduces aliasing errors through cancellation effects.[38]

The Helmholtz problem for the diffusion term

The diffusion term in the Navier-Stokes equations makes the solution of a Helmholtz equation necessary, if numerical methods of the types described here are used (i.e., hybrid spatial discretization and/or time splitting using implicit methods for the

diffusion term). In this section, the Galerkin formulation of the Helmholtz problem will first be described in a more general form and then details of the discretized system will be given for the numerical method used in the present work.

We consider the Helmholtz equation:

$$\nabla^2 u - \lambda^2 u = f \tag{3.24}$$

on a domain Ω. (The problem is discussed for a scalar u, which can be a component of the velocity vector. The function f describes the right-hand side of the equation, and λ^2 is a constant.) It is assumed that the boundary of the domain can be decomposed in non-overlapping sections $\partial\Omega_{\mathcal{D}}$, on which Dirichlet boundary conditions are given, and $\partial\Omega_{\mathcal{N}}$ with Neumann boundary conditions. (Note that $\partial\Omega_{\mathcal{N}}$ may be empty. This is in fact the case for the channel flow, but Neumann boundary conditions are naturally included in the formulation, and therefore this term will be retained in the general description of the Helmholtz problem in this section.) All functions are assumed to be sufficiently smooth so that a unique solution exists.

To cast (3.24) in variational form we define the inner product over the domain Ω as:

$$(f, g)_\Omega \equiv \int_\Omega f(\mathbf{x}) g(\mathbf{x})\, d\mathbf{x}. \tag{3.25}$$

We define a test function v which has the property:

$$v(\mathbf{x}) = 0 \text{ on } \partial\Omega_{\mathcal{D}}. \tag{3.26}$$

Taking the inner product of v with (3.24) we obtain:

$$(v, \nabla^2 u)_\Omega - \lambda^2 (v, u)_\Omega = (v, f)_\Omega. \tag{3.27}$$

The first term can be integrated by parts to obtain:

$$(\nabla v, \nabla u)_\Omega + \lambda^2 (v, u)_\Omega = \int_{\partial\Omega_\mathcal{N}} v \nabla u \cdot \hat{\mathbf{n}} \, dS - (v, f)_\Omega. \tag{3.28}$$

The integration in the surface integral is only performed over $\partial\Omega_\mathcal{N}$ because the test function vanishes for $\partial\Omega_\mathcal{D}$.

The Galerkin approximation of the last equation is obtained by replacing the exact solution u and the exact right-hand side f with their finite-dimensional expansions u^δ and f^δ. The test function will be expanded using the same set of basis functions as for u^δ, which is what distinguishes the Galerkin method from other weighted-residual methods. The Galerkin approximation can formally be written as

$$\mathrm{a}(u^\delta, v^\delta)_\Omega = (v^\delta, g_\mathcal{N})_{\partial\Omega_\mathcal{N}} - (v^\delta, f^\delta)_\Omega, \tag{3.29}$$

where we have introduced the operator $\mathrm{a}(f, g)_\Omega \equiv \int_\Omega (\nabla f)(\nabla g) \, d\mathbf{x} + \lambda^2 \int_\Omega fg \, d\mathbf{x}$. The Neumann boundary condition has been written using $g_\mathcal{N} \equiv [\nabla u^\delta \cdot \hat{\mathbf{n}}]\big|_{\delta\Omega_\mathcal{N}}$.

In order to implement the Dirichlet boundary conditions, the approximate solution u^δ is decomposed in a known function $u^\mathcal{D}$, which satisfies the Dirichlet boundary condition, and an unknown, homogeneous function $u^\mathcal{H}$, which vanishes on $\partial\Omega_\mathcal{D}$. Substituting this decomposition, we obtain:

$$\mathrm{a}(u^\mathcal{H}, v^\delta)_\Omega = (v^\delta, g_\mathcal{N})_{\partial\Omega_\mathcal{N}} - (v^\delta, f^\delta)_\Omega - a(u^\mathcal{D}, v^\delta)_\Omega. \tag{3.30}$$

For the numerical method used in the channel flow simulations of the present work, the discretization (3.21) is used. The Fourier modes in the two homogeneous directions are decoupled in the Helmholtz equation. Therefore, a one-dimensional Helmholtz equation (in wall-normal z-direction) is solved independently at each (x, y) location.

We introduce the vector $\check{\mathbf{u}}_{mp}$, which contains Fourier coefficients u_{mpq}, $q = 0, \ldots, N_z$ for fixed modes (m, p), cf. (3.21), but we will drop the indices mp in the following.

In other words, this vector contains the coefficients for the expansion in terms of the basis (3.15) in z-direction. The vector $\check{\mathbf{u}}^{\mathcal{D}}$ contains the coefficients of $u^{\mathcal{D}}$ which is constructed using those basis functions which have non-zero support on the (Dirichlet) boundary. And the vector $\check{\mathbf{u}}^{\mathcal{H}}$ contains the coefficients of the unknown homogeneous solution $u^{\mathcal{H}}$, which vanishes at the boundary. Furthermore, the vector $\check{\mathbf{f}}$ represents the discretization of the right-hand side f, and the vector $\mathbf{\Gamma}$ represents the contribution of the surface integrals in (3.30).

In order to allow a more compact formulation of the discrete system, we define matrix operators. (This description can be extended to a general, three-dimensional expansion, see [30, Chap. 4]). The *weight matrix* $\mathbf{W}$ is defined as:

$$W_{ij} \equiv J_i w_i \delta_{ij} \quad \text{(no sum)}. \tag{3.31}$$

The GLL weights were defined in (3.16) and the GLL points ξ_i in (3.14). The Jacobian $J_i = d\chi/d\xi$ is unity for the special case of the channel flow with walls at $z = -1$ and $z = 1$, cf. (3.21).

The *derivative matrix* $\mathbf{D}$ which, in this case, is only needed for the derivative in wall-normal direction, is given by:

$$D_{ij} \equiv \left.\frac{dh_j(\xi)}{d\xi}\right|_{\xi_i}. \tag{3.32}$$

The integrals are evaluated by Gauss-Lobatto-Legendre quadrature using the $(N_z + 1)$ nodes, and we obtain the discretized system:

$$\mathbf{D}^T\mathbf{W}\mathbf{D}\check{\mathbf{u}}^{\mathcal{H}} + \lambda^2\mathbf{W}\check{\mathbf{u}}^{\mathcal{H}} = -\mathbf{W}\check{\mathbf{f}} + \mathbf{\Gamma} - (\mathbf{D}^T\mathbf{W}\mathbf{D}\check{\mathbf{u}}^{\mathcal{D}} + \lambda^2\mathbf{W}\check{\mathbf{u}}^{\mathcal{D}}) \tag{3.33}$$

3.3.2 Parallelization

Large-eddy simulations of channel flow, despite their strongly reduced computational cost compared to DNS, still require the use of supercomputers. Such high-performance

computers are mostly built as parallel machines at the present time. Therefore, the original, sequential code had to be parallelized as part of the present work.

The version of the channel code used for all simulations in this work decomposes the computational domain in the spanwise direction, i.e., the discretized computational domain is divided in x-z-planes, and a subset of the total number of planes is assigned to each of the parallel processes. If there are N_y spanwise modes/gridpoints total, and there are P parallel processes, the computational domain of each process will be comprised of N_y/P such planes. Therefore, at most N_y processors can be used so that the domain of each processor consists of at least one plane; also, to avoid load imbalances and simplify the implementation of the parallel code, we require that N_y must be divisible by P.

The parallelization is based on the message-passing model, i.e., each process has its own, separate memory, but is able to communicate with the other processes using special subroutines. It is implemented using MPI.[24]

Each process can compute the linear pressure and viscous terms independently on its subdomain. The nonlinear term, however, requires special treatment in the parallel code. Because of the coupling of modes, it is most efficiently evaluated in physical space. But this requires inverse Fourier transformations in streamwise direction (which can be performed locally to each process) and in spanwise direction. The latter require a global transpose of the computational domain, i.e., the data has to be redistributed over the process such that it is now divided up in streamwise direction, and the domain of each process now comprises one or more complete y-z-planes. After the transpose, Fourier transforms in spanwise directions can be performed locally on each process (since all the spanwise modes for a given (x, z) coordinate are now on the same process). After the transform has been performed, the data has to be transposed back to its original distribution. Each transpose of the data requires all-to-all communication of each process with each other process, which is expensive in terms of communication time required, but seems unavoidable in the parallel implementation of spectral methods.

Additional communication is required for the SGS-model implementation: When

the structure function is computed according to (2.46), each process needs to exchange the data at the boundaries of its domain in spanwise direction with its neighboring processes.

3.3.3 Time discretization I

The original code by Chan[9] uses a fractional step method based on the scheme by Kim and Moin.[33] The semi-discrete system of equations for this time-discretization scheme is given by:

$$\frac{\hat{\mathbf{U}} - \mathbf{U}^n}{\Delta t} = \sum_{j=1}^{4} \gamma_j \mathbf{k}_{(j)}, \text{ where } \mathbf{k}_{(j)} = \mathbf{N}(\mathbf{U}^n + \sum_{l=1}^{j-1} \beta_{jl} \mathbf{k}_{(l)}) \text{ and } \mathbf{k}_{(1)} = \mathbf{N}(\mathbf{U}^n), \tag{3.34}$$

$$\frac{\mathbf{U}^* - \hat{\mathbf{U}}}{\Delta t} = \frac{1}{2}\mathbf{L}(\mathbf{U}^* + \mathbf{U}^n), \tag{3.35}$$

$$\frac{\mathbf{U}^{n+1} - \mathbf{U}^*}{\Delta t} = -\nabla \phi^{n+1}. \tag{3.36}$$

In (3.34), the nonlinear term is integrated by a four-step Runge-Kutta scheme. The coefficients are given as: $\beta_{21} = \frac{1}{4}$, $\beta_{31} = 0$, $\beta_{42} = 0$, $\beta_{43} = \frac{1}{2}$, and $\gamma_4 = 1$, $\gamma_3 = \gamma_2 = \gamma_1 = 0$. The integration of the linear term in (3.35) uses the second-order, implicit Crank-Nicholson scheme. The scalar ϕ, which is related to the physical pressure, is determined such that the resulting velocity $\mathbf{U}^{n+1}$ satisfies the divergence-free condition. Taking the divergence of (3.36) and requiring $\nabla \cdot \mathbf{U}^{n+1} = 0$, one obtains:

$$\nabla^2 \phi^{n+1} = \frac{1}{\Delta t} \nabla \cdot \mathbf{U}^*. \tag{3.37}$$

The accuracy of splitting methods in general is strongly influenced by the type of boundary conditions used for the intermediate step. It is well known that inconsistent boundary conditions can introduce time-discretization errors of $O(1)$. Kim and Moin[33] derive an extrapolation boundary condition of second-order accuracy for the

intermediate velocity $\mathbf{U}^*$:

$$\mathbf{U}^* = \mathbf{U}^{n+1} + \Delta t \nabla \phi^n + O(\Delta t^2) \quad \text{on} \quad \partial\Omega_{\mathcal{D}}, \tag{3.38}$$

where $\partial\Omega_{\mathcal{D}}$ are the segments of the domain boundary $\partial\Omega$, for which Dirichlet boundary conditions are specified.

To discuss the boundary conditions for (3.37), we apply the method of weighted residuals to this equation (see Sec. 3.3.1):

$$\int_\Omega W \nabla^2 \phi \, d\mathbf{x} = \frac{1}{\Delta t} \int_\Omega W \nabla \cdot \mathbf{U}^* \, d\mathbf{x} \tag{3.39}$$

$$\Leftrightarrow -\int_\Omega \nabla W \nabla \phi \, d\mathbf{x} + \int_{\partial\Omega} W \frac{\partial \phi}{\partial \hat{\mathbf{n}}} \, dS = -\frac{1}{\Delta t} \int_\Omega \nabla W \cdot \mathbf{U}^* \, d\Omega + \frac{1}{\Delta t} \int_{\partial\Omega} W \mathbf{U}^* \cdot \hat{\mathbf{n}} \, dS \tag{3.40}$$

From (3.36) we obtain: $\partial\phi/\partial\hat{\mathbf{n}} = -(1/\Delta t)(\mathbf{U}^{n+1} - \mathbf{U}^*) \cdot \hat{\mathbf{n}}$. Substituting this and cancelling the $\mathbf{U}^*$ term, leads to the following equation for ϕ:

$$-\int_\Omega \nabla W \nabla \phi \, d\mathbf{x} = -\frac{1}{\Delta t} \int_\Omega \nabla W \cdot \mathbf{U}^* \, d\Omega + \frac{1}{\Delta t} \int_{\partial\Omega} W \mathbf{U}^{n+1} \cdot \hat{\mathbf{n}} \, dS. \tag{3.41}$$

This shows that no additional boundary conditions for the pressure correction ϕ are necessary. (Of course, since computing the pressure correction is a Neumann problem, the arbitrary constant in the solution needs to be set in a suitable way, usually by setting the mean of ϕ in one plane to zero.)

3.3.4 Time discretization II

The original channel code by Chan has been modified in the course of the present work to implement the time-discretization scheme of Karniadakis et al.[29] This technique uses a high-order-accurate pressure boundary condition and a "stiffly-stable" time-integration scheme. These schemes have larger stability regions than standard Adams-type explicit schemes. They are also more efficient than the discretization scheme described in the previous section, which also has good stability properties but uses

a computationally expensive Runge-Kutta method even though the limited overall accuracy still imposes rather strict limits on the timestep.

The splitting method of Ref. 29 takes the form:

$$\frac{1}{\Delta t}\left(\hat{\mathbf{U}} - \sum_{q=0}^{J_i-1} \alpha_q \mathbf{U}^{n-q}\right) = \sum_{q=0}^{J_e-1} \beta_q \mathbf{N}(\mathbf{U}^{n-q}), \tag{3.42}$$

$$\frac{\hat{\hat{\mathbf{U}}} - \hat{\mathbf{U}}}{\Delta t} = -\nabla \bar{p}^{n+1}, \tag{3.43}$$

$$\frac{\gamma_0 \mathbf{U}^{n+1} - \hat{\hat{\mathbf{U}}}}{\Delta t} = \frac{1}{Re}\nabla^2 \mathbf{U}^{n+1}, \tag{3.44}$$

where J_e and J_i are the order of the explicit and implicit time-integration rules, respectively. The values of the coefficients are derived in Ref. 29 for schemes up to third order. For example, the values for the third-order schemes are: $\gamma_0 = 11/6$, $\alpha_0 = 3$, $\alpha_1 = -3/2$, $\alpha_2 = 1/3$, $\beta_0 = 3$, $\beta_1 = -3$, $\beta_2 = 1$.

The pressure correction $\bar{p}^{n+1}$ is again determined by a Poisson equation, which here has the form:

$$\nabla^2 \bar{p}^{n+1} = \frac{1}{\Delta t}\nabla \cdot \hat{\mathbf{U}} \quad \text{in } \Omega \tag{3.45}$$

but a special boundary condition for the pressure correction is required. (The pressure correction is the intermediate step in this splitting scheme.)

Formally, the correct boundary condition can be derived by taking the inner product of the unit normal $\hat{\mathbf{n}}$ with the momentum equation and evaluating the result at the (Dirichlet) boundary to obtain (in semi-discrete form):

$$\frac{\partial \bar{p}^{n+1}}{\partial \hat{\mathbf{n}}} = \hat{\mathbf{n}} \cdot \left[\sum_{q=0}^{J_e-1} \beta_q \mathbf{N}(\mathbf{U}^{n-q}) + \frac{1}{Re}\mathbf{L}(\mathbf{U}^{n+1})\right] \quad \text{on } \partial\Omega. \tag{3.46}$$

This expression for the boundary condition contains terms at time level $(n+1)$, which are unknown. Therefore, an explicit timestepping method must be applied to this boundary condition. Numerical instabilities can be avoided by making use of the vector identity $\nabla^2 \mathbf{U} = \nabla(\nabla \cdot \mathbf{U}) - \nabla \times (\nabla \times \mathbf{U})$, see Ref. 29. The irrotational

part is formally treated implicitly, but consistent with the derivation of the pressure Poisson equation, the divergence at timestep $(n+1)$ is set to zero. Therefore, only the solenoidal part remains, which is integrated by the same explicit scheme as the nonlinear term. This leads to the following final form of the high-order pressure boundary condition:

$$\frac{\partial \bar{p}^{n+1}}{\partial \hat{\mathbf{n}}} = \sum_{q=0}^{J_e-1} \beta_q \hat{\mathbf{n}} \cdot \left[-\frac{1}{Re} \nabla \times (\nabla \times \mathbf{U})^{n-q} + \mathbf{N}(\mathbf{U}^{n-q}) \right] \quad \text{on } \partial\Omega. \tag{3.47}$$

3.3.5 A test case for numerical channel flow simulations: linear growth of small disturbance

The initial conditions for this test case are obtained using eigenfunctions of the Orr-Sommerfeld stability equation. We write the perturbation velocity in general as $\mathbf{u}'(\mathbf{x},t) = \breve{\mathbf{u}}(z)\exp[i(\alpha x + \beta y - \alpha c t)]$, but it can be shown that the problem can be reduced to an equivalent two-dimensional problem. We then introduce the streamfunction of the perturbation $\psi' = \phi(z)\exp[i\alpha(x-ct)]$, and obtain in the end the following eigenproblem for ϕ, the well-known Orr-Sommerfeld equation (for detailed derivation, see 17):

$$\frac{1}{i\alpha\, Re}\left(\frac{\partial^2}{\partial z^2} - \alpha^2\right)^2 \phi = (U-c)\left(\frac{\partial^2}{\partial z^2} - \alpha^2\right)\phi - U''\phi, \tag{3.48}$$

where $U = U(z)$ is the mean velocity profile. The boundary conditions for rigid walls at $z=-1$ and $z=1$ are: $\alpha\phi = \partial\phi/\partial z = 0$.

To test Navier-Stokes solvers in the channel flow geometry, one can numerically solve the eigenproblem, and use, for example, one unstable mode as a small-amplitude perturbation superimposed on the parabolic profile of the laminar channel flow. When the evolution of such an initial flowfield is simulated with the Navier-Stokes code, the simulation result for the growth of the perturbation (as measured, e.g., by the growth of the perturbation energy) can be compared to the result obtained from linear theory, as long as the amplitude of the perturbation is small enough.

Discrete formulation of the eigenproblem

The present formulation uses the basis functions (3.15), even though other, very efficient formulations are known, e.g. Ref. 64. But the eigenfunctions obtained with the present formulation can be used directly to generate initial conditions for our channel flow code, which uses the same basis functions.

To reduce the order of the problem, we introduce $\zeta \equiv \partial\phi/\partial z$, and obtain a system of equations:

$$\frac{\partial^3\zeta}{\partial z^3} - 2\alpha^2\frac{\partial\zeta}{\partial z} + \alpha^4\phi - i\alpha\, Re\, U\left(\frac{\partial\zeta}{\partial z} - \alpha^2\phi\right) + i\alpha\, Re\, U''\phi = -c\, i\alpha\, Re\left(\frac{\partial\zeta}{\partial z} - \alpha^2\phi\right) \tag{3.49}$$

$$\frac{\partial\phi}{\partial z} - \zeta = 0. \tag{3.50}$$

We use the matrix operators $\mathbf{W}$ and $\mathbf{D}$ introduced above, see (3.31) and (3.32), and the operator for the second derivative:

$$D^{(2)}_{ij} \equiv \left.\frac{d^2 h_j(\xi)}{d\xi^2}\right|_{\xi_i}. \tag{3.51}$$

Moreover, we denote by $\boldsymbol{\zeta}$ and $\boldsymbol{\phi}$ the vectors of the nodal values of ζ and ϕ, respectively. And the vectors $\mathbf{U}$ and $\mathbf{U}''$ contain the values of the mean profile and of its curvature at the nodes. Then the discrete system can be written in the form:

$$\begin{aligned} -\mathbf{D}^T\mathbf{W}\mathbf{D}^{(2)}\boldsymbol{\zeta} - 2\alpha^2\mathbf{W}\mathbf{D}\boldsymbol{\zeta} - i\alpha\, Re\,\mathbf{U}^T\mathbf{W}\mathbf{D}\boldsymbol{\zeta} \\ +\alpha^4\mathbf{W}\boldsymbol{\phi} + i\alpha\, Re(\alpha^2\mathbf{U}^T + \mathbf{U}''^T)\mathbf{W}\boldsymbol{\phi} = -c\, i\alpha\, Re(\mathbf{W}\mathbf{D}\boldsymbol{\zeta} - \alpha^2\mathbf{W}\boldsymbol{\phi}) \end{aligned} \tag{3.52}$$

$$\mathbf{W}\mathbf{D}\boldsymbol{\phi} - \mathbf{W}\boldsymbol{\zeta} = 0 \tag{3.53}$$

Defining the solution vector $\mathbf{x} = [\boldsymbol{\zeta}^T, \boldsymbol{\phi}^T]^T$, the system can be written in the standard form of a generalized eigenproblem: $\mathbf{A}\mathbf{x} = c\mathbf{B}\mathbf{x}$. This problem can be solved numerically using a LAPACK routine.

Initial condition for test case

The chosen parameters have been frequently used to test numerical methods for channel flow, see, e.g., Ref. 40. The eigenproblem for the Orr-Sommerfeld equation is solved for $\alpha = 1$ and $Re_c = 7500$, where Re_c is the Reynolds number based on the centerline velocity and channel halfwidth. There is one unstable mode, the value of which is given as $c \equiv c_R + ic_I = 0.24989154 + i0.00223498$ in Ref. 51. With the numerical scheme described in the previous section, the computed value of this eigenvalue is $c_{65} = 0.24989148 + i0.00223441$ for $N_z = 65$ and $c_{97} = 0.24989154 + i0.00223498$ for $N_z = 97$.

The corresponding eigenfunction is used to generate a perturbation velocity field $(u', 0, w')$ which is superimposed on the laminar channel flow to obtain an initial velocity field (U, V, W) of the form:

$$U = 1 - z^2 + \epsilon u' \tag{3.54}$$

$$V = 0 \tag{3.55}$$

$$W = \epsilon w' \tag{3.56}$$

where ϵ is an amplitude parameter. For the present case $\epsilon = 10^{-4}$ is used.

Results from the test case

From this initial condition, the Navier-Stokes equations are integrated forward in time with the channel flow code, and the growth of the perturbation energy:

$$E'(t) = \int_{x=0}^{L_x} \int_{z=-h}^{h} (u'^2 + w'^2)\, dx\, dz \tag{3.57}$$

is measured (h is the channel halfwidth and L_x is the domain length in streamwise direction). In this test only, the simulations are non-dimensionalized using the centerline velocity and the channel halfwidth as scaling parameters. The integration time $t_{\text{end}} - t_{\text{start}} = 50$ corresponds to twice the time required by the disturbance to propagate through the computational domain: This propagation time T can be obtained

from the phase speed (as obtained from linear theory) c_R/α as $T = L_x\alpha/c_R \approx 25$. We plot the growth of perturbation energy normalized by E'_0, the perturbation energy in the initial condition. The exact solution according to linear theory, $E'(t)/E'_0 = e^{2c_I t}$, is shown in the figures for comparison.

All the results shown here are computed with $N_z = 65$. The number of Fourier modes in the homogeneous directions were $N_x = 16$ and $N_y = 4$, but the resolution in the x and y-direction has little influence on the present tests. Results with higher wall-normal resolution (not shown) are closer to the exact solution, but the size of the timestep has been found to have a much stronger influence on the quality of the results. In Fig. 3.1, a comparison between the original time-discretization scheme I (see Sec. 3.3.3) and the new scheme II implemented in the course of the present work (Sec. 3.3.4) can be made: The solution of scheme II ($\Delta t = 5 \cdot 10^{-5}$) is closer to the theoretical solution than the one computed with scheme I ($\Delta t = 10^{-5}$), even though the former is computed with a five times larger timestep. Since scheme II also requires only about a third of the CPU time for one timestep compared to scheme I, the total CPU time for the test with scheme II was about 15 times less than the time required for scheme I. Both of the numerical solutions, however, are not converged completely,

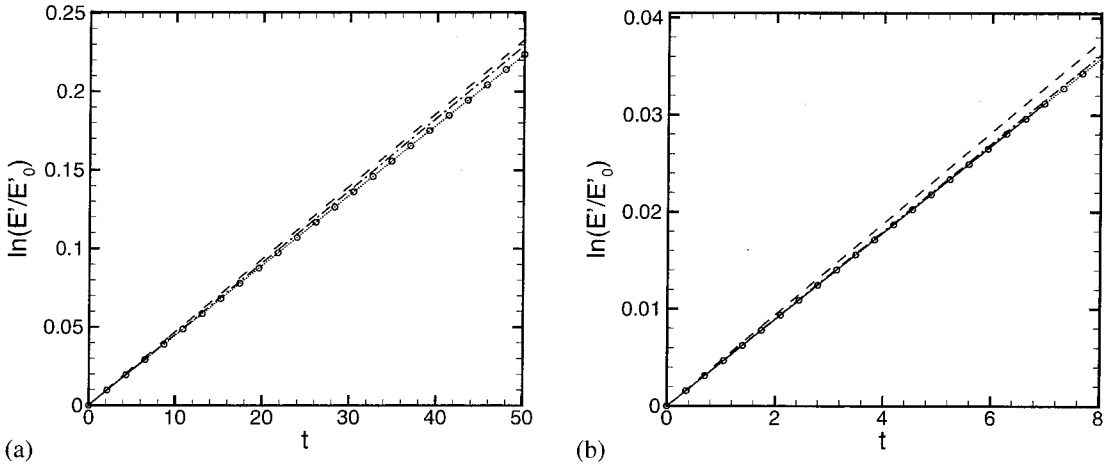

Figure 3.1: Growth of perturbation energy for a small normal-mode perturbation in a channel, (a) complete runs and (b) enlarged for early times. - - -: time discretization I with $\Delta t = 10^{-5}$, - · -: time discretization II with $\Delta t = 5 \cdot 10^{-5}$, —— : time discretization II with $\Delta t = 0.5 \cdot 10^{-5}$, o · · · o: linear theory.

yet. To indicate that the accuracy of the solution can be improved by reducing the timestep, results for a shorter runtime are shown using time discretization II and a timestep of $\Delta t = 0.5 \cdot 10^{-5}$. This computation (which inevitably is quite slow) has not been carried out for the whole 50 time units, but an enlargement for the shorter timespan in Fig. 3.1b seems to indicate that good convergence can be achieved if the timestep is small enough.

3.3.6 Divergence errors

Non-zero divergence in the numerical solution for the resolved-scale velocity field can be a problem in simulations of incompressible, wall-bounded flows. This is at least in part due to the use of splitting methods for the time discretization. They are widely used because they are computationally efficient and applicable to very general flow conditions, but it is also well known that the splitting methods inevitably lead to divergence errors. These errors normally manifest themselves in a layer of non-zero divergence at the boundary. By using high-order-accurate boundary conditions, the influence of these errors on the global solution can, however, be reduced so that the errors are of higher order than the error of the time discretization itself.[29]

Divergence errors in the solution are a particular source of concern in connection with the stretched-vortex model. The influence of divergence errors on the model manifests itself in their effect on the subgrid kinetic energy production term $\varepsilon_{\text{sgs}} = -\tilde{S}_{ij}\tau_{ij}$, cf. (2.26). If this quantity is evaluated in the vortex-fixed frame (cf. Sec. 2.2.1) and if for reasons of simplicity we assume alignment with $\tilde{\mathbf{e}}_3$ only (cf. Sec. 2.3.4), we obtain:

$$\varepsilon_{\text{sgs}} = -K(\lambda_1 + \lambda_2), \tag{3.58}$$

where, as defined before, K is the subgrid kinetic energy and $\lambda_1 < \lambda_2 < \lambda_3$ are the eigenvalues of $\tilde{S}_{ij}$. For this alignment model, the vortex-fixed coordinate axes are identical to the principal axes of $\tilde{S}_{ij}$. If the solution was exactly solenoidal, we would have $\lambda_1 + \lambda_2 + \lambda_3 = 0$, and therefore $\lambda_3 > 0$ and $\lambda_1 + \lambda_2 < 0$. This ensures

$\varepsilon_{sgs} > 0$, which means, with the sign conventions used in (2.26), that the model is purely dissipative, i.e., energy is always transferred from the resolved scales to the subgrid model. If the divergence-free condition is not exactly satisfied, and the errors become large, the case $\lambda_1 + \lambda_2 > 0$ could occur, creating an inverse energy transfer which is not consistent with the physical model for this choice of alignment, and which could also cause numerical instabilities.

For the channel code used in the present work, the divergence error is shown in Fig. 3.2, where we plot the instantaneous plane averages of the normalized divergence error of velocity fields obtained from LES with and without de-aliasing, and with the two different time-discretization schemes. (The plane average is, of course, taken over the absolute value of the error, not the signed value.) The normalized divergence error is given by:

$$\frac{|\nabla \cdot \tilde{\mathbf{U}}|}{\sqrt{\lambda_1^2 + \lambda_2^2 + \lambda_3^2}}. \tag{3.59}$$

The normalization factor can be expressed in terms of the invariants of the resolved rate-of-strain tensor: $\lambda_1^2 + \lambda_2^2 + \lambda_3^2 = I_3^2 - 2I_2$, where $I_3 \equiv \mathrm{tr}(\tilde{\mathbf{S}})$ and $I_2 \equiv \frac{1}{2}[\mathrm{tr}(\tilde{\mathbf{S}})^2 - \mathrm{tr}(\tilde{\mathbf{S}}^2)]$.

It may seem surprising that the divergence error in the interior of the channel is higher for the version with time-discretization scheme II, which uses a high-order boundary condition. But this is actually expected, since in time-discretization scheme I the pressure step, which serves to enforce the divergence-free condition, is performed last, while in scheme II the viscous step is performed last, which may introduce small additional errors. The trade-off for performing the pressure step last in scheme I is that there would be small errors in enforcing the no-slip boundary conditions. Results which clearly indicated the positive influence of the high-order boundary condition of scheme II were already presented in the previous section. The purpose of Fig. 3.2 is to give an indication of the actual divergence errors present in the large-eddy simulations for which results will be shown below. The divergence errors in Fig. 3.2 are small enough in the channel interior so that no negative influ-

ence on the model performance is to be expected. The larger values very close to the boundary seem to be unavoidable with splitting methods. Since the model contribution goes to zero as the boundary is approached (see Sec. 4.2.6), these boundary errors are not expected to have a significant influence on the LES.

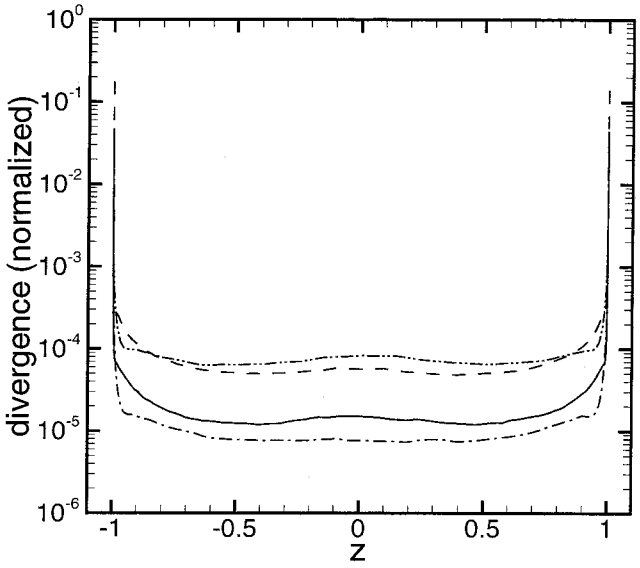

Figure 3.2: Normalized divergence error (instantaneous, plane-averaged) of channel flow LES, - - -: $Re_\tau = 1017$, no de-aliasing, scheme I; —— : $Re_\tau = 1017$, with de-aliasing, scheme I; - · -: $Re_\tau = 180$, with de-aliasing, scheme I; -·-·-: $Re_\tau = 180$, with de-aliasing, scheme II.

3.3.7 Simulations with constant mean pressure gradient

The external forcing necessary to drive the channel flow can be realized as a constant mean pressure gradient. To determine the value of the mean pressure gradient needed to drive the flow, we employ the Reynolds-averaged momentum equations. Since all derivatives of mean quantities in the spanwise and streamwise directions (except for the mean pressure gradient) are assumed to be zero, the non-dimensional momentum equations in steady channel flow for the streamwise and wall-normal direction reduce

to:

$$0 = -\frac{\partial \overline{\overline{P}}}{\partial x} - \frac{d}{dz}\overline{\overline{u'w'}} + \frac{1}{Re_\tau}\frac{d^2\overline{\overline{U}}}{dz^2} \tag{3.60}$$

$$0 = -\frac{\partial \overline{\overline{P}}}{\partial z} - \frac{d}{dz}\overline{\overline{w'^2}}. \tag{3.61}$$

The coordinate system we use for the channel flow is defined as follows: the streamwise direction is the x-direction, spanwise is y, and wall-normal is z. Periodic boundary conditions are used in the streamwise and spanwise directions (see Sec. 3.3). The governing equations for the channel flow simulation are non-dimensionalized based on the wall-shear velocity $u_\tau \equiv (\tau_W/\rho)^{1/2}$ and the channel halfwidth h. Here, τ_W is the shear stress at the wall, ρ is the density, and ν is the kinematic viscosity. The Reynolds number is then defined as $Re_\tau = u_\tau h/\nu$.

The wall-normal momentum equation (3.61) can be integrated with respect to z to yield: $\overline{\overline{P}} + \overline{\overline{w'^2}} = \overline{\overline{P}}_0$, where $\overline{\overline{P}}_0$ does not depend on z. Since $\overline{\overline{w'^2}}$ is independent of x, this equation implies that $\partial\overline{\overline{P}}/\partial x$ is equal to $d\overline{\overline{P}}_0/dx$. Substituting this in the streamwise momentum equation, it can be integrated with $z = -1$ (lower wall) as lower limit of integration:

$$0 = -(z+1)\frac{d\overline{\overline{P}}_0}{dx} - \overline{\overline{u'w'}} + \frac{1}{Re_\tau}\frac{d\overline{\overline{U}}}{dz} - \frac{1}{Re_\tau}\frac{d\overline{\overline{U}}}{dz}\bigg|_{z=-1}. \tag{3.62}$$

From the definition of u_τ, we have (after non-dimensionalization): $d\overline{\overline{U}}/dz\big|_{z=-1} = Re_\tau$. Furthermore, at the channel center (z=0), the total shear stress $(-\overline{\overline{u'w'}} + (1/Re_\tau)d\overline{\overline{U}}/dz)$ must be zero for reasons of symmetry. Evaluating (3.62) at $z = 0$, yields the mean pressure gradient required to drive the flow:

$$\frac{d\overline{\overline{P}}_0}{dx} = -1. \tag{3.63}$$

3.3.8 Simulations with constant flowrate

Instead of imposing a constant mean pressure gradient, the channel flow can also be driven by imposing a pressure gradient which is constant in space throughout the domain but varies with time such that the (volume) flowrate through the channel remains constant in time. To describe this method in some more detail, we define the *bulk mean velocity*:

$$U_m(t) = \frac{1}{2}\int_{-1}^{1} \lfloor U \rfloor \, dz, \tag{3.64}$$

where again all quantities are to be understood as non-dimensionalized using u_τ as velocity scale and the channel halfwidth h as length scale. With $\lfloor U \rfloor$ we denote the instantaneous, plane-averaged velocity $\lfloor U \rfloor = 1/(L_x L_y)\int_0^{L_x}\int_0^{L_y} U \, dx \, dy$. U_m is directly proportional to the flowrate.

We now use the streamwise momentum equation and perform spatial averaging in all three directions in order to obtain an equation for U_m:

$$\begin{aligned}
\frac{dU_m}{dt} &+ \frac{1}{2}\frac{1}{L_x}\frac{1}{L_y}\int_{x=0}^{L_x}\int_{y=0}^{L_y}\int_{z=-1}^{1}\left(\frac{\partial U^2}{\partial x} + \frac{\partial (UV)}{\partial y} + \frac{\partial (UW)}{\partial z}\right) dx\, dy\, dz \\
&= \frac{1}{2}\frac{1}{L_x}\frac{1}{L_y}\int_{x=0}^{L_x}\int_{y=0}^{L_y}\int_{z=-1}^{1}\left(-\frac{\partial P}{\partial x}\right) dx\, dy\, dz \\
&+ \frac{1}{Re_\tau}\frac{1}{2}\frac{1}{L_x}\frac{1}{L_y}\int_{x=0}^{L_x}\int_{y=0}^{L_y}\int_{z=-1}^{1}\left(\frac{\partial^2 U}{\partial x^2} + \frac{\partial^2 V}{\partial y^2} + \frac{\partial^2 W}{\partial z^2}\right) dx\, dy\, dz.
\end{aligned} \tag{3.65}$$

This equation can be simplified by carrying out the integration and making use of the boundary conditions for the channel flow. This yields:

$$\frac{dU_m}{dt} = \frac{1}{2}\frac{1}{L_x}\frac{1}{L_y}\int_{x=0}^{L_x}\int_{y=0}^{L_y}\int_{z=-1}^{1}\left(-\frac{\partial P}{\partial x}\right) dx\, dy\, dz + \frac{1}{2Re_\tau}\left(\left\lfloor\frac{\partial U}{\partial z}\right\rfloor_{z=1} - \left\lfloor\frac{\partial U}{\partial z}\right\rfloor_{z=-1}\right), \tag{3.66}$$

where the square half-brackets again denote plane averaging. This equation can be further simplified by decomposing the pressure in a plane-averaged component, the forcing term, and a fluctuating component such that $\partial P/\partial x = -f_x(t) + \partial p'/\partial x$.

The fluctuating component and its derivative will be periodic in streamwise and spanwise direction like the velocity field, and therefore this contribution will vanish after averaging. We therefore obtain the result:

$$\frac{dU_m}{dt} = f_x + \frac{1}{2Re_\tau}\left(\left\lfloor\frac{\partial U}{\partial z}\right\rfloor_{z=1} - \left\lfloor\frac{\partial U}{\partial z}\right\rfloor_{z=-1}\right). \tag{3.67}$$

From this, it is clear that a constant flowrate ($dU_m/dt = 0$) can be achieved by adjusting the (time-dependent) forcing function f_x such that at each instant of time it balances the instantaneous, space-averaged shear stresses at the walls.

Chapter 4 Large-eddy simulations with the stretched-vortex model

4.1 Decaying isotropic turbulence

Isotropic turbulence has long been a topic of great interest to theoretical turbulence research (see, e.g., Batchelor[5]). This is mainly due to the great simplifications which result from the constraints imposed by the condition of isotropy in the statistical description of turbulence. Isotropic turbulence can also be simulated very efficiently by numerical methods (cf. Sec. 3.1). The first attempt of direct numerical simulation of three-dimensional turbulence was a simulation of decaying isotropic turbulence, which was simulated in a periodic box.[65] Even though computers are now much more powerful, the DNS of isotropic turbulence has still been of interest in more recent years because in such DNS higher Reynolds numbers can be reached than in simulations of other, more-complicated flows.

The concept of decaying isotropic turbulence, i.e., an infinite space of turbulent motion, decaying in time in the absence of production of turbulence kinetic energy, and its computational approximation by a periodic box containing the turbulence, are, of course, very idealized. But the streamwise evolution of temporally stationary turbulence, generated, for example, by the flow through a grid in a duct, has been found to resemble the time evolution of ideal, isotropic turbulence. Comparison of measurements of stationary grid turbulence, which is inhomogeneous in streamwise direction, with the non-stationary, homogeneous box turbulence is performed by identifying the spatial inhomogeneity of statistical properties (such as kinetic energy) in the experiment with the temporal decay of the same quantity in the box turbulence.[12] The time t in the simulation is then related to the downstream distance from the grid

in the experiment through the Taylor approximation:

$$t \sim \int_0^x \frac{dx'}{\overline{\overline{U}}(x')}, \tag{4.1}$$

where $\overline{\overline{U}}(x)$ is the mean velocity in the experiment. This approximation is applicable as long as the fluctuating component of the velocity is small compared to the mean flow: $u_1'/\overline{\overline{U}} \ll 1$.

The availability of well-documented experimental[12] and DNS[1] data, together with the theoretical interest in this case, has made decaying isotropic turbulence an important testcase for subgrid-stress models in large-eddy simulations. The LES of decaying isotropic turbulence has to reproduce the decay of the turbulence kinetic energy correctly, and energy spectra can be compared to the spectra which Comte-Bellot and Corrsin[12] obtained from their measurements. Since LES for this case can be performed without large computational effort, it is a useful first test for new models. It certainly must be complemented by other tests of shear flows with turbulence energy production, but unlike standard testcases for shear flows, like channel flow, decaying isotropic turbulence is non-stationary.

The numerical methods used for the present simulations have been reviewed in Secs. 3.1 and 3.2. The results of the simulation are compared to the experimental data of Ref. 12. For the computations, a cubic box with sidelength $L = 11M_g$ was used, where $M_g = 5.08\,\mathrm{m}$ is the mesh width used in the experiment. They were performed with non-dimensional variables, using the velocity scale $U_{\mathrm{ref}} = \sqrt{3u_0'^2/2}$ based on the streamwise rms velocity of the experiment $\sqrt{u_0'} = 0.222\,\mathrm{m/s}$, the length scale $L_{\mathrm{ref}} = L/(2\pi)$, and the corresponding time scale $t_{\mathrm{ref}} = L_{\mathrm{ref}}/U_{\mathrm{ref}}$. The experimental results are given using the non-dimensional time $U_\infty t/M_g$, where $U_\infty = 10\,\mathrm{m/s}$ was the freestream air speed in the wind tunnel, and the simulation results have been converted to this time scale, too.

The initial conditions of the simulation are generated by creating a divergence-free velocity field such that the spectrum of this initial field matches the spectrum of the experiment at $U_\infty t/M_g = 42$ for wavenumbers $k < k_c$ (k_c is the cutoff wavenumber).

Matching the spectra does not determine the phases of the Fourier coefficients, which are therefore initially set to be randomly distributed in the interval $[0, 2\pi]$. This leads to some initial transients in the simulation until the flowfield has developed a more realistic structure. These transients may be responsible for the larger discrepancies visible at early times in some of the results shown below.

The tests for decaying isotropic turbulence were not only used as a first indication of whether the SGS model is able to perform successfully in actual LES, but also to investigate the influence of different choices for the alignment of the model subgrid-vortex structures and for the cutoff in the subgrid energy spectrum (see Sec. 2.3.4).

4.1.1 Results obtained with the pseudospectral Fourier code

All simulations with this code (see Sec. 3.1) were performed using a resolution of 32^3 Fourier modes. The decay of the kinetic energy (per unit mass) is shown in Fig. 4.1. The resolved-scale contribution of the energy is computed directly from the resolved-scale velocity field and is shown in Fig. 4.1a. For comparison, the energy spectra given in Ref. 12 are truncated to the resolution of the simulation, so that the experimental data can be decomposed in resolved-scale and subgrid-scale energy. The filtered experimental data for the resolved scales are shown as symbols in Fig. 4.1a. From the SGS model, we also obtain an estimate for the kinetic energy contained in the subgrid scales. This is added to the resolved-scale energy to obtain an estimate for the total kinetic energy, which can be compared directly to the unfiltered experimental data, see Fig. 4.1b.

The comparison of the energy decay shows that the $\tilde{\mathbf{e}}_2 + \tilde{\mathbf{e}}_3$ model is slightly less dissipative than the $\tilde{\mathbf{e}}_3$ model, which can be explained by the fact that the eigenvector $\tilde{\mathbf{e}}_3$ corresponds to the direction of maximum stretch. It can also be seen that the $J = 1$ version is less dissipative than the $J \to \infty$ version. The results for the decay of the total energy are somewhat too low, especially at the early stages of the simulation (possibly due to the initial conditions used, see above). But these results include a model estimate for the subgrid kinetic energy and therefore somewhat larger

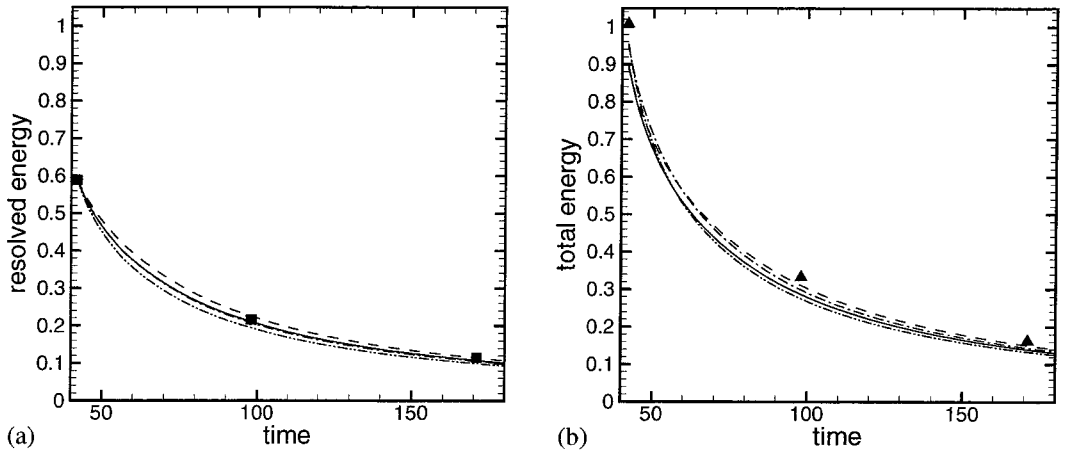

Figure 4.1: Decay of (a) resolved-scale and (b) total kinetic energy, Fourier-Galerkin code, - - -: $\tilde{\mathbf{e}}_2 + \tilde{\mathbf{e}}_3$ model with $J = 1$; ——: $\tilde{\mathbf{e}}_3$ with $J = 1$; - · -: $\tilde{\mathbf{e}}_2 + \tilde{\mathbf{e}}_3$ with $J \to \infty$; -·· -·-: $\tilde{\mathbf{e}}_3$ with $J \to \infty$; symbols: data of Comte-Bellot and Corrsin,[12] filtered for (a).

differences with the experimental results may be expected. It should also be noted that SGS models which only generate the trace-free part of the SGS tensor are not able to estimate the total energy without additional modeling for the subgrid kinetic energy.

The shell-summed, three-dimensional energy spectra, including the modeled subgrid spectra, are shown in Fig. 4.2. The model estimate of the factor $\mathcal{K}_0\epsilon^{2/3}$ determines the vertical offset in the subgrid spectrum. The estimate approximately satisfies the requirement that the spectrum be continuous across the cutoff, even though this condition is not enforced explicitly in the physical-space version of the model.

The results for the resolved-scale spectrum show some differences depending on the choice of J. The results for the $\tilde{\mathbf{e}}_2 + \tilde{\mathbf{e}}_3$ model with $J = 1$ show quite good agreement with the experimental data, while the spectra for the $J \to \infty$ version exhibit a larger energy removal from modes at the highest resolved wavenumbers. This is consistent with the model derivation since the $J \to \infty$ version places slightly more kinetic energy in the subgrid fluctuations because of the $k^{-5/3}$ tail which extends to infinity. This leads to larger subgrid Reynolds stresses which in turn result in larger energy removal from the resolved scales. This difference between the $J \to \infty$ version and the $J = 1$ version is also distinguishable in the decay of the kinetic energy, Fig. 4.1,

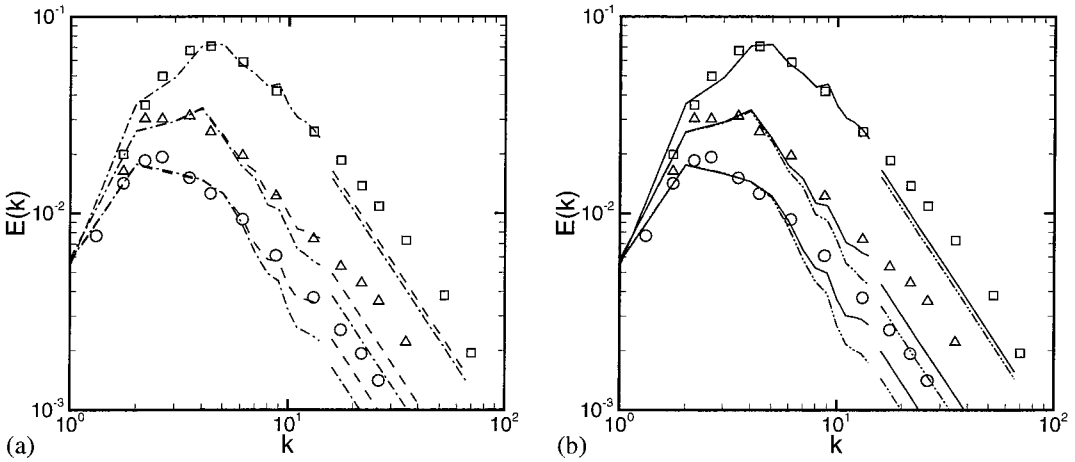

Figure 4.2: Energy spectra for initial and two subsequent times (including the modeled subgrid spectra), (a) $\tilde{\mathbf{e}}_2 + \tilde{\mathbf{e}}_3$ model, - - -: $J = 1$; - · -: $J \to \infty$; (b) $\tilde{\mathbf{e}}_3$ model, —— : $J = 1$; -· ·-: $J \to \infty$; symbols: data from Ref. 12.

but there it has a much smaller influence since it only affects the highest resolved wavenumbers. The results also show that the model is only weakly dependent on the choice of alignment for the subgrid-vortex structure ($\tilde{\mathbf{e}}_2 + \tilde{\mathbf{e}}_3$ model versus $\tilde{\mathbf{e}}_3$ model).

4.1.2 Results obtained with the compact finite-difference code

The resolution for the simulations with this code (see Sec. 3.2) was 32^3 gridpoints. The results for the decay of the kinetic energy, Fig. 4.3, show that the model also performs well within a pure physical-space numerical method. The results for the decay of the resolved-scale energy are of comparable quality as those obtained with the spectral method. The total kinetic energy also shows similar trends: The model estimate for the subgrid kinetic energy is somewhat too low, especially for early times. But this simulation was also able to give a satisfactory estimate for the decay of the total kinetic energy. Energy spectra (Fig. 4.4) are of satisfactory quality, too, taking into account that compact finite-difference methods inevitably have inferior resolution characteristics compared to a Fourier method. Moreover, for the compact finite-difference method, the spectra have to be computed by an additional postprocessing step.

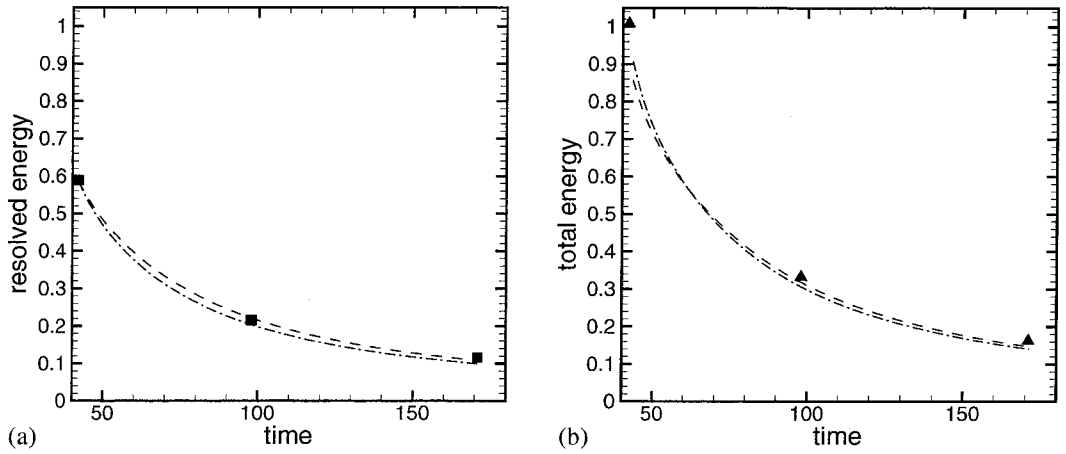

Figure 4.3: Decay of (a) resolved-scale and (b) total kinetic energy, compact finite-difference code, - - -: $\tilde{\mathbf{e}}_2 + \tilde{\mathbf{e}}_3$ model with $J = 1$; - · -: $\tilde{\mathbf{e}}_2 + \tilde{\mathbf{e}}_3$ model with $J \to \infty$.

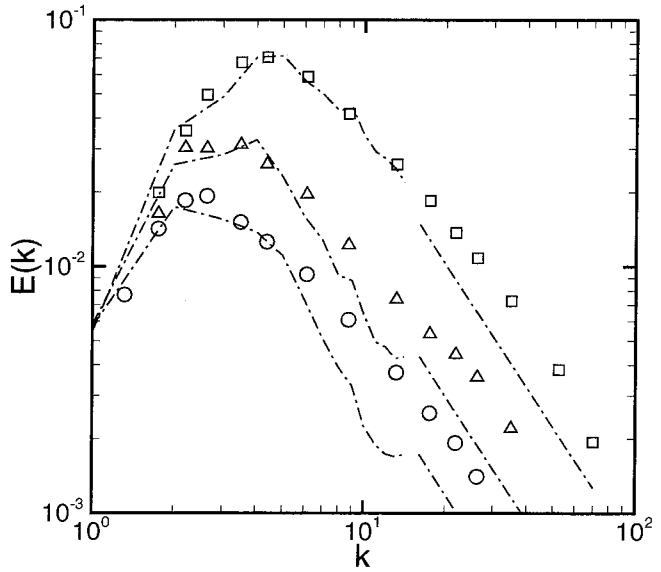

Figure 4.4: Energy spectra, compact finite-difference code, $\tilde{\mathbf{e}}_2 + \tilde{\mathbf{e}}_3$ model with $J \to \infty$.

4.2 Channel flow

Wall-bounded shear flows have been the subject of many theoretical, experimental and computational studies, and even the simplest cases of such flows, i.e., boundary layers, channel flows and pipe flows are still a topic of current research. Channel flow in particular has become a preferred testcase for large-eddy simulation because this case can be more easily simulated with highly-accurate numerical methods and the use of periodic boundary conditions. Boundary layers, for example, are more difficult to compute because of their spatial development (which is sometimes represented as a temporal development in numerical simulations, see review in Ref. 60). Pipe flow, on the other hand, has the disadvantage of the presence of a coordinate singularity, and possibly requires very long streamwise domains because the typical length of flow structures seems to be larger in pipe flow than in channel flow. For these reasons, and to allow a comparison with the performance of other SGS models, we will also use channel flow as a testcase, and will not discuss the other cases in the following.

A classical theory for turbulent channel flow is the logarithmic "law of the wall." It is derived (see, e.g., Ref. 82) by performing an asymptotic matching between the scaling which governs the flow near the center (with the channel halfwidth as length scale) and the scaling in the viscous sublayer close to the wall (where a length scale based on viscosity is relevant). This matching can be performed if one assumes that there exists an inertial sublayer, where the viscous length scale is too small to govern the dynamics of the flow, and the channel halfwidth is too large to be of relevance either. In the absence of an external length scale, the distance from the wall itself is then the only length scale in the inertial sublayer. The result of this matching is that the velocity profile in the inertial sublayer must have the form:

$$U = \frac{1}{\kappa} \ln z + \text{const.} \tag{4.2}$$

where κ, the so-called "von Kármán constant," is accepted as a universal constant (this non-dimensional equation holds regardless whether viscous scaling or outer scal-

ing is used). The existence of a logarithmic region is thus a direct consequence of the assumption that there is an overlap region of simultaneous validity of the viscous scaling and the scaling of the core region.[55] The description of the mean velocity profile in turbulent boundary layers has been completed by Coles,[10] who summarized the developments on the law of the wall and extended it by the "law of the wake," which describes the difference between the actual velocity profile in the core region and the logarithmic law.

Even though the assumption of an inertial sublayer with a logarithmic mean profile is widely used, it is not universally accepted. For example, Barenblatt and Chorin[4] arrive at a power-law profile by arguing that a dependence on the viscosity ν must be retained in the overlap region. The presence of a logarithmic inertial sublayer is difficult to verify (or exclude) with certainty. Logarithmic or power-law dependence are hard to distinguish in plots of experimentally or numerically obtained profiles. Moreover a logarithmic inertial sublayer can only be expected to be present at sufficiently high Reynolds numbers.

Some of the experimental studies of turbulent channel flow are reviewed in Ref. 1. Representative for the many studies which relied on hot-wire and/or hot-film probes to study the channel flow, we mention only the study by Comte-Bellot, who obtained measurements in channel flow in the Reynolds number range of 57 000 to 230 000 (the Reynolds number is based on bulk velocity and channel halfwidth). But at such high Reynolds numbers, the finite length of the probe can become large compared to the length scales of the flow (Wei and Willmarth[86] estimate that Comte-Bellot's probe length was as large as 36 viscous lengths for the highest Reynolds number case). This will cause measurement results to underestimate the magnitude of the turbulence fluctuations. More recently, advancements in measurement technology, which were not available to those earlier investigations, have allowed progress towards more accurate measurements of channel-flow statistics. Wei and Willmarth[86] used a high-resolution, two-component laser-Doppler anemometer to obtain simultaneous measurements of the streamwise and wall-normal turbulent velocity components for bulk Reynolds numbers in the range of 13 000 to 35 000. But even they found in the analysis of their

data indications that the resolution very close to the wall was not completely adequate for their highest Reynolds number cases. For example, they computed the Reynolds shear stress by two different methods, first directly from the velocity traces, and secondly from the momentum balance (using their measured values for the pressure gradient) and found that the results obtained with the two methods were significantly different close to the wall for their highest Reynolds number cases. We will only use the results for their second-highest Reynolds number for comparison with our LES, which is the best available data for moderately high Reynolds numbers. In the results for the root-mean-square velocity fluctuations and other statistics, they found a clear Reynolds number dependence, i.e., the rms velocities at different Reynolds numbers plotted using the viscous scales u_τ and ν/u_τ did not collapse even close to the wall.

Providing accurate data at high Reynolds numbers is even more difficult in numerical simulations. Some of the earliest numerical simulations of turbulence were performed for channel flow (by Deardorff and by Schumann, see the review by Rogallo and Moin[74] for details), but these simulations did not attempt to resolve the near-wall turbulence. Rather, they used artificial boundary conditions in the inertial sublayer, thereby avoiding explicit calculation of the wall region. A first large-eddy simulation of turbulent channel flow (including the wall region) was performed by Moin and Kim[59] for a Reynolds number of 13 800, based on centerline velocity and channel halfwidth. (Unfortunately, computational and experimental studies have different preferences for the definition of the Reynolds number, but the Reynolds number based on centerline velocity and that based on bulk velocity are comparable in magnitude for turbulent channel flow.) The LES of Moin and Kim used a subgrid-stress model based on the eddy-viscosity assumption with a fixed model constant. This required the use of an exponential damping function (Van Driest[84] function) near the wall. The first direct numerical simulation of turbulent channel flow was performed by Kim, Moin, and Moser,[34] for a centerline Reynolds number of 3300. Their code uses a spectral Fourier expansion in the homogeneous directions and Chebychev polynomials in the wall-normal direction. The governing equations are recast in a velocity-vorticity formulation which eliminates the pressure. The resolution for

this DNS was $192 \times 160 \times 129$ gridpoints in streamwise, spanwise and wall-normal direction, respectively. A variant of their code was used recently by Moser et al.[61] to perform DNS of turbulent channel flow up to a centerline Reynolds number of about 12 500 ($Re_\tau = 590$). With present-day computers, they were able to perform this case using a resolution of $384 \times 384 \times 257$ gridpoints. Moser et al. also examined the question of the logarithmic versus power-law velocity profiles in the inertial sublayer. Despite careful tests, the result was inconclusive (which may be attributable to the relatively low Reynolds numbers of this DNS study). They also collected statistics of the detailed balance for the turbulence kinetic energy. This balance can provide some insight in the mechanisms of the turbulence in wall-bounded shear flow (see Sec. 4.2.7). Here we mention only that another expected property of an inertial sublayer is that production and dissipation of turbulence kinetic energy are in balance. Moser et al. also investigated this property by plotting the ratio of production to dissipation. There were signs that with increasing Reynolds number a plateau at a ratio of unity was beginning to form, but again the evidence was not conclusive. Nevertheless, these simulations demonstrate that DNS can be a very useful complement to experiments in the study of turbulence because DNS can provide very extensive statistics of the flow, although only at relatively low Reynolds numbers. Moreover, such DNS datasets provide invaluable reference data for the testing of subgrid-stress models.

Finally, it must be mentioned that even though the theory of the logarithmic velocity profile for the inertial sublayer has been discussed extensively, it does not address at all the question of the detailed physical mechanisms which generate and support turbulence in wall-bounded shear flows. The structure of the near-wall turbulence seems to be composed of elongated "streaks" of high-speed and low-speed streamwise velocity. These streaks are surrounded by streamwise vortices, which were assumed to be equally elongated and to be occurring in counter-rotating pairs.[32] According to DNS results, however, (see review of Moin and Mahesh[60]) these streamwise vortices are of shorter extent than the velocity streaks and do not necessarily occur in pairs. Another question is the structure of the turbulence outside of the near-wall

region. Hairpin-like vortex structures with a preferred inclination of about 45° to the wall have been identified in this region. But these hairpin vortices have also been observed in homogeneous shear flow simulations, and may not be a special feature of wall-bounded turbulence.[60]

It is unclear whether LES can provide answers to questions about the detailed structure of wall-bounded turbulence. If LES velocity fields are used for this purpose (for example, through visualizations of velocity or vorticity fields), it must be kept in mind that these fields represent only the resolved-scale contributions. Therefore, LES will necessarily have difficulties to correctly reproduce structures which can have very small length scales near the wall. For example, the velocity streaks mentioned above have a mean spacing (in spanwise direction) of about $\Delta z^+ = 100$ (see the compilation of data in Ref. 32), i.e., one streak is about 50 viscous length scales wide. This is to be compared to the spanwise grid spacing for typical LES (see below, Table 4.1), which is about of the same size.

In the present work, which focuses on validating the new version of the stretched-vortex subgrid-stress model, we will limit ourselves mostly to the comparison of statistical quantities, which LES seems to be able to reproduce quite successfully, partly because the modeled SGS tensor can be used to estimate some of the contributions of unresolved subgrid-scale velocities to the turbulence statistics. Results like the turbulence-kinetic-energy budgets may also be useful in shedding light on the physical mechanisms of turbulence in wall-bounded shear flows.

4.2.1 Simulation geometry and parameters

The numerical method used for the simulations reported here was reviewed in Sec. 3.3. The simulations of the channel flow without rotation relied on the time-discretization scheme I (Sec. 3.3.3).

The non-dimensionalization for the channel flow simulations was described in Sec. 3.3.7; it is based on wall-shear velocity, u_τ, and channel halfwidth, h. For the presentation of the results, the wall-normal coordinate is also given in wall units:

$z^+ \equiv z u_\tau / \nu$.

The simulations were run until a statistically steady state was reached, as verified by symmetry in the obtained mean and rms velocity profiles, and by the time evolution of the wall shear stress. The simulations were then run further to collect statistics computed using plane- and time-averaging. For the $Re_\tau = 590$ simulation ($Re_c \approx 12\,500$), traces of the shear stresses $d\overline{\overline{U}}/dz$ at the walls, normalized by their average value ($Re_{\tau,\text{actual}} = 584$, see below), are shown in Fig. 4.5, for the time period during which statistics were collected.

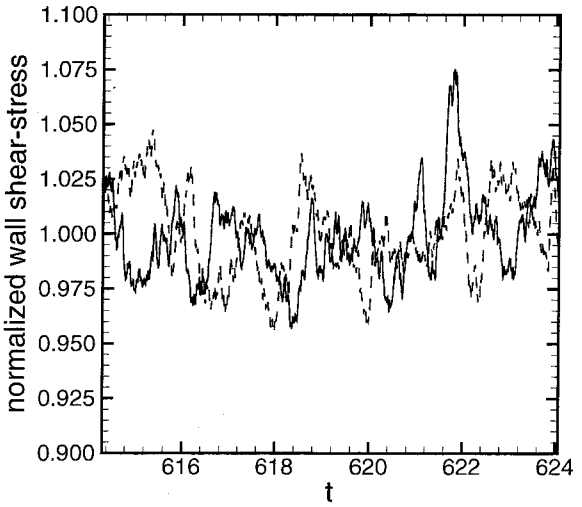

Figure 4.5: Normalized wall shear stresses for $Re_\tau = 590$ (case 9), —— : bottom wall, - - -: top wall.

Parameters for the different simulations are shown in Table 4.1. Simulations were performed for three different Reynolds numbers: $Re_\tau = 180$, $Re_\tau = 590$, and $Re_\tau = 1017$. If the Reynolds number is defined using the centerline velocity instead of the wall-shear velocity (Re_c), these values correspond to $Re_c \approx 3300$, $Re_c \approx 12\,500$, and $Re_c \approx 22\,800$. The column "LES" indicates whether the model has been turned on (Y) or off (N) in each case. (Runs without model, i.e., underresolved simulations, have been performed for comparison.) We also compare cases with and without the de-aliasing described in Sec. 3.3.1. The resolution is given in a way that accounts for de-aliasing. We call this the "effective" resolution. If no de-aliasing is used, the

numbers given in the table are simply the number of modes used in the simulation. When de-aliasing (using the "2/3"-method) is turned on, however, the number of modes used in the simulation is 50% higher than the numbers given here, with the upper 1/3 of the modes in the Fourier and polynomial spectra set to zero for de-aliasing. The number of modes retained after de-aliasing is given in the table as "effective" resolution.

The $Re_\tau = 180$ and $Re_\tau = 1017$ cases were performed using a constant mean pressure gradient to drive the flow. In this case, the (mean) shear stress at the wall will always go to the nominal value determined by Re_τ when the flow reaches steady state. For the present simulations (cases 1 to 8), the mean value was within one to two percent of the nominal value, with fluctuations typically less than ten percent of the mean. The negative influence of underresolution and the positive influence of the LES model can clearly be assessed in terms of the deviation of the centerline velocity from the correct value. For the $Re_\tau = 590$ case, the constant flowrate version of the code was used. (The flowrate was set to the value computed from the mean velocity profile of the DNS.[61]) This method of driving the flow is known to significantly reduce the time required to reach a steady state. With constant flowrate, the influence of the model is less pronounced in the mean profile (though still clearly visible) since the control simulation without SGS model (case 10) was forced to have the same flowrate as the LES (case 9). A good indication of the quality of the results in this case is the actual Re_τ as determined by the wall shear stress measured in the simulation results. The error in the wall shear stress for the LES (case 9) was only one percent, but without the model it was about seven percent.

Most of the channel flow simulations were performed with the $\tilde{\mathbf{e}}_3$ model version, except where otherwise noted in Table 4.1. For the $Re_\tau = 1017$ case, results for both the $\tilde{\mathbf{e}}_3$ and the $\tilde{\mathbf{e}}_2 + \tilde{\mathbf{e}}_3$ version (case 8) were available. It was found that the results of case 8 for the mean and rms quantities (not shown) are very close to the results obtained for alignment with $\tilde{\mathbf{e}}_3$ only. Case 8 was used to collect additional statistics for the turbulence-energy balances, which will be shown here. All channel flow large-eddy simulations presented here used the $J \to \infty$ version of the model,

which is less complicated and computationally less expensive than a version with finite J. The results of the decaying isotropic turbulence test indicate that the simpler $J \to \infty$ version performs sufficiently well for this application. This may not be true for all cases, especially when Reynolds-number effects become significant.

Table 4.1: Important parameters for the channel flow simulations.

Case	Re_τ	Domain		LES	De-	Effective Res.	Grid spacing			
		$\frac{L_x}{h}$	$\frac{L_y}{h}$		alias	$N'_x \times N'_y \times N'_z$	Δx^+	Δy^+	$\Delta z^+_{\min}$	$\Delta z^+_{\max}$
1	180	4π	2π	Y	Y	$32 \times 32 \times 43$	71	35	0.73	13.3
2	180	4π	2π	Y	N	$32 \times 32 \times 65$	71	35	0.32	8.76
3	180	4π	2π	N	Y	$32 \times 32 \times 43$	71	35	0.73	13.3
4	1017	$\frac{5}{2}\pi$	π	Y	Y	$48 \times 64 \times 65$	166	50	1.79	49.5
5	1017	$\frac{5}{2}\pi$	π	Y	N	$48 \times 64 \times 65$	166	50	1.79	49.5
6	1017	$\frac{5}{2}\pi$	π	N	N	$48 \times 64 \times 65$	166	50	1.79	49.5
7[a]	180	4π	2π	Y	Y	$32 \times 32 \times 43$	71	35	0.73	13.3
8[b]	1017	$\frac{5}{2}\pi$	π	Y	N	$48 \times 64 \times 65$	166	50	1.79	49.5
9[b,c]	590	2π	π	Y	N	$64 \times 64 \times 97$	58	29	0.46	19.2
10[b,c]	590	2π	π	N	N	$64 \times 64 \times 97$	58	29	0.46	19.2

[a] Case 7 is a realization of the same flow as case 1 at a different time.

[b] Uses the $\tilde{\mathbf{e}}_2 + \tilde{\mathbf{e}}_3$ model version

[c] Run with constant flowrate

4.2.2 Reynolds averaging and LES

When computing the rms velocity fluctuations, it is necessary to distinguish between two different decompositions which are used in this context: On one hand, a flow quantity U can be subjected to the LES decomposition in resolved-scale contribution $\tilde{U}$ and subgrid-scale component u. On the other hand, Reynolds averaging can be performed to decompose U in a mean quantity $\overline{\overline{U}}$ and the fluctuating component U'. The double overbar denotes an ensemble average (which will in practice be computed using spatial and temporal averages). Combining these two decompositions,

we can write,

$$U = \overline{\overline{\tilde{U}}} + \tilde{U}' + u', \tag{4.3}$$

and we assume $\overline{\overline{\tilde{U}}} = \overline{\overline{U}}$ and $u' = u$.

Now consider the correlation tensor of the turbulent velocity fluctuations $\overline{\overline{U_i'U_j'}} = \overline{\overline{U_iU_j}} - \overline{\overline{U_i}}\,\overline{\overline{U_j}}$. Using (4.3), we obtain

$$\overline{\overline{U_i'U_j'}} = \overline{\overline{\tilde{U}_i'\tilde{U}_j'}} + \overline{\overline{\tilde{U}_i'u_j'}} + \overline{\overline{\tilde{U}_j'u_i'}} + \overline{\overline{u_i'u_j'}}. \tag{4.4}$$

The first term is known, but the cross terms (correlation of resolved-scale, fluctuating velocities and subgrid-scale fluctuations) and the subgrid-scale correlation term are unknown in the context of LES. Only the last term is modeled. The best estimate for the rms quantities, which can be obtained from large-eddy simulations, is therefore,

$$\overline{\overline{U_i'U_j'}} \approx \overline{\overline{\tilde{U}_i'\tilde{U}_j'}} + \overline{\overline{\tau}}_{ij}. \tag{4.5}$$

We use this LES estimate for the rms velocity fluctuations (which requires knowledge of the full τ_{ij}, not only the trace-free component of the tensor) and compare it with the (unfiltered) results from DNS and experiment. Thereby we avoid applying a filter defined only in the context of large-eddy simulations to DNS and experimental results. For experimental data, it may often not be possible at all to compute filtered rms velocities because the data necessary to perform the filtering operation may not be available.

4.2.3 Mean and rms velocities for $Re_\tau = 180$

Results for the $Re_\tau = 180$ flow are shown in Fig. 4.6. Time averaging for these results was performed over a simulation time of $(t_{\text{end}} - t_{\text{start}})u_\tau/h = 30$. The mean velocity (Fig. 4.6a) of the de-aliased LES (case 1) shows good agreement with the DNS data by Kim, Moin, and Moser.[34] Comparison with case 3 (no model), shows

the significant contribution of the LES model. The results from the LES without de-aliasing (case 2) are little different from those with de-aliasing, although there is some improvement noticeable in the buffer region and near the center of the channel. The differences between case 1 (with de-aliasing) and case 2 (without de-aliasing) are slightly larger in the root-mean-square velocity fluctuations (Fig. 4.6b, shown for the near-wall region). In particular, streamwise fluctuations show some improvement when the de-aliasing is used. But both LES estimates, with and without de-aliasing, are somewhat too high for the spanwise fluctuations $v_{\rm rms}$. As described in Sec. 4.2.2, these are LES estimates for the total velocity fluctuations, which are compared to the unfiltered results of DNS in Fig. 4.6b.

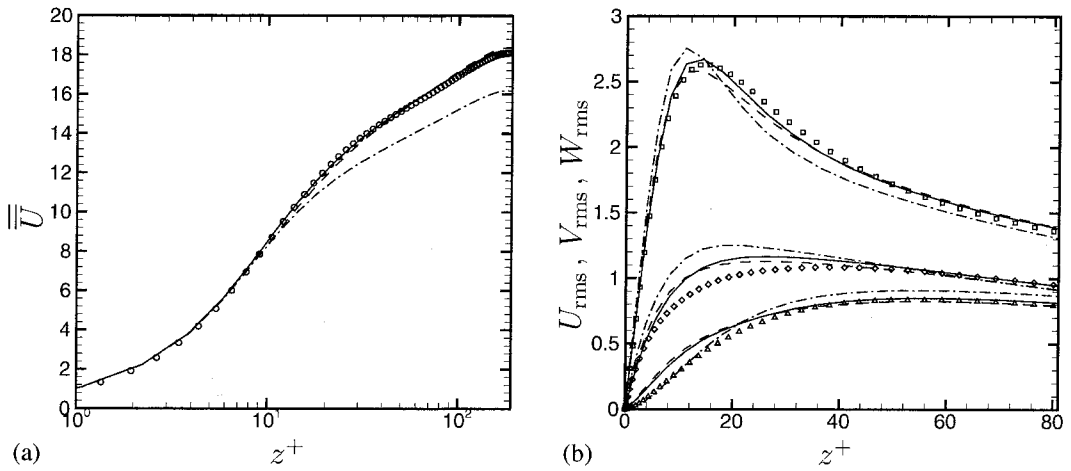

Figure 4.6: Channel flow at $Re_\tau = 180$, (a) Mean velocity and (b) root-mean-square velocity fluctuations (resolved plus subgrid). —— : LES, with de-aliasing (case 1); - - -: LES, no de-aliasing (case 2); - · -: no model, with de-aliasing (case 3); symbols: data (unfiltered) from DNS by Kim, Moin and Moser,[34] ○ : $\overline{\overline{U}}$; □ : $U_{\rm rms}$; ◇ : $V_{\rm rms}$; △ : $W_{\rm rms}$.

4.2.4 Mean and rms velocities for $Re_\tau = 590$

The mean and rms velocity profiles of the LES at $Re_\tau = 590$ (case 9) show similarly good agreement with the corresponding DNS results[61] as in the lower Reynolds number case. Comparison with case 10 (no model, same resolution) again shows the influence of the model. We note that for this Reynolds number, the flow was driven

using a constant flowrate, and for both cases 9 and 10, the same flowrate was prescribed. Therefore, the influence of the model on the mean profile is less pronounced, but still clear. The success of the model for this case can also be judged by looking at Re_τ achieved in the simulation: In the LES, it was $Re_{\tau,\text{actual}} \approx 584$, while without the model it was $Re_{\tau,\text{actual}} \approx 633$. Time averaging for case 9 was performed over $(t_{\text{end}} - t_{\text{start}})u_\tau/h = 9.75$, and for case 10 over $(t_{\text{end}} - t_{\text{start}})u_\tau/h = 8$. For $Re_\tau = 590$, no de-aliased runs were performed.

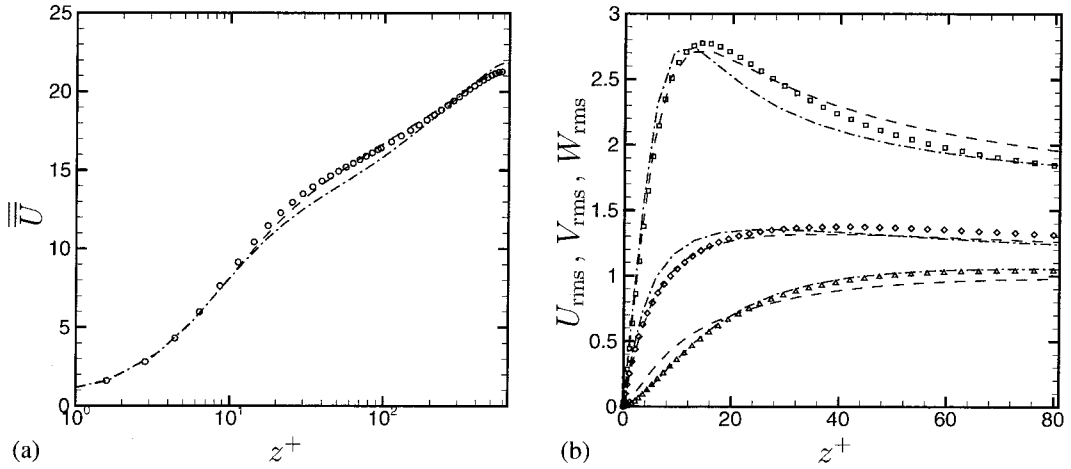

Figure 4.7: Channel flow at $Re_\tau = 590$, simulation with constant massflow, (a) Mean velocity and (b) root-mean-square velocity fluctuations (resolved plus subgrid). - - -: LES, no de-aliasing (case 9); - · -: no model, no de-aliasing (case 10); symbols: data (unfiltered) from DNS by Moser, Kim and Mansour,[61] ∘ : $\overline{\overline{U}}$ (only every second point, near centerline every fourth point shown); □ : U_{rms}; ◇ : V_{rms}; △ : W_{rms}.

4.2.5 Mean and rms velocities for $Re_\tau = 1017$

The mean and rms velocity profiles for $Re_\tau = 1017$ are shown in Fig. 4.8. The time averaging for these results was performed over $(t_{\text{end}} - t_{\text{start}})u_\tau/h = 10$. No DNS has been performed for a channel flow with comparably high Reynolds number. We compare our results with the experimental data by Wei and Willmarth.[1,86] Again the mean velocity profiles (Fig. 4.8a), both with and without de-aliasing, show good agreement with the reference data. The comparison with case 6 (no model, same grid resolution) shows the large influence of the model at this Reynolds number. The

agreement of the LES estimates for the total rms velocities with the experimental data is not as good as for the mean velocities. In particular, the de-aliased result for the streamwise fluctuations overestimates the peak value and the error is larger than for the case without de-aliasing. The de-aliased result seems to show some improvement in predicting the wall-normal coordinate of the peak. Note that there is no experimental data for the spanwise fluctuations in this case.

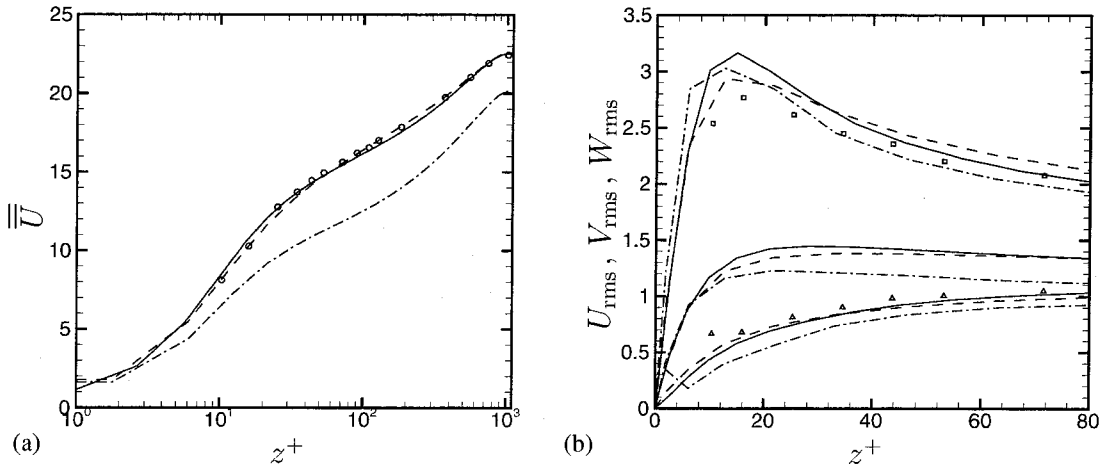

Figure 4.8: Channel flow at $Re_\tau = 1017$, (a) Mean velocity and (b) root-mean-square velocity fluctuations (resolved plus subgrid). —— : LES, with de-aliasing (case 4); - - -: LES, no de-aliasing (case 5); - · -: no model, no de-aliasing (case 6); symbols: data (unfiltered) from experiments by Wei and Willmarth,[86] ○ : $\overline{\overline{U}}$; □ : $U_{\rm rms}$; △ : $W_{\rm rms}$.

4.2.6 Model "dissipation"

The behavior of the model, in particular in the region very near to the walls, and its influence on the resolved scales can be illustrated by plotting the ratio $\varepsilon_{\rm sgs}/(\varepsilon_{\rm sgs}+\tilde{\epsilon}_{\rm visc})$ as a function of the wall-normal coordinate (Fig. 4.9). $\varepsilon_{\rm sgs}$ was defined in (2.26), it has the effect of a model "dissipation" on the resolved scales. The resolved-scale viscous dissipation is denoted by $\tilde{\epsilon}_{\rm visc} = 2\nu\tilde{S}_{ij}\tilde{S}_{ij}$. For the highest Reynolds number, the model contribution to the correct energy removal from the resolved scales is very significant, except for the region very close to the wall. For $z^+ \to 0$, i.e., when approaching the wall, the model contribution rapidly decays to zero, due to the dynamic estimate of the

factor $\mathcal{K}_0\epsilon^{2/3}$ using local circular-averaged structure functions. This vanishing model influence in the region very near to the wall, in connection with a reduced grid-spacing at least in the wall-normal direction, is typically required for large-eddy simulations of wall-bounded shear flows. This is probably one of the main limiting factors for large-eddy simulations of wall-bounded shear flows: The SGS models available today will not function correctly in the near-wall region, where shear stresses become very high, and length scales become very small, if the resolution is not increased near the wall so that the model contributes less and less to the dynamics of the flow as the wall is approached. But such high resolution requirements near the wall make LES of wall-bounded flows at very high Reynolds numbers prohibitively expensive. One possible solution could be the development of specialized models which are able to represent the physical mechanisms of the near-wall region.

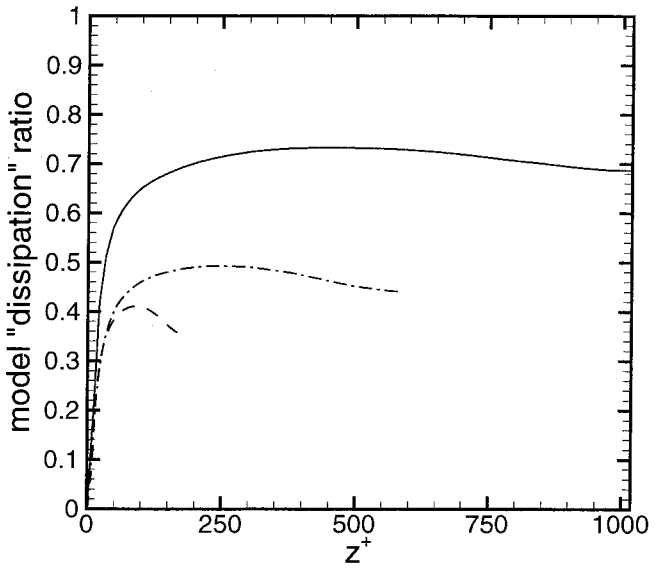

Figure 4.9: Model "dissipation" ratio $\varepsilon_{\text{sgs}}/(\tilde{\epsilon}_{\text{visc}}+\varepsilon_{\text{sgs}})$, —— : $Re_\tau = 1017$; - · -: $Re_\tau = 590$, - - -: $Re_\tau = 180$.

4.2.7 Turbulence-energy balance

The investigation of the turbulence kinetic energy balance, i.e., of the contributions of the individual terms in the evolution equation for the turbulence kinetic energy,

can provide information on questions like where turbulence energy is created and where it is dissipated, and how it is transported between regions. These questions are all relevant if one wants to understand the general mechanisms how, for wall-bounded shear flows in the present case, turbulence is generated and sustained, i.e., how energy input in the flow from external forcing (pressure gradient), which occurs at large scales, is converted to turbulence energy, i.e., energy contained in the fluctuating velocities at small scales, where energy is ultimately dissipated. In the present work, we will mainly investigate how well LES with the stretched-vortex model is able to estimate the contributions to the turbulence-energy balance by comparing LES results to DNS results.[61] Examples of the kind of information which can be obtained from such results will be discussed below.

In LES simulations, only the balance of the resolved-scale turbulence energy can be determined completely from the resolved quantities. For the channel flow, the following resolved-scale turbulence-energy equation is obtained, after averaging over homogeneous directions and time averaging:

$$\begin{aligned}\frac{d}{dt}\overline{\overline{\left(\frac{1}{2}\tilde{U}_j'\tilde{U}_j'\right)}} &= -\frac{\partial}{\partial x_3}\overline{\overline{\left[\tilde{U}_3'\left(\frac{\tilde{P}'}{\rho}+\frac{1}{2}\tilde{U}_j'\tilde{U}_j'\right)\right]}} - \overline{\overline{\tilde{U}_1'\tilde{U}_3'}}\frac{\partial\overline{\overline{U}}_1}{\partial x_3} - 2\nu\overline{\overline{\tilde{S}_{ij}'\tilde{S}_{ij}'}} \\ &\quad + \overline{\overline{\tilde{S}_{ij}'\tau_{ij}}} + 2\nu\frac{\partial}{\partial x_3}\overline{\overline{\left(\tilde{U}_i'\tilde{S}_{i3}'\right)}} - \frac{\partial}{\partial x_3}\overline{\overline{\left(\tilde{U}_i'\tau_{i3}\right)}}.\end{aligned} \tag{4.6}$$

For steady state, the left-hand side vanishes — note that d/dt denotes the material derivative, but the convective terms vanish for a steady channel flow — and the terms on the right-hand side must be in balance. The first term on the right-hand side is the convective diffusion of the total turbulence energy, which consists of the internal energy (pressure term) and the kinetic energy, the second is the production term, the third is viscous dissipation, the fourth term is subgrid "dissipation," i.e., the energy transfer rate from resolved scales to the subgrid scales, the fifth term is the surface work done by the viscous shear stresses of the turbulent motions, and the last term is the surface work done by the subgrid stresses. Those terms are shown for $Re_\tau = 180$ (case 7) in Fig. 4.10a (the two dissipation terms are lumped together, as are the two

surface work terms). In Fig. 4.10b, the ratio of the production term to the dissipation term (absolute values) is plotted. Unfiltered results from the DNS by Moser, Kim, and Mansour[61] are also shown in the figures. This allows the identification of those terms in the resolved-scale energy balance where significant contributions are missing compared to the energy balance for the full flowfield. Particularly large differences are visible in the production term and the convective-diffusion term of the kinetic energy.

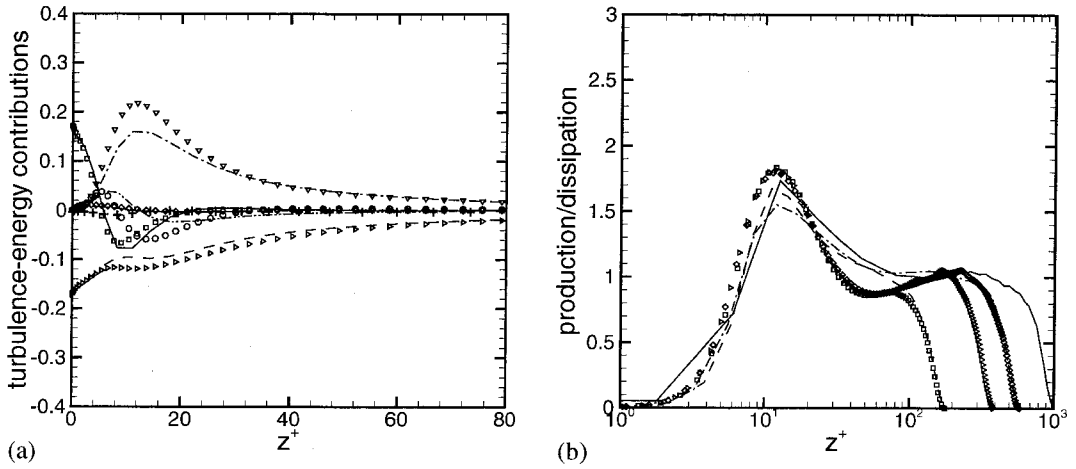

Figure 4.10: Turbulence-energy equation, (a) Terms of resolved-scale balance (see text) for $Re_\tau = 180$: - · -: production; - - -: dissipation; —— : surface work; - · · -: convective diffusion of turbulence kinetic energy; — —: convective diffusion of the internal energy (pressure term), +: sum of all terms. Also shown: DNS results (unfiltered) by Moser, Kim and Mansour,[61] $\bigtriangledown$: production; $\triangleright$: dissipation; $\square$: work of the tractions; $\circ$: diffusion of turbulence kinetic energy; $\diamond$: diffusion of internal energy. (b) Ratio of production to dissipation (absolute value), —— : $Re_\tau = 1017$; - · -: $Re_\tau = 590$, - - -: $Re_\tau = 180$, symbols: DNS,[61] $\square$: $Re_\tau = 180$; $\triangleright$: $Re_\tau = 395$; $\diamond$: $Re_\tau = 590$.

For those two terms, additional contributions from interactions with the subgrid scales can be estimated using the modeled SGS tensor:

$$\begin{aligned} \text{Production} &\approx -\overline{\overline{\tilde{U}_1'\tilde{U}_3'}}\frac{\partial\overline{\overline{U}}_1}{\partial x_3} - \overline{\overline{\tau}}_{13}\frac{\partial\overline{\overline{U}}_1}{\partial x_3} \quad \text{and} \\ \text{Convective diffusion of kinetic energy} &\approx -\frac{\partial}{\partial x_3}\overline{\overline{\left[\tilde{U}_3'\left(\frac{1}{2}\tilde{U}_j'\tilde{U}_j' + \frac{1}{2}\tau_{kk}\right)\right]}}. \end{aligned}$$

These are not exact expressions for the full production and kinetic-energy diffusion terms because their decomposition in resolved and subgrid component has additional contributions, but those cannot be estimated with a model for the SGS tensor. Including the known additional contributions, the terms of the turbulence-energy balance are plotted again in Fig. 4.11 for all three Reynolds numbers investigated here. The production term with the subgrid contribution in the $Re_\tau = 180$ case now matches the DNS result better. The significant disagreement remains, however, for the diffusion of turbulence kinetic energy. The LES estimate, even though it includes a subgrid contribution (the convective diffusion of the subgrid kinetic energy by the resolved-scale velocity), looks qualitatively similar to the result for the resolved scales only, which was obtained by Moin and Kim.[59]

To assess the quality of the numerical results, the sum of the terms which appear in the right-hand side of (4.6) was computed (i.e., without the additional subgrid contributions which are included in the Fig. 4.11). The value of the sum, which should go to zero for a sufficiently large number of statistical samples, is plotted with "+" symbols. In the low and medium Reynolds number cases, this condition is satisfied to acceptable accuracy, but in the high Reynolds number case (Fig. 4.11b), errors are visible very close to the wall. These errors have to be attributed to the relatively poor near-wall resolution at $Re_\tau = 1017$.

Some general observations for turbulence in wall-bounded shear flows can be made from these balances: The production and dissipation terms are clearly the dominant ones. But very close to the wall, the production becomes small because the increasing influence of viscosity dampens the turbulent fluctuations. To balance the viscous dis-

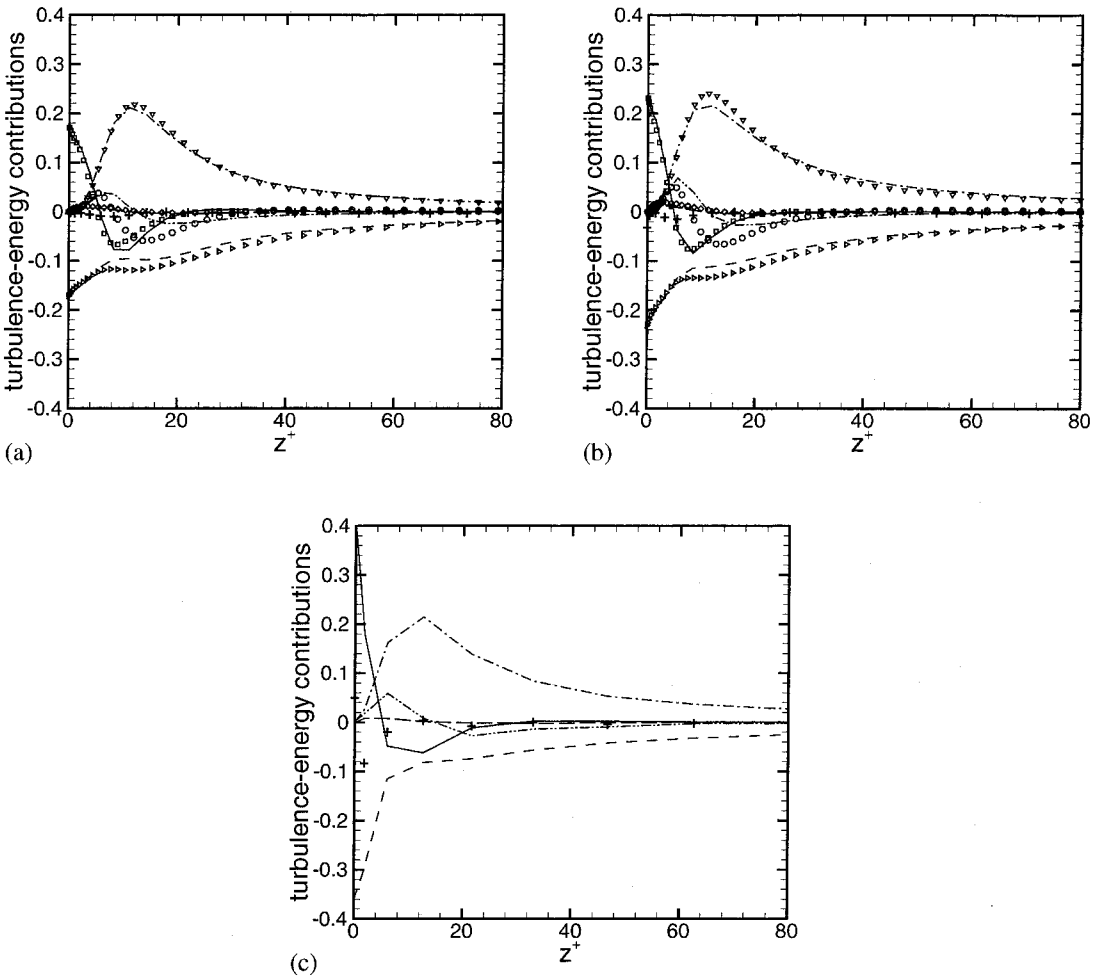

Figure 4.11: Turbulence-energy balance including known additional subgrid terms (see text), (a) $Re_\tau = 180$ (case 7), (b) $Re_\tau = 590$ (case 9), (c) $Re_\tau = 1017$ (case 8). - · -: production with subgrid contribution; - - -: dissipation; —— : surface work; - · · -: convective diffusion of turbulence kinetic energy with subgrid contribution; — —: convective diffusion of the internal energy (pressure term), +: sum of the resolved-scale terms, i.e., right-hand side of (4.6). Symbols (DNS) as in Fig. 4.10a: (a) $Re_\tau = 180$, (b) $Re_\tau = 590$.

sipation, energy must be carried towards the wall by the work of viscous shear stresses. The peak of the turbulent production occurs in the *buffer* layer,[82] which is the region between the viscous sublayer and the inertial sublayer (if it exists). In the region, where an inertial sublayer would be expected, all the other contributions become very small, and production and dissipation should be (approximately) balanced.

In Fig. 4.12, the ratio of production, including the subgrid contribution, to the absolute value of dissipation is shown. The LES estimate for $Re_\tau = 180$ ($Re_c \approx 3300$) and $Re_\tau = 1017$ ($Re_c \approx 22\,800$) is too high in the near-wall region compared to the DNS data. For the $Re_\tau = 590$ case ($Re_c \approx 12\,500$), this overestimate near the wall is reduced significantly. A somewhat finer grid (see the grid spacing in wall units in Table 4.1) was chosen for this Reynolds number. Improvements in these higher-order statistics can likely be attributed to this higher resolution. For the two higher Reynolds number cases, it is interesting to note that in the region where an inertial sublayer may be expected the ratio of production to dissipation is approximately unity, although the curve does not have an exactly horizontal plateau, and values are slightly above unity. The DNS data for intermediate Reynolds numbers seems to approach approximately the same value, however. But given the expected inaccuracies in this high Reynolds number LES, it cannot be conclusively determined if there is a region in turbulent channel flow where production and dissipation are balanced.

4.3 Rotating channel flow

The occurrence of rotating flows in engineering applications (e.g., turbomachinery) has motivated many studies of simplified flow configurations under rotation. One such configuration is the channel flow under spanwise rotation. Qualitative and quantitative results for this flow were obtained by Johnston et al.[27] for bulk Reynolds numbers of 5500 and 17 500 and moderate rotation rates. A more recent experimental investigation[62] was performed for low Reynolds numbers and very low rotation rates. Experimental investigations of rotating flow are not easy to perform because typically the whole channel assembly with instrumentation must be mounted on a

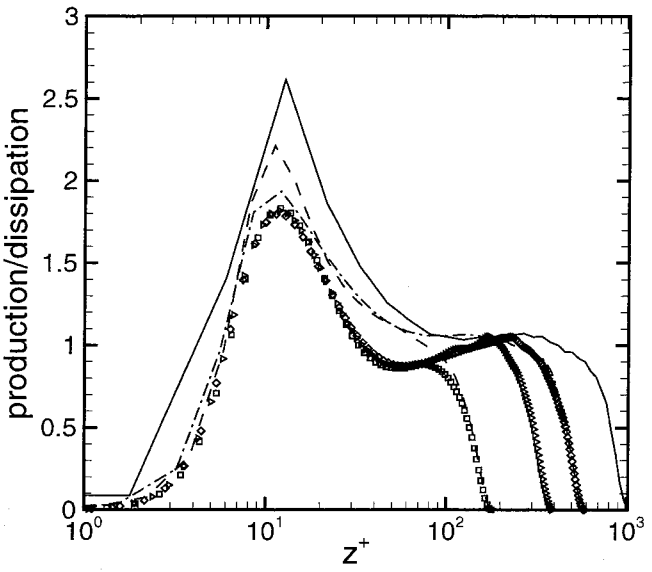

Figure 4.12: Ratio of production (including known additional subgrid contribution) to dissipation (absolute value), —— : $Re_\tau = 1017$ (case 8); - · -: $Re_\tau = 590$ (case 9), - - -: $Re_\tau = 180$ (case 7), symbols: DNS by Moser, Kim and Mansour,[61] □ : $Re_\tau = 180$; ▷ : $Re_\tau = 395$; ◇ : $Re_\tau = 590$.

rotating table.

In computational studies of flows under rotation, the flow is simulated in a reference frame rotating with the channel. A direct numerical simulation was carried out by Kristoffersen and Andersson[2,41] for a bulk Reynolds number of about 2900 (i.e., about the same as the non-rotating channel flow DNS by Kim et al.[34]) and low to moderate rotation rates, using a second-order finite-difference code with $128 \times 128 \times 128$ gridpoints. Their comparison of results for the non-rotating channel with the results of Kim et al. indicates that this resolution was sufficient, although the rms velocity fluctuations exhibited some small differences. Direct and large-eddy simulation (using a version of the dynamic eddy-viscosity model) of rotating channel flow was also carried out by Piomelly and Liu.[69] The interesting physical effects of rotation on the flow make it a useful testcase for large-eddy simulations. As will be discussed below, the effect of rotation is a suppression of the turbulent fluctuations on one side of the channel and an enhancement on the other. The SGS model has to react to both of these effects correctly for the simulation to produce good results.

4.3.1 Flow configuration and governing equations

The turbulent flow in an open channel under spanwise rotation is simulated in the reference frame of the channel, i.e., the coordinate system rotates with a constant angular velocity $\mathbf{\Omega} = (0, \Omega, 0)^{\mathrm{T}}$ about the spanwise or y-axis. The configuration is illustrated in Fig. 4.13. The Navier-Stokes equations (for incompressible flow) in a

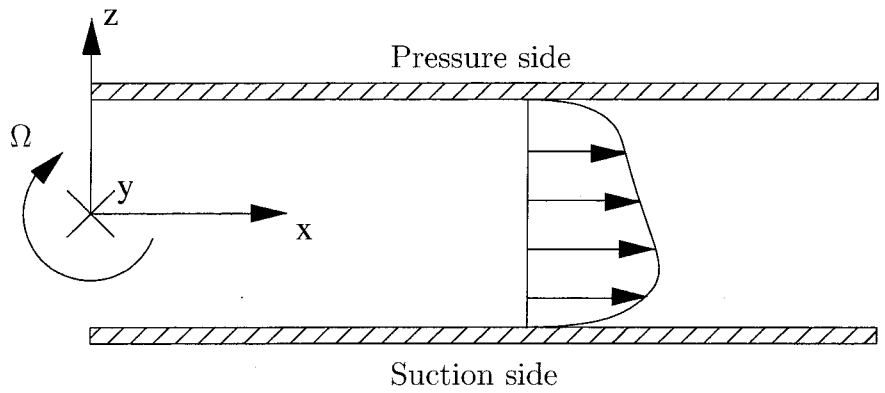

Figure 4.13: Channel flow under spanwise rotation: geometry and coordinate system.

reference frame rotating with constant angular velocity can be written in the non-dimensional form:

$$\frac{\partial U_i}{\partial x_i} = 0 \tag{4.7}$$

$$\frac{\partial U_i}{\partial t} + \frac{\partial}{\partial x_j}(U_i U_j) = -\frac{\partial P^*}{\partial x_i} + \frac{1}{Re_\tau}\frac{\partial^2 U_i}{\partial x_j \partial x_j} - Ro_\tau \epsilon_{ijk}\frac{\Omega_j}{|\mathbf{\Omega}|}U_k. \tag{4.8}$$

The alternating matrix ϵ_{ijk} is used to represent the cross product in the Coriolis-force term. The Reynolds number is defined as $Re_\tau = u_\tau h/\nu$, where h is again the channel halfwidth. Since the flow is not symmetric anymore for the rotating case, the definition of the velocity scale u_τ has to be generalized. We introduce local wall-shear velocities $u_{\tau s}^2 \equiv (\tau_W|_{z=-1})/\rho$ at the lower wall and $u_{\tau p}^2 \equiv -(\tau_W|_{z=1})/\rho$ at the upper wall. (These definitions are in terms of dimensional quantities.) Returning to the integrated, Reynolds-averaged momentum equation in streamwise direction (3.62), we can rewrite the boundary term using the definition of $u_{\tau s}$. After non-dimensionalization

(by formally introducing a velocity scale u_τ), we obtain:

$$0 = -(z+1)\frac{d\overline{\overline{P}}_0}{dx} - \overline{\overline{u'w'}} + \frac{1}{Re_\tau}\frac{d\overline{\overline{U}}}{dz} - \frac{u_{\tau s}^2}{u_\tau^2}. \tag{4.9}$$

At the upper wall, $z = 1$, this reduces to:

$$\frac{u_{\tau s}^2 + u_{\tau p}^2}{u_\tau^2} = -2\frac{d\overline{\overline{P}}_0}{dx}, \tag{4.10}$$

where we have used the definition of $u_{\tau p}$. This equation indicates that, for consistency with the non-rotating case, the generalized definition of the velocity scale, u_τ, must be:

$$u_\tau^2 \equiv \frac{1}{2}(u_{\tau s}^2 + u_{\tau p}^2). \tag{4.11}$$

In particular, for the case of a constant pressure gradient, this reduces (4.10) to $d\overline{\overline{P}}_0/dx = -1$.

The other non-dimensional number which characterizes this problem is the rotation number $Ro_\tau = 2\Omega h/u_\tau$, where $\Omega = |\boldsymbol{\Omega}|$. (The rotation number, which is commonly used in the literature on rotating channel flow,[41,48,69] is the inverse of the Rossby number.) The centrifugal force term $-\boldsymbol{\Omega} \times (\boldsymbol{\Omega} \times \boldsymbol{x})$ has a potential, and can be absorbed in the pressure term by defining $P^* = P - \frac{1}{8}Ro_\tau^2 r^2$ (with $r^2 = x^2 + z^2$).

4.3.2 Effects of spanwise rotation on turbulent shear flows

The effects of spanwise rotation on (approximately unidirectional) turbulent shear flows have been investigated extensively, see, e.g., Refs. 6, 27, 41. Johnston et al.[27] analyzed the influence of rotation with the help of the transport equation for the turbulence velocity correlation tensor (Reynolds stress tensor). According to this analysis, the non-dimensional parameter

$$S \equiv \frac{Ro_\tau}{(d\overline{\overline{U}}_1/dx_3)}, \tag{4.12}$$

which is related to the gradient Richardson number $Ri \equiv 2\Omega(d\overline{\overline{U}}_1/dx_3 - 2\Omega)/(d\overline{\overline{U}}_1/dx_3)^2$ by $Ri = S(S+1)$, determines the effect of rotation. The turbulence intensity may be expected to be reduced for $Ri > 0$, and increased for $Ri < 0$. A negative Richardson number corresponds to $-1 < S < 0$, but close to the wall in a shear flow, the gradient $(d\overline{\overline{U}}_1/dx_3)$ is very large, and therefore $Ri \approx S$. For the channel flow configuration investigated here, we have $S > 0$ at the lower wall (we will call this the *suction* side), and $S < 0$ at the upper wall (*pressure* side).

This approach using the turbulence-kinetic-energy budget based on Reynolds-averaging does not distinguish between velocity fluctuations caused by actual small-scale turbulence and those caused by large-scale secondary flow structures, which have been observed both in experiments[48] and computation.[41] Nevertheless the analysis based on the Richardson number describes the basic tendency towards stabilization or destabilization in accordance with observations. But as will be seen in the discussion of the observed values for the turbulence kinetic energy (see below), additional effects must be taken into account.

The presence of system rotation will also affect the turbulent energy cascade. The existence of an inertial subrange with a $k^{-5/3}$ energy spectrum presupposes that no external length scale or time scale influences the dynamics of the turbulence in this range. But clearly system rotation with a constant angular velocity Ω imposes a time scale $1/\Omega$. Therefore, the mechanism of energy transfer from large scales to small scales can be expected to change, which will also affect the form of the energy spectrum.

4.3.3 LES of rotating channel flow

In the computations reported here, we have used the stretched-vortex model as described in Table 2.1 to perform LES of (4.7) and (4.8). (The resolved-scale equations for this non-inertial frame correspond to (1.2) and (1.3), except that they include the Coriolis term for the resolved-scale velocity field.) Future research may lead to improved models for the vortex alignment or the functional form of the energy spectrum

in turbulence subject to rotating, but this is beyond the scope of the present work. We note, however, that the use of a $k^{-5/3}$-spectrum as given by (2.25) in the integrals for the subgrid kinetic energy and the structure-function relation may not be a very good model for turbulence subject to rotation, as discussed in the previous section. It has been suggested that dimensional analysis leads to a k^{-2}-spectrum for turbulence subject to strong rotation.[87] We have performed tests for the rotating channel using the stretched-vortex model with the energy spectrum of Ref. 87, but the results (not shown) obtained with the new spectrum were of poorer quality than those obtained with the $k^{-5/3}$ spectrum. Therefore, all the results presented here were computed using the model of Table 2.1 without any changes.

The parameters for the present LES were chosen to reproduce the DNS results of Kristoffersen and Andersson,[1,2,41] who simulated rotating channel flow at $Re_\tau = 194$ for several different rotation numbers. We performed LES for three of those cases: $Ro_\tau = 1.56$, $Ro_\tau = 3.046$ and $Ro_\tau = 7.625$. All cases were run using de-aliasing and with an effective resolution of $48 \times 64 \times 43$ in a domain of size $L_x \times L_y \times L_z = 4\pi h \times 2\pi h \times 2h$. Constant flowrate was enforced (matching the flowrate of the DNS in each case) to drive the flow. The mean velocity profiles are compared to the DNS results in Fig. 4.14. The agreement is quite good for all three cases, but seems to become better with increasing rotation number. At the lowest Ro_τ, the LES shows some difficulties matching the slope of the profile in the middle of the channel. For $Ro_\tau = 3.046$, a simulation at the same resolution, but without SGS model, has been performed. As described before, the differences in the mean profiles are not very pronounced in this case because the flowrate was forced to be the same in all cases, but the contribution of the model can still be distinguished. For constant flowrate simulations, it is important to compare the wall shear stress, which is a result of the simulations, to the values of the reference data (see Fig. 4.15). Here, it is visible, too, that the SGS model improves the results compared to the case with no model. The differences are not big, however, probably because at this relatively low Reynolds number the simulation without model is still marginally well resolved. The turbulence kinetic energy (TKE) $\overline{\overline{\left(\frac{1}{2}U_j'U_j'\right)}}$, i.e., the kinetic energy of the fluctuating

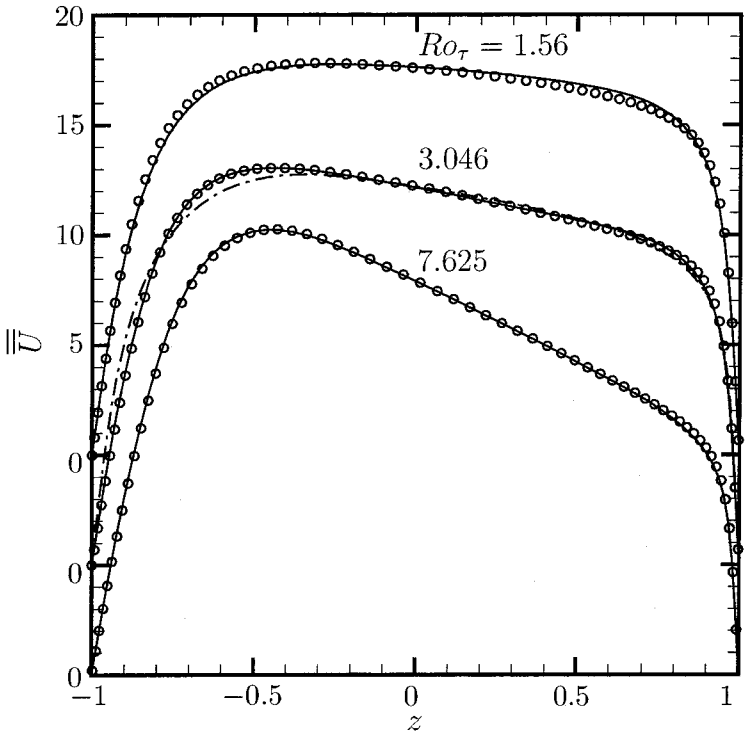

Figure 4.14: Channel flow under spanwise rotation for different rotation numbers, mean velocity profiles, —— : LES; - · -: no model (only for $Ro_\tau = 3.046$); symbols: data from DNS by Kristoffersen and Andersson.[41]

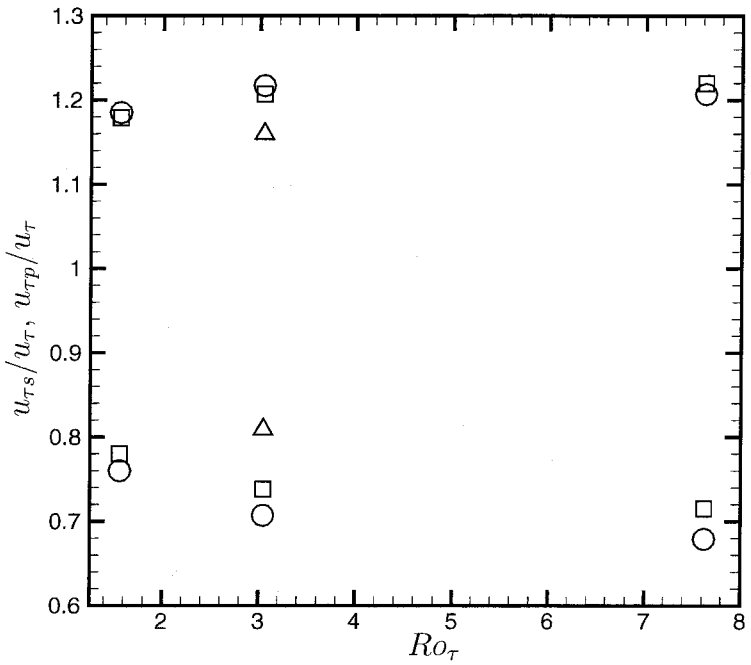

Figure 4.15: Local wall-shear velocities at suction and pressure sides for different rotation numbers, □ : LES; Δ : no model; ∘ : DNS.[41]

velocity field (possibly including secondary flows caused by roll cells), for the three rotation numbers has been estimated using (4.5), and compared to DNS results in Fig. 4.16. (The datafiles[1] available to us from the DNS of the rotating channel do not include rms values for the individual velocity components, which we had available for the non-rotating case.) Kristoffersen and Andersson observed that, as expected,

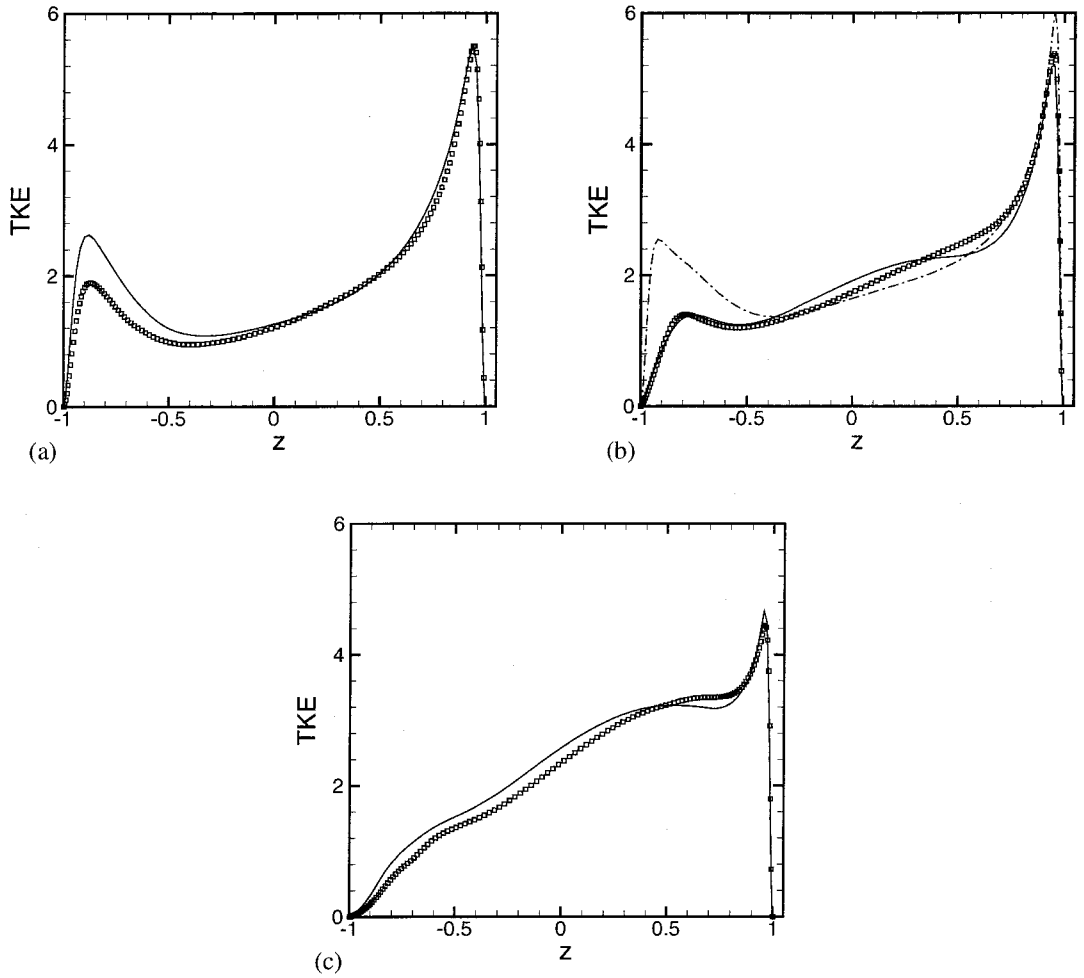

Figure 4.16: Turbulence kinetic energy (TKE) of channel flow under spanwise rotation, (a) $Ro_\tau = 1.56$, (b) $Ro_\tau = 3.046$, (c) $Ro_\tau = 7.625$. —— : LES, - · -: no model (only for $Ro_\tau = 3.046$); symbols: DNS.[41]

the turbulence intensity on the suction side is increasingly suppressed with increasing rotation number. In particular, one can see that for the highest rotation number investigated, the maximum of turbulence kinetic energy in the buffer layer has almost completely disappeared on the suction side. On the pressure side, an increase in the

peak of turbulence energy for increasing rotation number can be observed, but only in the regime of weak rotation. For higher rotation numbers, this trend levels off, and for the highest rotation number, $Ro_\tau = 7.625$, the turbulence kinetic energy on the pressure side falls below the values for intermediate rotation numbers. A possible explanation may be that the significant increase in the kinetic energy of the fluctuating field observed at lower rotation numbers on the pressure side is caused by the onset of roll-cell instability.[6] These roll-cell instabilities seem to be less pronounced at higher rotation numbers.

The LES results for the turbulence kinetic energy reproduce the basic trends observed in the DNS. Some larger discrepancies occur, however, on the suction side for the lowest rotation number. For the intermediate rotation number (Fig. 4.16b), the result without SGS model at the same resolution is also shown. In comparison with that, the LES result with the SGS model is significantly closer to the DNS result, especially at the suction side, although it still deviates somewhat from the correct result closer to the pressure side. But the positive influence of the model is more clearly visible in the turbulence energy than in the mean profile.

For the present work, we did not try to identify the possible presence of roll cells. Since we used the data of Kristoffersen and Andersson[1,2] for comparison, we collected the statistical data presented above in the same way as was done in this reference, by averaging over planes parallel to the wall and over time. This means that the velocity fluctuations may include contributions from the large roll cells as well as from the turbulence fluctuations.

It should be noted that, as a consequence of the development of longitudinal roll cells in rotating channel flow, the periodic boundary conditions used in DNS and LES of this flow may not be a good model anymore of laboratory flows with uniform inflow conditions.[41] It might be interesting for future work to investigate the presence of roll cells by trying to extract their patterns from the flowfield and separate out their influence in the statistics.

The influence of the SGS model would most likely be more pronounced at higher Reynolds numbers. But to our knowledge there is currently no reliable data (ex-

perimental or computational) available for rotating channel flow at higher Reynolds numbers and moderate rotation numbers, to which LES results could be compared.

4.3.4 Flow visualizations

The effects of rotation can also be illustrated by comparing flow visualizations of rotating and non-rotating channel flow. Isosurfaces of constant vorticity magnitude $|\boldsymbol{\omega}| = 45u_\tau/h$ for channel flow with and without rotation at approximately the same Reynolds number are shown in Fig. 4.17. (The value of the vorticity magnitude was chosen solely by visual criteria.) We note again that these visualizations only show the resolved-scale field, but they can nevertheless give a good qualitative impression of the effects of rotation on the channel flow. For the case with rotation ($Ro_\tau = 7.625$), the increased turbulence intensity at the pressure side (top wall) compared to the non-rotating case manifests itself clearly in the figure. The vorticity structures extend from the top wall far into the center region of the channel. The suppression of turbulence on the lower wall in the rotating case is also visible: The vorticity isosurface is much smoother than in the non-rotating case, which indicates the tendency to re-laminarization on the suction side.

As was mentioned above, a characteristic feature of near-wall turbulence is the presence of alternating streaks (i.e. thin, elongated structures) of high- and low-speed fluid in connection with elongated, streamwise vortices.[32] In Fig. 4.18, we have plotted contours of streamwise vorticity, again for cases without rotation (top), and with rotation (bottom). In the non-rotating case, the elongated, streaky structures appear to be visible at the chosen contour level in several spots interspersed between areas with no activity or less-organized vorticity patches with smaller length scales. In the rotating case, the entire top wall (pressure side) appears to be covered with streak-like structures, which also extend far into the interior of the channel. The bottom wall (suction side) shows almost no activity in the streamwise vorticity. The disappearance of the characteristic structures of a turbulent wall layer is consistent with the expected suppression of the turbulence on this side.

The strong spanwise variations in streamwise velocity caused by the streaks should also be observable in the wall-normal component, ω_z, of the vorticity vector. Isosurfaces of positive and negative ω_z are shown in Fig. 4.19. The streak structure is clearly visible at both walls in the non-rotating case. With rotation, the streaks are also present at the pressure side, but are again completely absent at the bottom wall (suction side). In Fig. 4.19, it can also be observed that the streak structures on the pressure side of the rotating channel have a smaller spanwise length scale than in the non-rotating case. It must be noted that the spanwise resolution in the rotating case was significantly higher than in the non-rotating case (64 versus 32 modes). It can therefore not be excluded with certainty that such finer structures would also be visible in the non-rotating case, if the resolution of the resolved field was high enough to capture them. But nevertheless the smaller streak spacing in the rotating channel is consistent with the expectation that the turbulence intensity is increased on the pressure side, and may explain why a higher spanwise resolution was required to obtain good results for the LES of the rotating case.

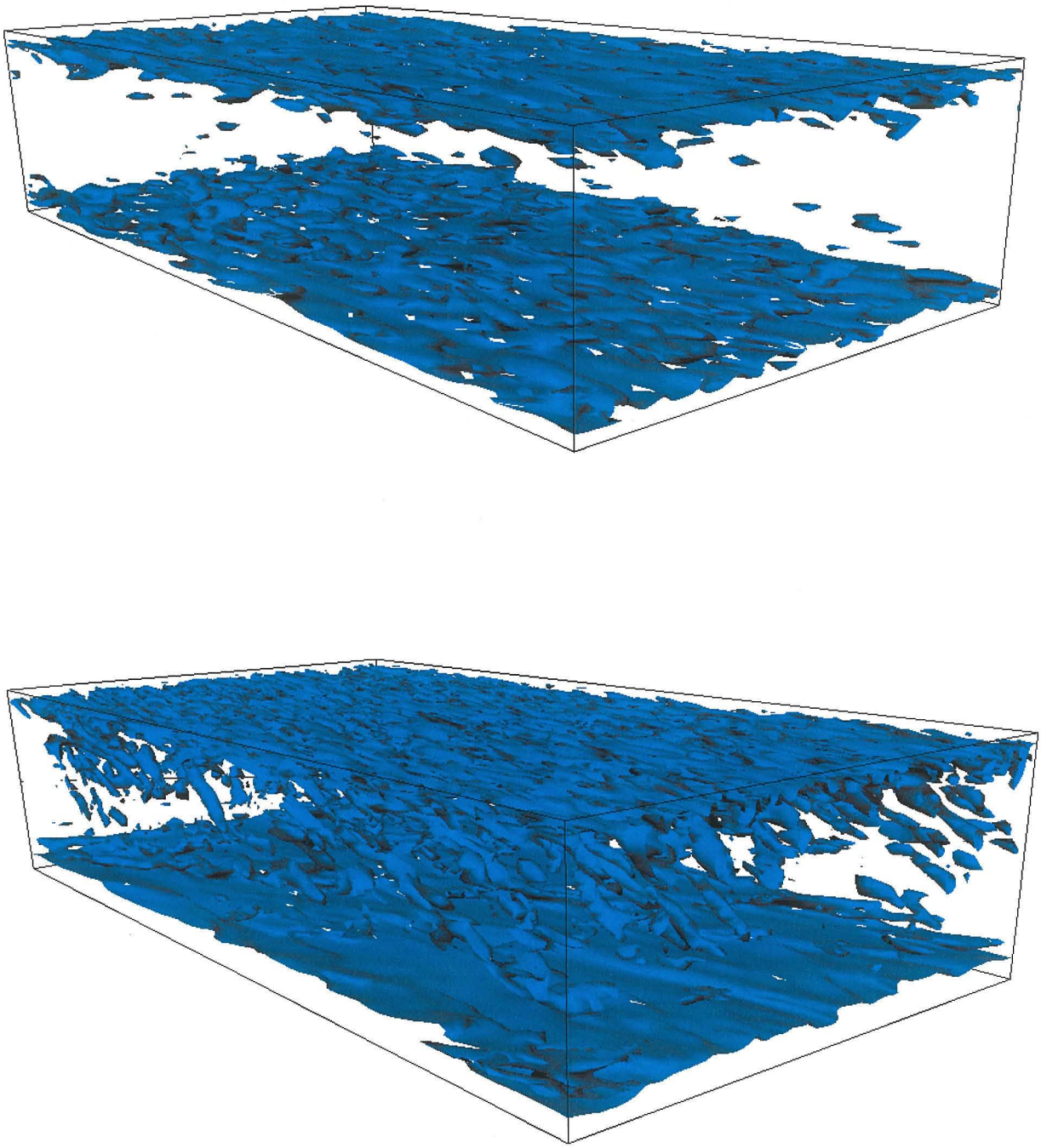

Figure 4.17: Isosurfaces of vorticity magnitude $|\boldsymbol{\omega}| = 45u_\tau/h$, top: $Re_\tau = 180$, $Ro_\tau = 0$ (case 1, see Table 4.1); bottom: $Re_\tau = 194$, $Ro_\tau = 7.625$. (Note that aspect ratio of channel has been modified for visualization purposes.)

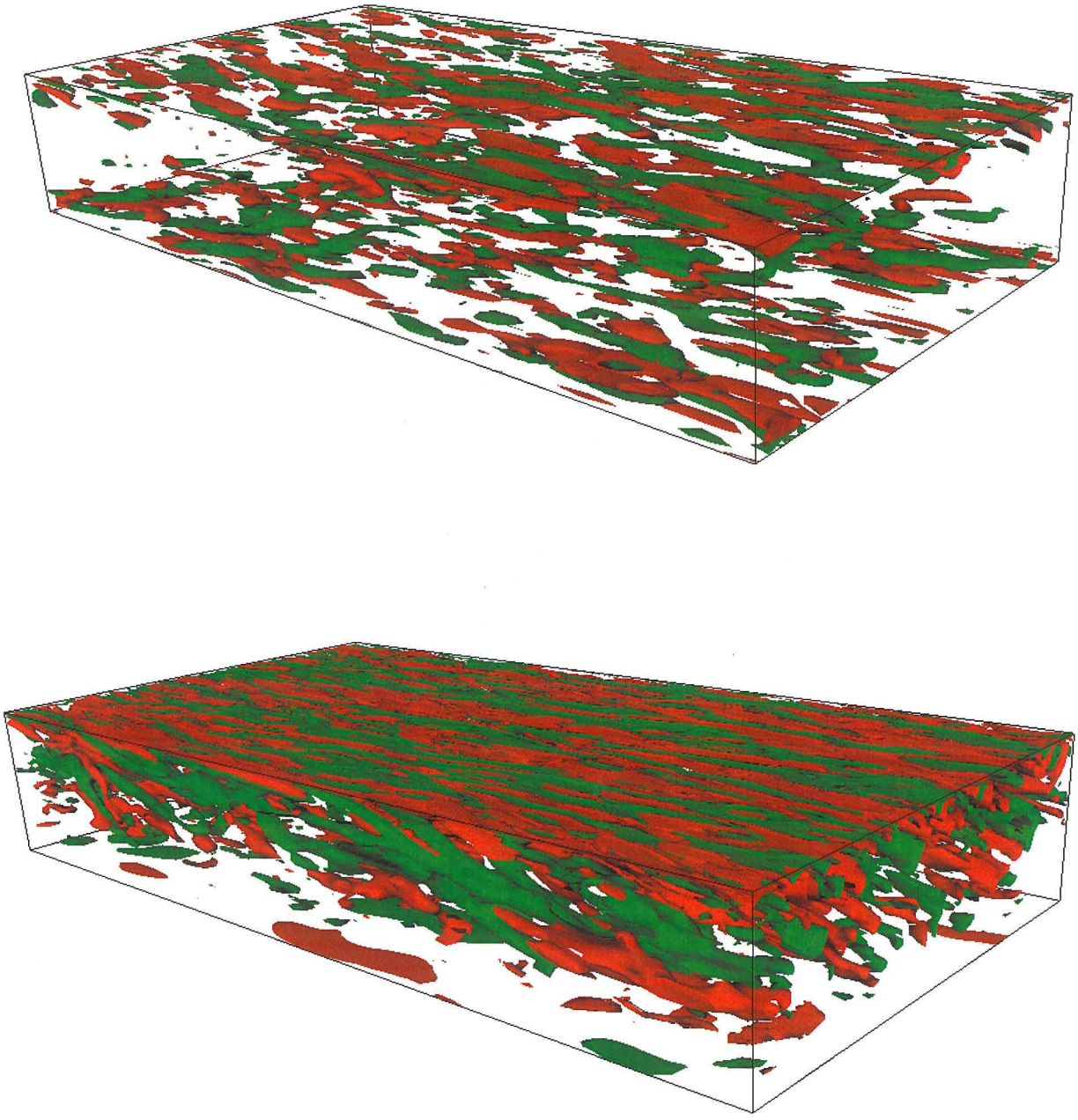

Figure 4.18: Isosurfaces of streamwise vorticity $\omega_x = 25u_\tau/h$ (green) and $\omega_x = -25u_\tau/h$ (red), top: $Re_\tau = 180$, $Ro_\tau = 0$; bottom: $Re_\tau = 194$, $Ro_\tau = 7.625$.

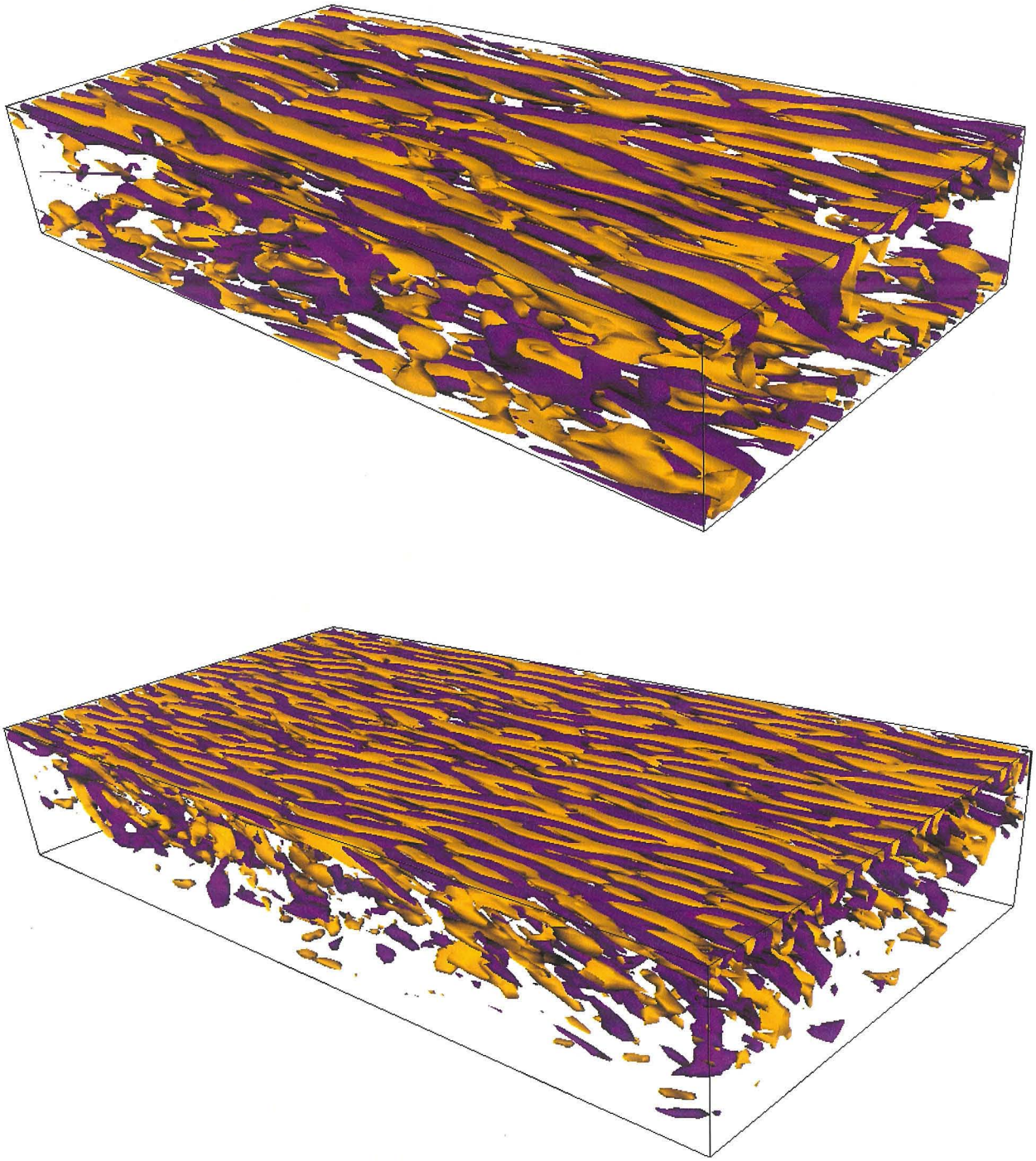

Figure 4.19: Isosurfaces of wall-normal vorticity $\omega_z = 15u_\tau/h$ (purple) and $\omega_z = -15u_\tau/h$ (yellow), top: $Re_\tau = 180$, $Ro_\tau = 0$; bottom: $Re_\tau = 194$, $Ro_\tau = 7.625$.

Chapter 5 Discussion

5.1 Numerical requirements for large-eddy simulations

In agreement with the conclusions of Kravchenko and Moin,[38] it has been found in the course of the present work that large-eddy simulation requires highly-accurate numerical methods. This is particularly true for the stretched-vortex model which relies on information from the resolved scales to estimate parameters for its model of the fine-scale turbulence. Large numerical errors in the resolved scales can therefore lead to unphysical model estimates, as can be seen from the influence of divergence errors, which has been discussed in Sec. 3.3.6. But as Kravchenko and Moin showed, LES with low-order numerical methods will always be problematic, independent of the choice of SGS model, because in that case the discretization errors of the numerical methods may be of the same order of magnitude as the subgrid term in the resolved-scale Navier-Stokes equations. Good candidates of highly-accurate numerical methods, which can also be applied to more complicated domains, appear to be the B-spline-based zonal-embedded-grid method by Kravchenko et al.,[40] or the spectral element method, see, e.g., Refs. 30 and 25. Currently, the use of these methods for LES in more complicated geometries appears to be inhibited by the large computational cost in the case of the B-spline method, and by the large divergence errors at domain boundaries in the interior of the domain for present implementations of the spectral element method.

An impression of the capabilities of the stretched-vortex model in combination with the numerical methods used for the present work can be gained by the following estimate: If one were to undertake a LES of channel flow using the same number of gridpoints ($384 \times 384 \times 257$) as Moser et al.[61] used for their DNS of channel flow at

$Re_\tau = 590$ ($Re_c \approx 12\,500$), a Reynolds number of $Re_\tau \approx 4000$ ($Re_c \approx 100\,000$) could be achieved in the LES. This estimate was based on the assumption that the size of the near-wall structures, which have to be resolved by the numerical method, scales with the wall variables. The grid spacings in wall units, which have been found to be adequate for successful LES in the present work, see table 4.1, can then be used to obtain the above estimate for the Reynolds number in wall units. In this case, we required the grid spacing in streamwise direction to be $\Delta x^+ = 100$ and in spanwise direction $\Delta y^+ = 30$. In wallnormal direction, we required that the first point away from the wall is located at $\Delta z^+ = 0.5$. This leads to the estimate of $Re_\tau = 4000$. The centerline Reynolds number is then obtained based on the logarithmic law of the wall using well-documented values for the constants.[82]

This example illustrates the main limiting factor for LES of wall-bounded flows: The structures very close to the wall, which have very small length scales, have to be adequately resolved by the numerical method since standard SGS models by design cannot correctly represent the region very close to the wall. Therefore, the grid spacing close to the wall has to be small enough to capture the important structures in this region, while the model contribution to the energy removal from the resolved scales goes to zero as the wall is approached. Simulations of wall-bounded turbulence at very high Reynolds numbers will require the development of special models for the wall layer.

5.2 Some properties of the fundamental equations of the stretched-vortex model in comparison with other SGS models

The model equation (2.24) for the SGS tensor, $\tau_{ij} = K(\delta_{ij} - e_i^v e_j^v)$, is the centerpiece of the stretched-vortex model, see Sec. 2.2. The tensor term $(\delta_{ij} - e_i^v e_j^v)$ is related to the orientation of the anisotropic vortex structure which is used to model the subgrid turbulence. The orientation of these structures in turn is coupled to the resolved-

scale flowfield. Furthermore, the SGS tensor is a function of the kinetic energy K contained in the subgrid-scales, which is modeled using the physical-space method described in Sec. 2.3. Clearly, the expression for τ_{ij} and its derivation is substantially different from the widely used eddy-viscosity ansatz for the SGS tensor, which is of the form: $\tau_{ij}^S - \delta_{ij}\frac{1}{3}\tau_{kk}^S = -2\nu_e\tilde{S}_{ij}$. This can already be seen by an examination of the simplest possible version of the stretched-vortex model using alignment only with the eigenvector $\tilde{\mathbf{e}}_3$ corresponding to the largest extensional eigenvalue of $\tilde{S}_{ij}$. For reasons of simplicity, this brief discussion will therefore be limited to the $\tilde{\mathbf{e}}_3$ version. One can see that, in this case, the SGS tensor obtained from the stretched-vortex model and the one obtained from an eddy-viscosity ansatz have one eigenvector in common because in the eddy viscosity ansatz, $\tilde{S}_{ij}$ and the SGS tensor have the same eigenvectors, and $\tilde{\mathbf{e}}_3$ is also an eigenvector for τ_{ij} in this version of the stretched-vortex model, as can easily be verified. But the corresponding eigenvalue is different for the two models, and in general the other two eigenvectors are also different.

The proportionality factor multiplying the tensor term in eddy-viscosity models is most frequently taken to be of the form proposed by Smagorinsky:[79] $\nu_e = (C_s l)^2(2\tilde{S}_{kl}\tilde{S}_{lk})^{1/2}$, where C_s is a model parameter and l is the characteristic length scale of the grid. In the stretched-vortex model on the other hand, the subgrid kinetic energy multiplies a tensor term, which can be interpreted physically as describing the partitioning of the subgrid kinetic energy between the components of the subgrid Reynolds stresses.

Moreover, the estimate for the subgrid kinetic energy, which is part of the stretched-vortex model, allows to compute the complete SGS tensor τ_{ij}, while the eddy-viscosity ansatz can only provide the trace-free component of the SGS tensor. This limits the ability of eddy-viscosity-based models to provide estimates for statistical quantities of the full turbulent flowfield, like root-mean-square velocities or the turbulence kinetic energy. But obtaining such estimates should be the goal for large-eddy simulations, in particular, if it is desired that LES results can be compared to laboratory measurements, which in general cannot be subjected to a filtering operation defined only in the context of a numerical procedure. Obtaining, for example, filtered rms velocities

from an experiment would require knowledge of the two-point velocity-correlation functions for separation lengths in the range of zero to two times the halfwidth of the filter.[1] Such a large dataset is typically not available from experiments like the channel flow measurements by Wei and Wilmarth.[86] We also note that, e.g., for the LES of decaying isotropic turbulence performed in the present work at a resolution of 32^3 modes, the subgrid scales still account for 20 to 30 percent of the total turbulence kinetic energy at an intermediate time ($U_\infty t/M_g = 98$) of the run, cf. Fig. 4.1. Thus a significant part of the full flowfield may be missing in large-eddy simulations which provide only results for the resolved scales.

The Smagorinsky model has more recently been combined with a method to dynamically estimate the model parameter C_s with information from the resolved scales. This dynamic procedure, which was proposed by Germano,[19] is based on properties of filtering. Using a testfilter with a filterwidth larger than the smallest resolved scales, it provides a formal mechanism for computing a parameter in a subgrid model. The physical-space version of the stretched-vortex model also estimates an important model quantity dynamically, in this case the factor $\mathcal{K}_0\epsilon^{2/3}$. But this method is based on a structure-function relation which is obtained as a kinematic result within the framework of the stretched-vortex model. Another difficulty with the testfiltering procedure is that the identity relating subgrid stresses and stresses at the testfilter level leads to an overdetermined system of five independent integral equations for the one unknown, the Smagorinsky factor C_s. While the problem can be solved in a mathematically consistent way by casting it into a variational formulation,[20] the computational complexity of the resulting dynamic localization models has in praxis led to the development of a variety of approximate solution methods, frequently involving the strong assumption that C_s as obtained from the dynamic procedure is constant in space.[20] Numerical instabilities arising from persistent negative values of C_s in actual LES have been addressed by *ad hoc* procedures like averaging in homogeneous directions,[19] or clipping.[39] Improved approximations have been proposed to address these shortcomings, for example a localization procedure[69] based on extrapolation in time (e.g., using an explicit Euler method), which, however, raises questions

about stability properties, if this version is to be applied to non-stationary flows like decaying isotropic turbulence. Another alternative uses averaging over flow pathlines by backwards time integration, resulting in the Lagrangian dynamic model,[53] which, however, requires the introduction of several additional model assumptions: An exponential weighting function is used in order to control the relative importance of events near the current simulation time to those at earlier times. Then a choice for the time scale in this weighting function has to be made. This introduces a new model parameter so that, despite the dynamic procedure, this version is not parameter-free. (Meneveau et al.[53] note, however, that they did not have to adjust their value for this parameter in the different testcases they performed.)

The eddy-viscosity ansatz is also used in the spectral eddy-viscosity model. A spectral expression[37] for ν_e can be obtained by using the Eddy-Damped Quasi-Normal Markovian (EDQNM) approximation (see Ref. 63 for a review of some of the developments). Large-eddy simulations based on this spectral eddy-viscosity model and variations thereof have been carried out, among others, by Lesieur and co-workers (for example, Refs. 43, 47, and 54). The basic form of the model equation for the subgrid-stress tensor in these models is the same as in other eddy-viscosity models. This is also true for the physical-space version[54] of the eddy-viscosity model, which is therefore very different from the present model, even though both use structure functions. Moreover, the physical-space version of the spectral eddy-viscosity model uses the structure-function relation for isotropic turbulence. As mentioned in Sec. 2.2.2, the assumption of isotropy is questionable in the context of LES, since it would imply vanishing Reynolds shear stresses and vanishing subgrid dissipation $-\tau_{ij}\tilde{S}_{ij}$. Furthermore, the expression for the spectral viscosity contains the Kolmogorov factor as parameter (not in the combination $\mathcal{K}_0\epsilon^{2/3}$ which appears in a Kolmogorov-type energy spectrum), and the fixed value for this parameter has to be specified as an input to the model, even in the structure-function version.

Other models which have been mentioned in the introduction are not discussed in this section since their approaches are clearly different from the stretched-vortex model.

5.3 On the comparison of model performance in actual LES

Evaluation of the merits of a particular modeling approach in comparison with other models would optimally consist in directly comparing the quality of the results of large-eddy simulations performed with the various models for the SGS tensor.

So-called *a priori* testing, i.e., the comparison of exact subgrid stresses obtained by filtering DNS data with the model predictions, which are computed using the filtered DNS velocity field as model input, has been found to give poor predictions of the success or failure of SGS models in actual LES. This, at least, is the case for traditional *a priori* testing methods, which try to compare model prediction and DNS data point-by-point. Newer approaches to *a priori* testing, which, for example, try to compare probability density functions of certain flow quantities, may be more promising. One fundamental problem remains, however, namely that a filtered DNS field is not the same as the resolved-scale field in actual LES, even at the same (filtered) resolution, because of the influence of the subgrid scales, which are not known exactly in actual LES.

The more desirable comparisons of results from actual large-eddy simulations would be very difficult to carry out, however, because ideally it would require performing simulations with different models for the same testcases with the same numerical method in order to exclude influences unrelated to the model performance, like the influence of different discretization methods or different grid resolutions. Such a comparison, however, would require a very large computational effort. Therefore, we will limit ourselves to some qualitative comparisons based on the information available in the literature.

Dynamic eddy-viscosity models have been applied in various large-eddy simulations. The large number of different model versions, however, makes a comparison difficult, since rarely one and the same model version has been applied to several different testcases. The first versions of the dynamic eddy-viscosity model using averaging in homogeneous directions have been applied to various LES of channel flow:

The results are typically in fair agreement with DNS and experiment, but both Germano et al.[19] and Meneveau et al.[53] show overpredictions of the centerline velocity. Piomelli[67] reports good agreement with reference data for his channel-flow LES using a plane-averaged dynamic eddy-viscosity, although it is difficult to verify in the published figures. We are not aware of decaying isotropic turbulence simulations performed with these simplest versions of the dynamic eddy-viscosity model. Piomelli and Liu[69] later proposed an improved dynamic eddy-viscosity model using an approximate localization as outlined in the previous section. They now chose rotating channel flow as testcase, for which they seem to achieve good agreement with DNS although again it is hard to verify in the published figures. Meneveau et al.[53] tested their proposal for an improved dynamic eddy-viscosity model, the Lagrangian dynamic model, both for decaying isotropic turbulence and channel flow. (In addition to the fully-developed channel flow, they also performed simulations for a transitional channel flow.) Their decaying-isotropic-turbulence simulation, following the Comte-Bellot and Corrsin experiment, gives quite good agreement for resolved-scale kinetic energy and energy spectra. Their simulation of fully-developed channel flow at a nominal Reynolds number of $Re_\tau = 650$ with the Lagrangian dynamic model shows improvements over simulations they performed with the plane-averaged dynamic model for the same case. But the mean profile is now somewhat too low in the buffer layer, and their is still an overprediction in the peak of the streamwise rms velocity. Overall, the Lagrangian dynamic model has been tested for different flows with good results, but the disadvantage remains that a weighting function has to be chosen, and a new model parameter is introduced, as described briefly in the previous section. Ghosal et al.[20] tested their dynamic localization models (DLM) for decaying isotropic turbulence with good results. One version of the dynamic localization model also includes an estimate for the subgrid kinetic energy, which is in good agreement with the reference data for the decaying-isotropic-turbulence test. But this model version has to solve an additional transport equation for the turbulence kinetic energy. No tests of the DLM for channel flow seem to have been performed, but Ghosal et al. performed an LES of backward-facing step flow, which is a very

challenging test. In this case, however, they used a simpler DLM version without an additional transport equation for the turbulence energy. This version of the DLM imposes the somewhat arbitrary constraint that the Smagorinsky constant does not depend on the coordinate in the homogeneous spanwise direction, which is similar to the averaging performed in earlier versions of dynamic eddy-viscosity models, except that the variational formulation of the DLM provides a more rigorous mathematical framework. Their comparison of the results for the LES of the backward-facing step flow with experimental data shows good agreement for the mean velocity. Turbulence velocity fluctuations are also shown in Ref. 20, but a comparison is difficult since their LES inevitably provides results only for the resolvable component of the fluctuations, while the experiment, of course, measured the fluctuations of the full flowfield.

Different versions of the spectral eddy-viscosity model have been applied in various LES (see Ref. 47 for a review). Few results, however, are available for quantitative comparisons in standard testcases. The structure-function version of the spectral eddy-viscosity model has been applied to forced isotropic turbulence,[54] but we are not aware of tests in decaying isotropic turbulence. Lesieur and Métais[47] report difficulties in the application of one version of the structure-function eddy-viscosity model to channel flow. Lamballais et al.[43] propose a new dynamic version of the spectral eddy-viscosity model, which operates in Fourier space. Using two-dimensional spectra of the resolved-scales, they obtain a dynamic estimate for the power-law exponent in the model energy spectrum, which is used to compute the spectral eddy viscosity. Their model, however, still contains the Kolmogorov factor as a parameter, and a localized version, which could operate in physical space only, has not been presented, yet. The spectral version of the model has only been tested for channel flow, with and without rotation. Results for the non-rotating case at $Re_\tau \approx 180$ and $Re_\tau \approx 395$ show overestimates of the centerline velocity. Comparison of fluctuating velocities is again made difficult because their LES only provide resolved-scale quantities, which are plotted together with unfiltered DNS results.

Among other, more recent developments in SGS modeling, we mention here only the subgrid-scale estimation model by Domaradzki and co-workers. Both the original

formulation in spectral space[15] and the physical-space version[13] have been tested in channel-flow LES at $Re_\tau = 180$ and $Re_\tau = 1017$. In particular, the physical-space version gives good agreement with reference data for the mean profiles. Turbulence velocities for the lower Reynolds-number case are compared with filtered DNS results. For the higher Reynolds number, Domaradzki and Loh[13] added the respective diagonal terms of the SGS tensor as computed by the estimation model to the resolved-scale fluctuations, so that a comparison with the experimental reference data for the turbulence fluctuations of the full flowfield is possible. These LES results are of similar quality as those in Fig. 4.8b. The spanwise resolution in the LES with the estimation model, however, effectively was twice as high as in the present work. The estimation procedure creates a subgrid-scale velocity field for wavenumbers up to two times the cutoff wavenumber. This range may be sufficient to represent the transport of energy across the cutoff, but does not actually constitute a model for the complete subgrid Reynolds stresses. Moreover, the estimation procedure requires a second, finer grid with twice the number of gridpoints, which increases the computational cost of the method. Forced isotropic turbulence calculation have been carried out with a different version of the estimation model,[16] but results for decaying isotropic turbulence simulations with the estimation model do not seem to be available.

In summary, it can certainly be said that the results obtained with the physical-space version of the stretched-vortex model are at least of equal, if not superior quality to those obtained with other models for the cases where comparisons are possible. Moreover, it appears that very few other SGS models have been successfully applied to a number of different testcases in exactly the same version, as was successfully done with the physical-space version of the stretched-vortex model.

Chapter 6 Conclusions and future work

The stretched-vortex model offers a promising alternative to other current subgrid-stress models for LES. It is distinguished from other models by its new approach, based on the physics of fine-scale turbulence, to the subgrid-modeling problem itself, even if the physical model necessarily is of extremely simple form. The information about the subgrid scales provided by this approach allows to obtain estimates for those statistical quantities of the full flowfield for which the second-order single-point product averages of the subgrid velocity field, i.e., the components of the SGS tensor, are the sole or dominant contributions from the fine-scale turbulence. An example is the subgrid kinetic energy, which is obtained as the trace of the SGS tensor in the stretched-vortex model, without solving an additional transport equation. Furthermore, the SGS model can be derived within the framework of the kinematics of the stretched-vortex structures without the need for *ad hoc* assumptions and without invoking isotropy of the subgrid scales. The important model parameter $\mathcal{K}_0\epsilon^{2/3}$ for the subgrid energy spectrum can be estimated with a dynamic procedure based on the stretched-vortex kinematics. A suitable vector quantity of the resolved field has to be chosen to determine the vortex alignment, and the form of the model energy spectrum has to be specified. But the results of decaying-isotropic-turbulence simulations are only weakly dependent on different choices. It was shown that all the testcases in the present work can be successfully simulated with the same version of the stretched-vortex model. With the use of a $k^{-5/3}$-spectrum for the whole subgrid range (extending to infinite wavenumbers) this version of the model does not contain any free model paramters.

The contribution of the present work consists in the development and testing of a physical-space version, which does not require global information of the resolved-scale field. Instead, it uses a structure-function relation derived from the kinematics of the stretched-vortex model. Estimating the resolved-scale structure functions in a circular

average ensures that this localized model is also applicable to wall-bounded flows. It has been tested for three different testcases, using both a Fourier spectral method and a compact finite-difference method to simulate decaying isotropic turbulence, and a hybrid polynomial/Fourier method to simulate channel flow with and without spanwise rotation. The results in all cases show good agreement with reference data from DNS and experiment, demonstrating that the model promises to perform well with different numerical methods and for different turbulent flows. The comparisons in the present tests were performed using the LES estimates for statistical quantities of the full turbulent flowfield, e.g., rms velocities and the kinetic-energy balance for the channel flow. To our knowledge, no other large-eddy simulation has attempted to provide estimates for the kinetic energy balance of the full flowfield. Our model results for these quantities were in good agreement with DNS data for most of the terms of the balance. The only exception was the term representing the convective diffusion of turbulence kinetic energy, which cannot be modeled using the SGS tensor because it contains third-order product averages (triple correlations) of velocity components.

Additional tests with the stretched-vortex model will have to be carried out to evaluate its performance for other important flow configurations, which could not be investigated within the scope of the present work, for example, flows with separation. Possible testcases are the backward-facing step, where the separation point is fixed, or flow over a cylinder or a sphere, which are even more challenging because the location of the separation point has to be predicted correctly by the simulation. The model has not yet been tested in flows with transition either, for example, in a boundary layer which undergoes transition from laminar to turbulent flow. The challenge for the model in this case is not to damp out the developing large-scale instabilities, which would therefore have to be sufficiently well resolved by the numerical method alone.

But given the good results obtained so far, and presupposing that it will also be applicable to other types of turbulent flows, the stretched-vortex model is expected to provide a good framework for LES of scalar transport, compressible flows, and ultimately flows with mixing and combustion, where information about the structure

of the subgrid turbulence is particularly important because of the dominant influence of the fine-scale motions on the molecular mixing process.

Appendix A Structure-function relation using a spherical average

We use the structure-function relation (2.38), but instead of averaging on a circle, we take the average over all possible directions of the separation vector $\mathbf{r}$ with fixed length r from a given location $\mathbf{x}$. As before, the coordinate system is chosen such that the three-axis is always aligned with $\mathbf{r}$, i.e., it will rotate with $\mathbf{r}$ over all possible directions as the average is taken. The angle θ in (2.38) is the polar angle of the vector $\mathbf{e}_v$ describing the orientation of the vortex structure, cf. (2.23). We note that (2.38) does not depend on the azimuthal angle; therefore, the spherical average, denoted by superscript ^{s}, reduces to

$$\tilde{F}_2^s(\mathbf{x}) = 2\int_{\theta=0}^{\pi}\int_{k=0}^{k_c} E(k)\left[1 - \mathrm{J}_0\left(rk\sin\theta\right)\right]\sin\theta\, dk\, d\theta. \tag{A.1}$$

Here, the integral over θ can be performed analytically, see, for example, Ref. 23, and we obtain

$$\tilde{F}_2^s(\mathbf{x}) = 2\int_0^{k_c} E(k)\left[2 - \pi \mathrm{J}_{-\frac{1}{2}}\left(\frac{kr}{2}\right)\mathrm{J}_{\frac{1}{2}}\left(\frac{kr}{2}\right)\right] dk.$$

Using the properties of Bessel functions,[23] that $\mathrm{J}_{\frac{1}{2}}(z) = \sqrt{2/(\pi z)}\sin z$ and $\mathrm{J}_{-\frac{1}{2}}(z) = \sqrt{2/(\pi z)}\cos z$, this can be transformed into:

$$\tilde{F}_2^s(\mathbf{x}) = 4\int_0^{k_c} E(k)\left[1 - \frac{\sin kr}{kr}\right] dk. \tag{A.2}$$

As required for consistency, taking a spherical average over the structure-function relation for the anisotropic stretched-vortex model recovers the functional form of the structure-function relation for isotropic turbulence, cf. Batchelor.[5]

Appendix B Analytical approximation for the integral in the structure-function equation

An analytical approximation for the integral in the denominator of (2.40) is derived so that the evaluation of this equation for $\mathcal{K}_0\epsilon^{2/3}$ can be simplified in actual simulations. The integral to be discussed is

$$Q(d,\sigma) \equiv \int_{\phi=0}^{2\pi}\int_{s=0}^{\pi} s^{-5/3}\left[1-\mathrm{J}_0\left(sd\sqrt{1-\sigma\cos^2\phi}\right)\right]\,ds\,d\phi, \tag{B.1}$$

which is a function of $d \equiv r/\Delta$ and $\sigma \equiv \sin^2\psi$. We first consider d small. Then the whole argument of the Bessel function is small, and we use the power series expansion of J_0 truncated to second order. Substituting this in the integral and performing the integration we obtain for small σ:

$$Q(d,\sigma) \approx \frac{3\pi^{7/3}}{16}(2-\sigma)d^2, \qquad \text{for} \qquad d \ll 1. \tag{B.2}$$

For large d, we substitute $v \equiv sd$. Then we have for Q:

$$Q = d^{2/3}\int_{\phi=0}^{2\pi}\int_{v=0}^{\pi d} v^{-5/3}\left[1-\mathrm{J}_0\left(v\sqrt{1-\sigma\cos^2\phi}\right)\right]\,dv\,d\phi. \tag{B.3}$$

But for large d we can, to a good approximation, set the upper limit of the v-integration to infinity. Introducing the change of variable $w \equiv v\sqrt{1-\sigma\cos^2\phi}$ we obtain

$$Q \approx d^{2/3}\int_{\phi=0}^{2\pi}(1-\sigma\cos^2\phi)^{1/3}\,d\phi\int_{w=0}^{\infty} w^{-5/3}\left[1-\mathrm{J}_0\left(w\right)\right]\,dw. \tag{B.4}$$

The integration over w can now be carried out analytically to give

$$C_1 \equiv \int_{w=0}^{\infty} w^{-5/3} \left[1 - \mathrm{J}_0(w)\right] dw = \frac{\pi}{2^{2/3}\sqrt{3}\,\Gamma^2\left(\frac{4}{3}\right)}. \tag{B.5}$$

The integrand in the ϕ-integral can be expanded in a power series for σ around $\sigma = 0$, and then the integral can be performed to obtain:

$$G(\sigma) \equiv \int_{\phi=0}^{2\pi} (1 - \sigma\cos^2\phi)^{1/3}\, d\phi \approx 2\pi - \frac{\pi}{3}\sigma - \frac{\pi}{12}\sigma^2 - \frac{25\pi}{648}\sigma^3 - \frac{175\pi}{7776}\sigma^4 + O(\sigma^5). \tag{B.6}$$

For large d we, therefore, have the approximation:

$$Q(d,\sigma) \approx C_1 G(\sigma) d^{2/3} \qquad \text{for} \qquad d \gg 1. \tag{B.7}$$

For the implementation, we use a composite formula which blends the two asymptotic results for small and large d. This approximate expression for the integral (B.1) in the structure-function relation is defined as follows:

$$Q_{\text{approx}}(d,\sigma) \equiv \frac{\frac{3\pi^{7/3}}{16}(2-\sigma)C_1 G(\sigma) d^2}{C_1 G(\sigma) + \frac{3\pi^{7/3}}{16}(2-\sigma)d^{4/3}}. \tag{B.8}$$

This expression is asymptotic to (B.2) for $d \ll 1$, and to (B.7) for $d \gg 1$. Comparisons of this approximate relation with results from the numerical integration of the exact expression (B.1) are shown in Table B.1 and Table B.2. The error can become quite large (up to 20%) for $d \to 1$. But in the important near-wall region one typically has $d \gg 1$ because of smaller grid spacing in the wall-normal direction in this region (i.e., $\Delta < r$, cf. Sec. 2.3.4). If the use of more precise values of the integral was desired, a two-dimensional table lookup of precomputed values from the numerical integration of Q could be used instead.

Table B.1: Comparison of the approximate relation Q_{approx}, given by (B.8), with numerical integration results Q_{ref} for the integral in the structure-function relation, $\sigma = \frac{1}{2}$.

d	Q_{ref}	Q_{approx}	$\lvert Q_{\text{ref}} - Q_{\text{approx}}\rvert / \lvert Q_{\text{ref}}\rvert$
1.0	3.37	2.71	0.196
2.0	8.62	7.19	0.165
5.0	19.38	19.26	0.006
10.0	33.34	34.54	0.036
20.0	55.49	57.78	0.041
50.0	105.92	109.17	0.031

Table B.2: Comparison of the approximate relation Q_{approx}, given by (B.8), with numerical integration results Q_{ref} for the integral in the structure-function relation, $\sigma = 1$.

d	Q_{ref}	Q_{approx}	$\lvert Q_{\text{ref}} - Q_{\text{approx}}\rvert / \lvert Q_{\text{ref}}\rvert$
1.0	2.27	1.94	0.146
2.0	6.01	5.42	0.097
5.0	14.45	15.46	0.071
10.0	25.45	28.47	0.119
20.0	42.93	48.25	0.124
50.0	82.76	91.75	0.109

Appendix C Approximate solution of the local-balance equation for the dissipation

The balance equation (2.44) may be written in the form

$$F(X) = 1 - (\Pi_1 - 3\,\Pi_4)X^4 - 3\Pi_4 \frac{X^{14/3}}{J^{2/3}} = 0, \qquad X < J, \tag{C.1}$$

where $\Pi_4 = \Pi_2\,\Pi_3$. Here we briefly discuss the properties of (C.1) when the parameters Π_1 and Π_4 are given. Note that $\Pi_1 \geq 0$ but Π_4 can be of either sign. Solutions of (C.1) are used only when $X < J$. Otherwise, the stress tensor is set to zero because $K = 0$. When $\Pi_4 \geq 0$, there is only one real positive solution for (C.1). This satisfies $X \geq J$ when $\Pi_1 \leq J^{-4}$ and $X < J$ when $\Pi_1 > J^{-4}$. When $\Pi_4 < 0$, there are either two real positive solutions for (C.1), which we denote by X_A and X_B respectively, or no real solutions. The solution of physical interest, X_A, is that on the branch which is a continuation of the solution $X_A = \Pi_1^{-1/4}$ for $\Pi_4 = 0$. The second real solution X_B is a bifurcation from infinity. There are no real solutions inside a region R defined by

$$0 < \Pi_1 < -3|\Pi_4| + \frac{7}{(2\,J^{2/3})^{6/7}}|\Pi_4|^{6/7}, \qquad \Pi_4 < 0. \tag{C.2}$$

In $\Pi_1 - \Pi_4$ space the boundary of R passes through the origin and the point $[\Pi_1, \Pi_4] = [0, -(7/3)^7/(2\,J^{2/3})^6]$, and has a turning point at $[\Pi_1, \Pi_4] = [J^{-4}, -2\,J^{-4}]$. When $[\Pi_1, \Pi_4]$ falls inside R the stress tensor is set to zero (conditional clipping). For $J = 1$ used presently for some decaying-turbulence runs, this requires $\Pi_1 < 1$, and a range of Π_4 satisfying (C.2). From (2.45) Π_1 is the order of the square of a cell Reynolds number. When $\Pi_1 < 1$ the SGS stresses are dominated by the resolved viscous stresses and clipping in a small fraction of cases has little effect on the overall calculation. Extensive experience with application of the model for 32^3 box turbulence shows that the incidence of clipping events maximizes at about 2% when $R_\lambda \approx 27$ (marginal

resolution) and are $O(10^{-5})$ at $R_\lambda = O(100)$.

When $J \to \infty$ with ν finite — used for all present channel calculations — (C.1) can be solved analytically. For $\Pi_1 - 3\Pi_4 > 0$, the first two terms of (C.1) are in balance, giving $X = (\Pi_1 - 3\Pi_4)^{-1/4}$. Then ϵ and $\mathcal{K}_0$ can be calculated because $\mathcal{K}_0\epsilon^{2/3}$ is known. The subgrid kinetic energy K follows from (2.41) and does not require X. When $\Pi_1 - 3\Pi_4 < 0$, the second and third terms are in balance, giving, for large J,

$$X \approx J\left(\frac{3\Pi_4 - \Pi_1}{3\Pi_4}\right)^{3/2}. \tag{C.3}$$

When $J \to \infty$ then $X \to \infty$ and the local resolved dissipation and the backscatter are in exact balance. A short calculation then shows that

$$K = \frac{2\nu\tilde{S}_{ij}\tilde{S}_{ij}}{\tilde{S}_{ij}(\delta_{ij} - e_i^v e_j^v)} \tag{C.4}$$

and τ_{ij} can be evaluated. The line $\Pi_1 - 3\Pi_4 = 0$ is a discontinuity in X but it is straightforward to show that τ_{ij} remains continuous.

When J is finite, the above expressions for X can be used as the zeroth order basis for either linear or quadratic expansions giving approximate analytical solutions to (C.1). These can be used directly or as initial approximations for numerical solution of (C.1) by Newton's method.

For example, we develop an approximate solution of the form $X = \frac{1}{(\Pi_1 - 3\Pi_4)^{1/4}}(1 + \delta X)$ with $\delta X \ll 1$ for $\Pi_4 < 0$. We set $J = 1$ and define the $Q_1 \equiv \Pi_1 - 3\Pi_4$ and $Q_2 = -3\Pi_4$. Then we can write the equation in the form: $1 - Q_1 X^4 + Q_2 X^{14/3} = 0$. Expanding for small δX and retaining terms up to second order, we obtain:

$$Q_2 Q_1^{-7/6} + \left(\frac{14Q_2}{3Q_1^{7/6}} - 4\right)\delta X + \left(\frac{77Q_2}{9Q_1^{7/6}} - 6\right)(\delta X)^2 + O(\delta X)^3 = 0 \tag{C.5}$$

Solving the quadratic equation for δX, we obtain the following approximate solution for X (again, only one of the two possible solutions is of physical interest, namely the

one which is a continuation of the solution for $\Pi_4 = 0$, see above):

$$X_{\text{approx}} = \frac{36Q_1^{7/6} - 56Q_2 + 3\sqrt{36Q_1^{7/3} - 30Q_1^{7/6}Q_2 - 28Q_2^2}}{Q_1^{1/4}(54Q_1^{7/6} - 77Q_2)} \qquad \text{for} \quad \Pi_4 < 0,\ J = 1 \tag{C.6}$$

Bibliography

[1] AGARD. *AR-345, A selection of test cases for the validation of large-eddy simulations of turbulent flows*, 1998.

[2] H. I. Andersson and R. Kristoffersen. Turbulence statistics of rotating channel flow. In F. Durst, N. Kasagi, and B. E. Launder, editors, *Turbulent Shear Flows 9.* Springer-Verlag, 1993.

[3] J. Bardina, J. H. Ferziger, and W. C. Reynolds. Improved subgrid scale models for large eddy simulation. AIAA 80-1357, 1980.

[4] G. I. Barenblatt and A. J. Chorin. Scaling laws and vanishing-viscosity limits for wall-bounded shear flows and for local structure in developed turbulence. *Commun. Pure Appl. Math.*, 50(4):381–398, 1997.

[5] G. K. Batchelor. *The Theory of Homogeneous Turbulence.* Cambridge University Press, Cambridge, UK, 1953.

[6] K. H. Bech and H. I. Andersson. Turbulent plane Couette flow subject to strong system rotation. *J. Fluid Mech.*, 347:289–314, 1997.

[7] M. E. Brachet, D. I. Meiron, S. A. Orszag, B. G. Nickel, R. H. Morf, and U. Frisch. Small-scale structure of the Taylor-Green vortex. *J. Fluid Mech.*, 130:411–452, 1983.

[8] C. Canuto, M. Y. Hussaini, A. Quarteroni, and T. A. Zang. *Spectral Methods in Fluid Dynamics.* Springer-Verlag, New York, 1988.

[9] D. C. Chan. *Effects of rotation on turbulent convection: Direct numerical simulation using parallel processors.* PhD thesis, University of Southern California, 1996.

[10] D. Coles. The law of the wake in the turbulent boundary layer. *J. Fluid Mech.*, 1:191–226, 1956.

[11] P. Comte, J. H. Silvestrini, and P. Begou. Streamwise vortices in large-eddy simulation of mixing layers. *European Journal of Mechanics B*, 17(4):615–637, 1998.

[12] G. Comte-Bellot and S. Corrsin. Simple Eulerian time correlation of full- and narrow-band velocity signals in grid-generated, 'isotropic' turbulence. *J. Fluid Mech.*, 48:273–337, 1971.

[13] J. A. Domaradzki and K.-C. Loh. The subgrid-scale estimation model. In D. Knight and L. Sakell, editors, *Recent Advances in DNS and LES*. Kluwer Academic Publishers, 1999.

[14] J. A. Domaradzki and K.-C. Loh. The subgrid-scale estimation model in the physical space representation. *Phys. Fluids*, 11(8):2330–2342, 1999.

[15] J. A. Domaradzki and E. M. Saiki. A subgrid-scale model based on the estimation of unresolved scales of turbulence. *Phys. Fluids*, 9(7):2148–2164, 1997.

[16] J. A. Domaradzki and P. P. Yee. The subgrid-scale estimation model for high Reynolds number turbulence. *Phys. Fluids*, 12(1):193–196, 2000.

[17] P. G. Drazin and W. H. Reid. *Hydrodynamic stability.* Cambridge University Press, 1981.

[18] F. Ducros, P. Comte, and M. Lesieur. Large-eddy simulation of transition to turbulence in a boundary layer developing spatially over a flat plate. *J. Fluid Mech.*, 326:1–36, 1996.

[19] M. Germano, U. Piomelli, P. Moin, and W. H. Cabot. A dynamic subgrid-scale eddy viscosity model. *Phys. Fluids A*, 3(7, 12(E)):1760–1765, 3128(E), 1991.

[20] S. Ghosal, T. S. Lund, P. Moin, and K. Akselvoll. A dynamic localization model for large-eddy simulation of turbulent flows. *J. Fluid Mech.*, 286:229–255, 1995.

[21] S. Ghosal and P. Moin. The basic equations for the large eddy simulation of turbulent flows in complex geometry. *J. Comput. Phys.*, 118:24–37, 1995.

[22] G. H. Golub and C. F. Van Loan. *Matrix computations.* The Johns Hopkins University Press, Baltimore, 1983.

[23] I. S. Gradshteyn and I.M. Ryzhik. *Table of Integrals, Series, and Products.* Academic Press, San Diego, 5th edition, 1994.

[24] W. Gropp, E. Lusk, and A. Skjellum. *Using MPI.* MIT Press, 1994.

[25] R. D. Henderson and G. E. Karniadakis. Unstructured spectral element methods for simulation of turbulent flows. *J. Comput. Phys.*, 122(2):191–217, 1995.

[26] J. Jiménez, A. A. Wray, P. G. Saffman, and R. S. Rogallo. The structure of intense vorticity in isotropic turbulence. *J. Fluid Mech.*, 255:65–90, 1993.

[27] J. P. Johnston, R. M. Halleen, and D. K. Lezius. Effects of spanwise rotation on the structure of two-dimensional fully developed turbulent channel flow. *J. Fluid Mech.*, 56:533–557, 1972.

[28] G. E. Karniadakis. Spectral element-Fourier methods for incompressible turbulent flows. *Comput. Methods Appl. Mech. Eng.*, 80:367–380, 1990.

[29] G. E. Karniadakis, M. Israeli, and S. A. Orszag. High-order splitting methods for the incompressible Navier-Stokes equations. *J. Comput. Phys.*, 97(2):414–443, 1991.

[30] G. E. Karniadakis and S. J. Sherwin. *Spectral/hp Element Methods for CFD.* Oxford University Press, 1999.

[31] S. Kida and Y. Murakami. Kolmogorov similarity in freely decaying turbulence. *Phys. Fluids*, 30(7):2030–2039, 1987.

[32] H. T. Kim, S. J. Kline, and W. C. Reynolds. The production of turbulence near a smooth wall in a turbulent boundary layer. *J. Fluid Mech.*, 50:133–160, 1971.

[33] J. Kim and P. Moin. Application of a fractional-step method to incompressible Navier-Stokes equations. *J. Comp. Phys.*, 59:308–323, 1985.

[34] J. Kim, P. Moin, and R. Moser. Turbulence statistics in fully developed channel flow at low Reynolds number. *J. Fluid Mech.*, 177:133–166, 1987.

[35] A. N. Kolmogorov. Local structure of turbulence in an incompressible viscous fluid at very high Reynolds numbers. *Dokl. Akad. Nauk SSSR*, 30:229, 1941.

[36] B. Kosović. Subgrid-scale modelling for the large-eddy simulation of high-Reynolds-number boundary layers. *J. Fluid Mech.*, 336:151–182, 1997.

[37] R. H. Kraichnan. Eddy viscosity in two and three dimensions. *J. Atmos. Sci.*, 33:1521–1536, 1976.

[38] A. G. Kravchenko and P. Moin. On the effect of numerical errors in large eddy simulations of turbulent flows. *J. Comput. Phys.*, 131:310–322, 1997.

[39] A. G. Kravchenko and P. Moin. B-spline methods and zonal grids for numerical simulations of turbulent flows. Technical Report TF-73, Stanford University, 1998.

[40] A. G. Kravchenko, P. Moin, and R. Moser. Zonal embedded grids for numerical simulations of wall-bounded turbulent flows. *J. Comput. Phys.*, 127:412–423, 1996.

[41] R. Kristoffersen and H. I. Andersson. Direct simulations of low-Reynolds-number turbulent flow in a rotating channel. *J. Fluid Mech.*, 256:163–197, 1993.

[42] A. Y. Kuo and S. Corrsin. Experiment on the geometry of the fine-structure regions in fully turbulent fluid. *J. Fluid Mech.*, 56:447–479, 1972.

[43] E. Lamballais, O. Métais, and M. Lesieur. Spectral-dynamic model for large-eddy simulations of turbulent rotating channel flow. *Theoret. Comput. Fluid Dynamics*, 12:149–177, 1998.

[44] S. K. Lele. Compact finite difference schemes with spectral-like resolution. *J. Comput. Phys.*, 103:16–42, 1992.

[45] A. Leonard. Energy cascade in large-eddy simulations of turbulent fluid flows. In F. N. Frankiel and R. E. Munn, editors, *Advances in Geophysics*, volume 18A, pages 237–249. Academic, 1974.

[46] A. Leonard. Large-eddy simulation of chaotic convection and beyond. AIAA 97-0204, 1997.

[47] M. Lesieur and O. Métais. New trends in large-eddy simulations of turbulence. *Annu. Rev. Fluid Mech.*, 28:45–82, 1996.

[48] D. K. Lezius and J. P. Johnston. Roll-cell instabilities in rotating laminar and turbulent channel flows. *J. Fluid Mech.*, 77:153–175, 1976.

[49] D. K. Lilly. A proposed modification of the Germano subgrid-scale closure method. *Phys. Fluids A*, 4(3):633–635, 1992.

[50] T. S. Lundgren. Strained spiral vortex model for turbulent fine structure. *Phys. Fluids*, 25(12):2193–2203, 1982.

[51] M. R. Malik, T. A. Zang, and M. Y. Hussaini. A spectral collocation method for the Navier-Stokes equations. *J. Comput. Phys.*, 61:64–88, 1985.

[52] C. Meneveau and J. Katz. Scale-invariance and turbulence models for large-eddy simulation. *Annu. Rev. Fluid Mech.*, 32:1–32, 2000.

[53] C. Meneveau, T. S. Lund, and W. H. Cabot. A Langrangian dynamic subgrid-scale model of turbulence. *J. Fluid Mech.*, 319:353–385, 1996.

[54] O. Métais and M. Lesieur. Spectral large-eddy simulation of isotropic and stably stratified turbulence. *J. Fluid Mech.*, 239:157–194, 1992.

[55] C. Millikan. A critical discussion of turbulent flows in channels and circular tubes. In *Proceedings of the Fifth International Congress on Applied Mechanics*, Cambridge, Mass., 1938.

[56] A. Misra. *Large-eddy simulation using a vortex-based subgrid stress model.* PhD thesis, California Institute of Technology, 1998.

[57] A. Misra and D. I. Pullin. A vortex-based subgrid stress model for large-eddy simulation. *Phys. Fluids*, 9(8):2443–2454, 1997.

[58] A. Misra, D. I. Pullin, and D. C. Chan. Large-eddy simulation using the stretched-vortex SGS model. In C. Liu and Z. Liu, editors, *Advances in DNS/LES, Proceedings of the First AFOSR International Conference on DNS/LES*, 1997.

[59] P. Moin and J. Kim. Numerical investigation of turbulent channel flow. *J. Fluid Mech.*, 118:341–377, 1982.

[60] P. Moin and K. Mahesh. Direct numerical simulation: A tool in turbulence research. *Annu. Rev. Fluid Mech.*, 30:539–578, 1998.

[61] R. D. Moser, J. Kim, and N. N. Mansour. Direct numerical simulation of turbulent channel flow up to $Re_\tau = 590$. *Phys. Fluids*, 11(4):943–945, 1999.

[62] K. Nakabayashi and O. Kitoh. Low Reynolds number fully developed two-dimensional turbulent channel flow with system rotation. *J. Fluid Mech.*, 315:1–29, 1996.

[63] S. A. Orszag. Analytical theories of turbulence. *J. Fluid Mech.*, 41:363–386, 1970.

[64] S. A. Orszag. Accurate solution of the Orr-Sommerfeld stability equation. *J. Fluid Mech.*, 50:689–703, 1971.

[65] S. A. Orszag and G. S. Patterson. Numerical simulation of three-dimensional homogeneous isotropic turbulence. *Phys. Rev. Lett.*, 28(2):76–79, 1972.

[66] A. E. Perry, S. Henbest, and M. S. Chong. A theoretical and experimental study of wall turbulence. *J. Fluid Mech.*, 165:163–199, 1986.

[67] U. Piomelli. High reynolds-number calculations using the dynamic subgrid-scale stress model. *Phys. Fluids A*, 5(6):1484–1490, 1993.

[68] U. Piomelli. Large-eddy simulation: Achievements and challenges. *Progress in Aerospace Sciences*, 35:335–362, 1999.

[69] U. Piomelli and J. Liu. Large-eddy simulation of rotating channel flows using a localized dynamic model. *Phys. Fluids*, 7(4):839–848, 1995.

[70] D. I. Pullin and P. G. Saffman. On the Lundgren-Townsend model of turbulent fine scales. *Phys. Fluids*, 5(1):126–145, 1993.

[71] D. I. Pullin and P. G. Saffman. Reynolds stresses and one-dimensional spectra for a vortex model of homogeneous anisotropic turbulence. *Phys. Fluids*, 6(5):1787–1796, 1994.

[72] D. I. Pullin and P. G. Saffman. Vortex dynamics in turbulence. *Annu. Rev. Fluid Mech.*, 30:31–51, 1998.

[73] R. S. Rogallo. Numerical experiments in homogeneous turbulence. NASA-TM-81315, 1981.

[74] R. S. Rogallo and P. Moin. Numerical simulation of turbulent flows. *Annu. Rev. Fluid Mech.*, 16:99–137, 1984.

[75] S. G. Saddoughi and S. V. Veeravalli. Local isotropy in turbulent boundary-layers at high Reynolds-number. *J. Fluid Mech.*, 268:333–372, 1994.

[76] P. G. Saffman and D. I. Pullin. Anisotropy of the Lundgren-Townsend model of fine-scale turbulence. *Phys. Fluids*, 6(2):802–807, 1994.

[77] R. Schiestel and S. Viazzo. A Hermitian-Fourier numerical method for solving the incompressible Navier-Stokes equations. *Computers & Fluids*, 24(6):739–752, 1995.

[78] M. K. Seager and A. Greenbaum. *DLAP - The sparse linear algebra package, double precision routines.* available via NETLIB, 1989.

[79] J. Smagorinsky. General circulation experiments with the primitive equations. *Mon. Weath. Rev.*, 91:99–164, 1963.

[80] J. L. Synge and C. C. Lin. On a statistical model of isotropic turbulence. *Trans. R. Soc. Canada*, 37:45–79, 1943.

[81] G. I. Taylor. Statistical theory of turbulence. *Proc. R. Soc. London, Ser. A*, 151:421, 1935.

[82] H. Tennekes and J. L. Lumley. *A First Course in Turbulence.* MIT Press, Cambridge, Mass., 1972.

[83] A. A. Townsend. On the fine-scale structure of turbulence. *Proc. R. Soc. London Ser. A*, 208:534–542, 1951.

[84] E. R. van Driest. On turbulent flow near a wall. *J. Aeronautical Sciences*, 23:1007–1036, 1956.

[85] A. Vincent and M. Meneguzzi. The dynamics of vorticity tubes in homogeneous turbulence. *J. Fluid Mech.*, 258:245–254, 1994.

[86] T. Wei and W. W. Willmarth. Reynolds-number effects on the structure of a turbulent channel flow. *J. Fluid Mech.*, 204:57–95, 1989.

[87] Y. Zhou. A phenomenological treatment of rotating turbulence. *Phys. Fluids*, 7(8):2092–2094, 1995.